Orally Available Near Infrared Imaging Agents for the Early Detection of Diseases

by
Sumit Bhatnagar

A dissertation submitted in partial fulfillment
of the requirements for the degree of
Doctor of Philosophy
(Chemical Engineering)
in the University of Michigan
2018

Doctoral Committee:

Assistant Professor Greg M. Thurber, Chair
Professor Jennifer J. Linderman
Professor Gary Luker
Professor Sunitha Nagrath

Sumit Bhatnagar

sumitbh@umich.edu

ORCID ID: 0000-0002-4410-8131

Dedication

This dissertation is dedicated to Nora, my parents, Swati, Vishal and Malika.

Acknowledgments

I would like to thank Prof. Greg Thurber for giving me the opportunity to join his lab and for all the hands-on training that he provided. He has been a constant source of guidance and support throughout my doctoral studies and has helped me become a critical thinker and problem solver. I would also like to thank my committee members, Prof. Linderman, Prof. Nagrath and Prof. Luker for their critique of my doctoral studies to make it the well-rounded dissertation it is now.

I appreciate all the help that the entire Thurber Lab – Liang Zhang, Cornelius Cilliers, Tejas Navaratna, Lydia Atangacho, Ian Nessler, Eshita Khera, Bruna Menezes, Reggie Evans, Emily Deschenes, Allison DuRoss, Aaron Priluck, Dyanne Neoh and Jianshan Liao – has provided over the years. I want to emphasize the role that Liang and Cornelius played in setting up the lab and protocols. I would also like to thank Eshita and Jianshan for their assistance in the rheumatoid arthritis work.

Prof. David Smith and Dr. Yongjun Hu provided me with a great deal of guidance from their pharmacy background and helped me learn techniques critical to the completion of this dissertation.

Prof. Ben Hackel gave me the opportunity to research with him for a year and half during my undergrad at the University of Minnesota. I believe that I am currently in the field of the study that I love because of that initial research experience and the influence that he had on me.

I would also like to express gratitude to all my friends – David, Andrea, Brett, Michelle, Mason, Deepika, Vikesh, Savannah, Trenton, Sarah, Cornelius, Nina, Nishanth, Cathy, Margaret, and Ian – for their continued support and for making my time in Ann Arbor truly memorable.

Lastly, I would like to thank my loving wife, Nora, who has been my side throughout my doctoral studies and has always pushed me to do the best I could. My parents, sister, brother-in-law and niece have always supported and loved me through any endeavor I embarked on and I am truly grateful for their presence in my life.

Table of Contents

List of Figures

List of Tables

Abstract

Early detection and treatment of diseases has the potential to dramatically improve patient outcomes. Diseases like cancer have shown remarkably higher survival rates when the cancer is detected early, before it has had a chance to metastasize and migrate to different regions. One way to increase rates of early detection is to implement annual screenings.

Current screening methods often focus on blood tests, which gather molecular information from the circulation, or imaging, which provides anatomical details. Molecular imaging has the ability to provide both types of information, but the high cost and radiation risk often preclude its use in population screening. In this thesis, we hypothesized that near-infrared fluorescent imaging agents could be administered orally and yield sufficient contrast for disease diagnosis. The use of NIR fluorescent targeting ligands provides both spatial and molecular information while making the entire process fast, inexpensive, completely non-invasive, and safe with the use of non-ionizing radiation.

For proof-of-concept studies to develop this novel technique, we selected integrin of the form $\alpha_v\beta_3$ as the target, and a high affinity peptidomimetic as the ligand. The major challenge of developing an orally available imaging agent is that orally available drugs and imaging agents generally have disparate properties. Orally available drugs are typically small in size and lipophilic in nature, while imaging agents tend to be larger in size and hydrophilic. In spite of these challenges, an IRDye800CW-labeled agent had an oral absorption of 2.3% and was selected for studies in the detection of two diseases: breast cancer and rheumatoid arthritis.

Mammography uses x-rays to detect suspicious lesions when screening for breast cancer but only provides anatomical data. This has lead to high false positive rates, unnecessary follow up tests and an estimated $4 billion in expenditure due to overdiagnosis. The method in this dissertation has the potential to increase sensitivity and specificity to improve early diagnoses and patient outcomes. The IRDye800CW agent was dosed at 5 mg/kg in an orthotopic tumor xenograft mouse model. Live animal imaging at 6, 24 and 48 hours post administration showed the highest target to background ratio of ~4 at 48 hours and histology showed high uptake of the agent by macrophages and breast cancer cells. Negligible uptake of a low affinity imaging agent control demonstrated specific uptake of the IRDye800CW agent in the tumor.

Rheumatoid arthritis (RA) is an autoimmune disease that leads to largely irreversible joint damage over time, but effective treatments are available. Therefore, there is intense interest in early detection of RA to prevent further damage, and some studies have even indicated that the disease could be cured (no long-term treatment required) if detected early. However, current methods lack the sensitivity to detect RA at an early stage. Oral delivery of the IRDye800CW agent in a collagen antibody induced arthritis mouse model showed significantly higher uptake in the inflamed joints compared to healthy joints. To scale the expected signal to clinically relevant depths, we developed a 3D COMSOL model for optical simulations of RA detection in the human hand. The simulations showed that for target to background concentration ratios of the imaging agent of 5.5 and 6.5, there was 95% and 98% probability of detection of the inflamed joint. The *in vivo* mouse model had an estimated target to background concentration ratio of ~20, which makes the detection of RA in humans very promising.

This dissertation demonstrates the oral delivery of molecular imaging agents for the detection of breast cancer and RA in relevant mouse models. These studies provide the

foundation to develop a range of oral molecular imaging agents for other biomarkers and diseases with the potential for earlier diagnosis and intervention to improve patient outcomes.

Chapter 1: Introduction

1.1 Background

It is widely accepted that the early detection of diseases can have a significant impact on patient outcomes. This is evident in diseases from infectious disease to cancer. Early intervention can prevent spreading of the disease or pathogen and stop irreversible damage. For example, in the case of a disease like breast cancer when it is diagnosed early and has not metastasized, the 5-year survival rates are over 90% whereas they drop to about 20% for cancers that have spread from the primary site[1]. For many diseases, a common screening method is to test the blood of the patient for biomarkers that would indicate the onset of a disease. This technique gives no spatial information about the origin of the biomarker/site of disease and requires high sensitivity to identify specific biomarkers out of all the molecules present in blood. The lack of spatial information and the need for early detection has led to a noteworthy push by the medical/ pharmaceutical community to develop techniques that can help diagnose diseases non-invasively while they are still in their early stages.

Historically, diseases were often diagnosed when the symptoms became apparent, which changed with the introduction of the imaging modalities for detection. With the discovery of X-ray in 1895, the field of medical imaging has steadily grown over time. X-rays, a form of ionizing electromagnetic radiation that can penetrate layers of opaque materials, allowed medical personnel to identify any injuries or abnormalities, particularly in bones. The use of heavy elements, such as iodine and barium as contrast agents improved the imaging of soft tissues. X-

ray tomography—replaced by computed tomography (CT) scans in the 1970s—was introduced in the 1940s and was used to obtain multiple image slices of the tissue by rotating the X-ray tube[2]. It was around this same time that the negative impacts of high amounts of radiation came to light, which has resulted in work to reduce radiation doses[3]. The 1950s saw the rise of nuclear medicine with the use of radioactive compounds instead of X-ray tubes and the advent of positron emission tomography (PET) scanning[2] and single photon emission computed tomography (SPECT) in the 1970s[4]. Ultrasound, first used in the 1970s, was one of the first imaging modalities that did not use any ionizing radiation and employed high frequency sound waves to generate images of the muscles, tendons, organs and fetuses inside the body. Magnetic resonance imaging (MRI) also emerged during this time period. It uses strong magnetic fields and radio waves to create anatomical images of the internal organs. The 1960s and 70s also saw the use of fluorescence to view hemorrhages and abnormalities in the eye[5] with recent uses of tissue autofluorescence in detection of diseases like oral neoplasia[6]. Fluorescence is the emission of non-ionizing electromagnetic radiation in the visible or near infrared range that is emitted by a molecule after excitation, usually with a form of radiation with a shorter wavelength.

These imaging modalities have improved over time with the technological boom of the last few decades. With an improvement in the technology itself, there has been a push for these imaging modalities to be able to provide more information with the use of imaging agents or contrast agents. Some well known imaging agents are gadolinium for MRI, ^{18}F-fluorodeoxyglucose for PET and iodine and barium for X-rays. These imaging agents help provide more information about internal organs and physiological processes in the body. Of the current FDA approved imaging agents, sixty-three were identified for Scintigraphy, 27 for X-ray, 13 for MRI, 8 for PET, 3 for Ultrasound and 3 for Optical (Fluorescent) imaging[7].

However, in order to get more detailed information about disease progression and monitoring therapeutic responses there needs to be improved specificity when using these imaging modalities[8]. Molecular imaging agents can provide this. Compared to contrast agents that are non-specific in nature and typically a reflection of the local physiology (e.g. blood flow, interstitial volume, etc.), molecular imaging agents interact specifically with a biomarker and are able to provide molecular information about the disease itself. With the medical community pursuing precision medicine, there is an increased need for molecular imaging agents to provide information in a non-invasive manner.

The aim of this thesis was to develop a screening method using a molecular imaging agent for the early detection of disease. In order to design a system that is inexpensive, safe, and easy to implement (for patient compliance), we had to select an imaging modality and route of administration of the imaging agent that would fit these criteria to make it feasible for screening large portions of the population.

1.2 Methods of Detection

The criteria considered for selecting an imaging modality were safety, cost, ability to provide molecular contrast, non-invasive nature of the method, and depth of imaging. Safety is paramount for a screening method since even a small risk percentage is amplified across thousands of (presumably healthy) people. For reference, there were about 40 million mammograms (MQSA national statistics) in the USA and a 0.01% risk would result in roughly 4000 people dealing with an adverse effect. Because of the large number of people likely to partake in screenings, cost is a major factor that needs to be considered. The imaging modality and imaging agents need to be relatively inexpensive when annual screenings are being considered. The 3rd criterion was molecular information. Anatomical data from medical imaging

can lead to several false positives, further testing and increased expenditure (see Chapter 4.3). A molecular imaging agent that can provide molecular information about the disease can help mitigate some of the false positives and extra expenditure as the imaging agent interacts with a biomarker specific to the disease. With the large populations being screened a non-invasive technique would be ideal to increase patient compliance (see Chapter 3.3). Finally, the imaging modality should have a sufficient depth of imaging to provide accurate information when imaging at clinically relevant depths.

Keeping the above-mentioned criteria in mind, all the imaging modalities were compared against each other with the summarized results in Table 1.1. CT is a form of X-ray imaging that images several sections (tomography) to represent the acquired data in a three-dimensional format. CT is a relatively fast imaging process, has a spatial resolution of about ~0.5 to 1 mm, is moderately expensive, has a high depth of imaging and is non-invasive[9]. Some of the limitations of this imaging modality are exposure to ionizing radiation, the use of contrast agents that can have renal toxicity, and negligible molecular contrast. MRI is a technique that uses magnetic fields and radio waves to form a detailed image of the entire body. MRI takes longer than a CT to complete a scan, has a spatial resolution of ~1mm, is expensive, has a high depth of imaging, is non-invasive and uses non-ionizing radiation. While MRI has excellent soft-tissue resolution, the sensitivity to exogenous imaging agents is low (albeit better than CT). PET is an imaging technique that uses radiolabeled imaging agents that decay and release positrons. PET detects the gamma ray pairs that are formed when the positron strikes an electron and uses this information to build tomographic images. SPECT on the other hand uses radiolabels that emit gamma rays that are captured by a gamma camera to create a 3D image of the distribution of the imaging agent. PET and SPECT have a spatial resolution of 5-7 mm and 8-10 mm, respectively[10]. PET is

an expensive imaging technique, whereas SPECT is comparatively moderately expensive[10]. Both imaging modalities have a high depth of imaging, high molecular contrast and high sensitivity. However, they are invasive as the molecular imaging agent is injected intravenously, and use ionizing radiation. Ultrasound employs high frequency sound waves to produce a two-dimensional anatomical image based on the how the waves travel through different tissues. Ultrasound has a spatial resolution of 0.1mm or 1-2 mm depending on the depth[10]. The technique is cheap, safe (lacks ionizing radiation), and some molecular imaging is possible with the use of microbubbles and vascular targeting. However, microbubbles require intravenous delivery. Therefore, this method generally lacks molecular contrast and has a limited depth of imaging in certain organs. Fluorescence imaging has a spatial resolution of 2-3 mm[10] for tomography and can have resolution of microns for surface imaging. It is relatively cheap, uses non-ionizing radiation, and has high sensitivity and molecular contrast. A major limitation of this technique is the low depth of imaging and the fact that it is invasive, as the fluorescent probes are typically injected intravenously.

Table 1.1 Comparison of FDA Approved Imaging Modalities

	CT	PET/ SPECT	X-Ray	MRI	Ultrasound	Fluorescence
Low Risk (Non-ionizing Radiation)				✔	✔	✔
Inexpensive			✔		✔	✔
Molecular Contrast		✔				✔
Non-Invasive			✔	✔	✔	
Depth of Imaging	✔	✔	✔	✔	✔	

With safety, cost, and the ability to provide molecular contrast being the most important for a screening method, fluorescence was chosen as the ideal method of detection for this thesis. The three optical (fluorescent) imaging agents that have been FDA approved are indocyanine green, fluorescein and aminolevulinic acid hydrochloride, and all are delivered intravenously with the aminolevulinic acid hydrochloride having the option of topical and oral delivery. Indocyanine green is being used to measure cardiac output[11], hepatic function, liver blood flow[12] and for ophthalmic angiographies. Fluorescein, discontinued by the manufacturer, was approved for angiography of the retina and iris vasculature[13]. Aminolevulinic acid hydrochloride is a prodrug that is metabolized to form a fluorescent metabolite and has recently been approved as an intraoperative imaging agent for the visualization of malignant gliomas[14].

1.3 Route of Administration

As mentioned above, the fluorescence imaging agents are typically delivered intravenously, but in order to make the process more feasible for large scale screening methods two other routes of administration, subcutaneous (SC) and oral delivery, were considered. SC delivery is the injection of a bolus dose of a drug or imaging agent in the subcutaneous layer between the dermis and muscle. The drug or imaging agent is then slowly absorbed over time into the blood stream. This route of delivery is considered minimally invasive. Oral delivery is the consumption of a pill, capsule, or solution, which dissolves in the stomach, is absorbed through the intestinal wall, passes through the liver and enters circulation. This method is completely non-invasive. Oral delivery is generally preferred to SC or intravenous delivery (See Chapter 3.3) due to the ease of delivery, low to no chance of an allergic reaction and cheaper costs of the drugs or imaging agents. SC is preferred over intravenous delivery because patients can administer it

themselves with minimal training, whereas intravenous delivery will always require a medical professional for administration.

1.4 Depth of Imaging

Another issue with fluorescence as the method of detection was the low depth of imaging. One way to rectify this is to use fluorescence with excitation and emission maxima closer to the infrared range. The wavelength range from 650 – 900 nm is usually referred to as near-infrared fluorescence (NIRF)[15]. NIRF increases the depth of imaging to about 1-2 cm from the surface of the skin. Aside from increasing the depth of penetration, another advantage of NIRF is that biological tissue has low absorption in this wavelength range[15], thereby reducing autofluorescence from tissue and increasing target to background ratios[16,17]. FDA approved Indocyanine green is a non-specific NIRF imaging agent and has been shown to work well in humans for its intended purposes. NIRF has also shown to be successfully used in angiograms of the eye[16], imaging the brain[16], intraoperative tumor imaging[18], hepatic output[12] and colon polyp identifications[19] among several others.

1.5 Objective

The objective of this thesis was to develop a non-invasive screening method for the detection of diseases with the ability to obtain spatial and molecular information simultaneously. Employing oral delivery in this technique makes the process completely non-invasive and the use of NIRF makes the process safe with the use of an imaging modality that does not rely on ionizing radiation. The only limitation of this technique would be that we are limited to the detection of diseases within several millimeters of tissue for epifluorescence imaging or several centimeters when employing NIR tomography (as in breast imaging). This thesis will be a proof-

of-concept study to show that detection of diseases post oral delivery is viable in mouse models with future studies looking into early detection.

1.6 Hypothesis

There is no literature evidence of orally available molecular imaging agents, largely due to the significant differences between high oral availability and specific targeting. High oral bioavailability generally requires low molecular weights and high lipophilicity based on Lipinski's rule of five[20]. Specific targeting on the other hand requires higher molecular weights for increased surface area to interact with the target and low lipophilicity to avoid off-site sticking. Despite these challenges we hypothesized that sufficient oral absorption and targeting could be achieved with appropriately balanced physicochemical properties of the imaging agents.

1.7 Work Plan

In order to accomplish the objective, the work plan shown in figure 1.1 was devised to make sure that we could develop the imaging agent and apply it to show the feasibility of detection of diseases in mouse models.

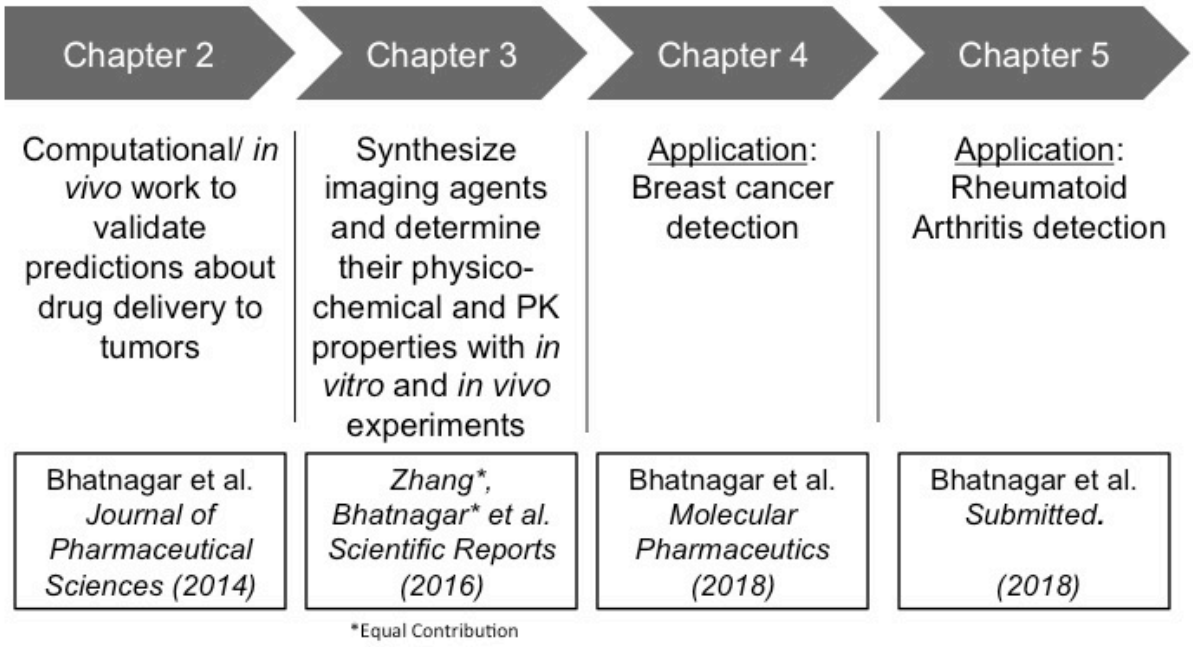

Figure 1.1 Work plan for the dissertation

Chapter 2 will show the *in vivo* validation of a theoretical computational model that can predict drug delivery in tumors. The model was validated in tumor xenografts in mice for wide range of drugs from small molecules to antibodies. The model was used to simulate the pharmacokinetic properties of potential imaging agents.

Chapter 3 highlights the synthesis of the potential imaging agents and *in vitro* studies used to determine the pharmacokinetic properties of these agents. The studies were used to select the imaging agents that would be used in the mouse models.

Chapter 4 uses the selected imaging agent for the detection of breast cancer in an orthotopic tumor xenografts mouse model.

Chapter 5 applies the same selected imaging agents in the detection of rheumatoid arthritis in a Collagen Antibody Induced Arthritis (CAIA) model and uses a 3D COMSOL model to show that epifluorescence imaging is feasible at clinically relevant depths.

Chapter 2: Multichannel Imaging to Quantify Four Classes of Pharmacokinetic Distribution in Tumors

2.1 Publication Information

Bhatnagar S, Deschenes E, Liao J, Cilliers C, Thurber GM 2014. Multichannel Imaging to Quantify Four Classes of Pharmacokinetic Distribution in Tumors. Journal of pharmaceutical sciences 103(10):3276-3286.

Modifications have been made to the published document to adapt the content to this dissertation.

2.2 Abstract

Low and heterogeneous delivery of drugs and imaging agents to tumors leads to decreased efficacy and poor imaging results. Systemic delivery involves a complex interplay of drug properties and physiological factors, and heterogeneity in the tumor microenvironment makes predicting and overcoming these limitations exceptionally difficult. Theoretical models have indicated there are four different classes of pharmacokinetic behavior in tissue depending on the fundamental steps in distribution. In order to study these limiting behaviors, we used multichannel fluorescence microscopy and stitching of high-resolution images to examine the distribution of four agents in the same tumor microenvironment. A generic partial differential equation model with a graphical user interface was used to select fluorescent agents exhibiting

four classes of behavior, and the imaging results compared favorably with predictions. A small molecule exhibited higher concentrations in regions with high blood flow, an antibody gave perivascular distribution limited by permeability, high plasma protein and target binding resulted in diffusion limited distribution for a lipophilic small molecule, and an imaging agent was limited by the number of binding sites in the tissue. Together, the probes and simulations can be used to investigate distribution in other tumor models and in designing and interpreting *in vivo* experiments.

2.3 Background

Drug delivery and distribution in tumors is a complicated interplay of local tumor physiology and drug properties. Understanding and being able to predict this distribution is imperative to developing new therapies, since poor uptake has been shown in the clinic[21] to correlate with poor outcomes. Tumor physiology is highly variable with gradients in oxygen[22], metabolic waste products[23], pH[24], differences in extracellular matrix composition[25,26], cell packing[27], interstitial pressure[28], multiple cell types[29], poor blood flow[30], increased and variable permeability[31], and heterogeneous target concentrations[32] among others. For drug properties, the dose, molecular weight, charge, target affinity and specificity, shape (e.g. globular versus linear macromolecules[33,34] or aspect ratio in nanoparticles[35]), surface chemistry (e.g. nanoparticles and antibody drug conjugates[36]), lipophilicity, pKa, local metabolism (e.g. antibody internalization), and systemic (plasma) clearance impact distribution. Even more complicated is that these effects are not independent. Increasing dose may have little effect if a growth receptor is saturated[37], for example, but have a major impact in another tumor or adjacent region with much higher receptor concentration where many receptors remain untargeted.

Tumor distribution is equally important for imaging agent development. Molecular imaging agents like radiolabeled ligands or protease sensors[38] must reach their target to bind or activate. The physiochemical properties of the agent must allow the binding or activation to dominate distribution; otherwise non-specific mechanisms such as membrane uptake may dictate the signal[39]. The requirements are even higher for quantitative imaging agents. Here, even if some of the target is exposed to the imaging agent, the resulting image may not be correlated with the amount of target[40-44]. In many cases, the imaging time will have an impact on the signal such as FDG that is limited by blood flow at early times[45] and glucose uptake and metabolism at later times[46].

Due to the complex interplay of factors determining distribution, often multiple animal experiments are conducted with a variety of agents and variable results. This method is time consuming and expensive, with no guarantee that the models used will mimic the clinical scenario. Mathematical simulations are playing a larger role in determining local distribution[47], and predictive physiologically based pharmacokinetic (PBPK) models are increasingly able to determine the organ level distribution for small molecules[48-50] and biologics[51,52]. However, assumptions that are valid in healthy tissue may fail in the tumor microenvironment. We have developed partial differential equation (PDE) models to accurately describe the distribution of molecules in tumors[47,53].

Theoretical studies by Thurber et al indicate that there are four major classes of pharmacokinetic distribution in tumors depending on the rate limiting step in uptake[53]. Molecules can be classified by 1) blood flow limitations, 2) extravasation limitations, 3) diffusion limitations, or 4) local binding and/or metabolism limitations as shown in figure 2.1. These classes are useful because they allow predictions about the impact of tumor physiology on

distribution. For example, changes in macromolecular permeability would have no direct impact on a blood flow limited agent but a major change in an extravasation-limited agent.

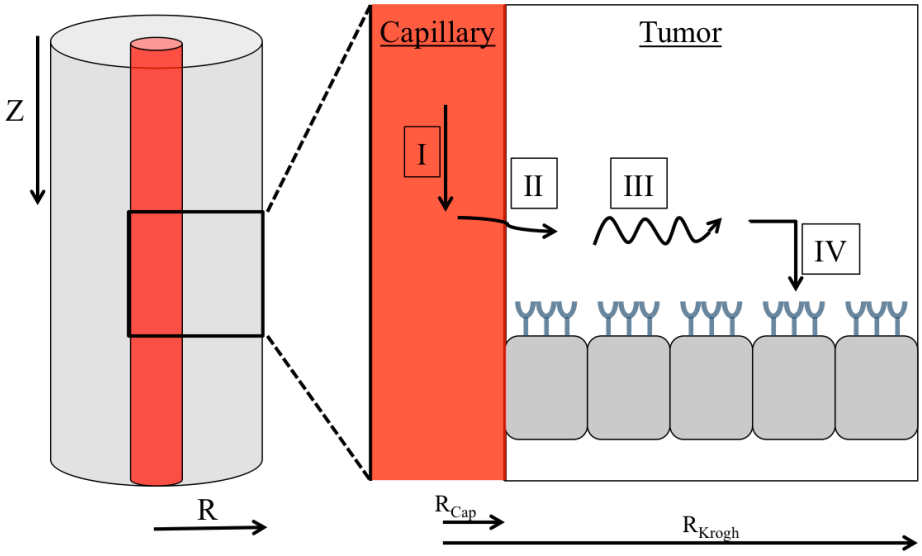

Figure 2.1 Schematic of the Krogh Cylinder Model.

(Left) Schematic of the Krogh Cylinder Model with radial (R) and axial gradients (Z). (Right) Zoomed in section shows the four classes of pharmacokinetic distribution (I) blood flow limited, (II) extravasation limited, (III) diffusion limited and (IV) local binding/ metabolism limited.

This study used multichannel imaging within the same tumor to look at different patterns of distribution. The variability within and between tumors makes it difficult to parse out the impact of drug properties versus the local microenvironment. Using multichannel imaging, several drugs and imaging agents were examined simultaneously in the same tumor to mitigate tumor microenvironment effects. The PDE model was used to predict the distribution of four molecules that displayed characteristics of the different classes of pharmacokinetic distribution. The selection criteria also ensured that these agents had different fluorescence excitation and emission profiles so they could be independently followed within a tumor. The model was also used to determine the imaging time after injection, and image analysis was used to compare the distribution with predictions.

2.4 Results

The drugs and imaging agents used in this study are listed in table 2.1 along with their properties. These were injected in nude mice with A-431 xenografts, where the vasculature is highly heterogeneous with some hyper-vascularized areas and other necrotic regions, replicating the variable tumor physiology seen in many animal models and the clinic.

Table 2.1 Physicochemical and optical properties of drugs and imaging agents.

	Target	Molecular Weight (Da)	Excitation / Emission (nm)	Plasma Protein Binding (%) ± S.D.	Plasma Clearance (Alpha fraction, Alpha half-life, Beta half-life)
Bodipy FL	-	292	502 / 511	89.7 ± 3.8	56.2% alpha 2.6 min 30.37 min
Cetuximab + AF 750	EGFR	~153,000	752 / 780	NA	58% alpha 3.0 hrs 70.3 hrs
Hoechst 33342	DNA	452	352 / 455	99.3 ± 0.4	99.5% alpha 2 min 1 hr
Hoechst 33258	DNA	424	352 / 455	98.8 ± 0.9	98.7% alpha 1.3 min 3.0 hrs
Integrisense 680	Integrin ($\alpha_v\beta_3$)	1432	675 / 693	94.9 ± 2.3	92.3% alpha 6 min 3.5 hrs

BODIPY-FL was chosen as a representative blood flow limited molecule due to its low molecular weight and relatively low plasma protein binding for a fluorophore. This agent clears quickly from the blood and does not bind to a specific target, so the agent was injected 2 min before excising the tumor to capture differences in blood flow. The BODIPY-FL dose distributed in a 1.4 mL plasma volume would give an initial concentration of 35 μM, but the measured concentration at 1 min was closer to 5 μM. This indicates that significant redistribution occurred

during the first minute between the tail vein injection and retro-orbital blood sample. Cetuximab is a chimeric monoclonal antibody used in the clinic to treat colon[54] and head and neck cancer[55]; it was selected as a representative antibody, which are generally limited by extravasation[56] due to their large size. The high EGFR expression in this line was predicted to give extravasation limited uptake at this dose of Cetuximab. Hoechst 33258 was initially discovered and developed as an anti-parasitic drug[57], but both Hoechst dyes were quickly adopted for fluorescence imaging given their cell permeability and bright nuclear signal. Hoechst 33342 has been used in tumors to track functional vessels[58,59]. Its high plasma protein binding 'buffers' the concentration within vessels so it is not depleted along the length of a tumor vessel. High cell uptake also allows it to quickly diffuse through endothelial cells, and the large number of DNA binding sites prevents it from saturating its target. Therefore, predictions show this agent to be limited by diffusion in the tissue. Hoechst 33258 has similar properties but is not taken up into cells nearly as fast as Hoechst 33342 even though they differ by only a hydroxyl versus an ethoxy group (Fig 2.2). Integrisense was originally developed as an $\alpha_v\beta_3$ integrin inhibitor for osteoporosis[60]. High specificity and affinity for its target made it an excellent imaging agent after conjugation to a fluorophore[61]. The low expression of $\alpha_v\beta_3$ in the tumor type ensured that the dose of Integrisense would be saturating making it binding/ metabolism limited.

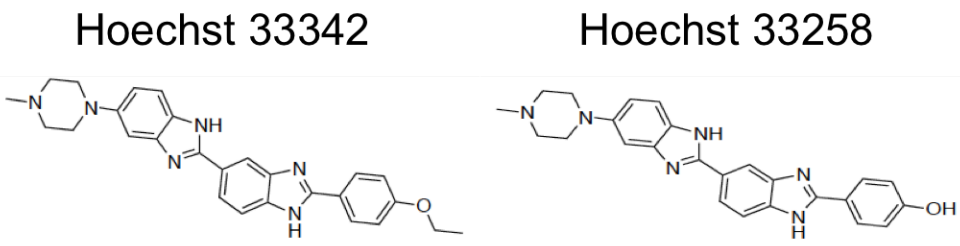

Figure 2.2 Structures of the Hoechst molecules.

The difference between the two molecules is the ethoxy group vs the hydroxyl group in the bottom right of the structures. The predicted logP of the two molecules is 4.67 and 4.07, respectively.

The full Krogh cylinder model simulates individual vessels within a tumor with gradients around the vessel (radial direction) and along the length of the vessel (axial direction) (Fig 2.1). In a tumor, slow blood flow depletes small molecules along the length of the vessel as seen with BODIPY-FL. The small size (< 300 Da) and moderate lipophilicity (predicted logP = 3) causes the molecule to distribute quickly in the radial direction. However, the local plasma concentration is quickly depleted resulting in low uptake. This is in contrast to liver tissue. Here, a much higher blood flow reduces depletion along the length of the vessel giving much higher uptake. Antibodies such as cetuximab-AF750 have a permeability that is several orders of magnitude lower than small molecules, so the slow rate of extravasation does not deplete the concentration along the length of the vessel. Extravasation limits uptake, and the molecules that do reach the tissue quickly bind their target and are immobilized. This results in a perivascular distribution (Fig 2.3). Hoechst 33342 also lacks a significant gradient along the length of the blood vessel. Although this is a small molecule like BODIPY-FL, it has much higher plasma protein binding. Binding to albumin and other proteins occurs on the millisecond time scale[62], so as free drug extravasates, bound drug dissociates from proteins to replace it. Although 89.7% versus 99.3% does not appear to be a large difference, it is the *free* drug that matters, so the ratio of free drug (10.3% versus 00.7%) results in ~15 fold more free drug for BODIPY-FL. Like Cetuximab, the large number of DNA binding sites per cell quickly immobilizes Hoechst 33342 before it diffuses deep in the tissue, resulting in a perivascular distribution. Finally, Integrisense-680 lacks both radial and axial gradients since it saturates its receptor. In the simulation, a constant receptor concentration is assumed. The large dose of Integrisense relative to the low $\alpha_v\beta_3$ expression in A-431 cells saturates the receptor within 30 minutes. The simulations for the other agents are shown at the time of tumor excision (2 min for BODIPY-FL, 24 hours for

Cetuximab, and 3 hours for Hoechst 33342), but it is shown at saturation after 30 min for Integrisense. At longer times, this agent is internalized and trapped while it clears from the background.

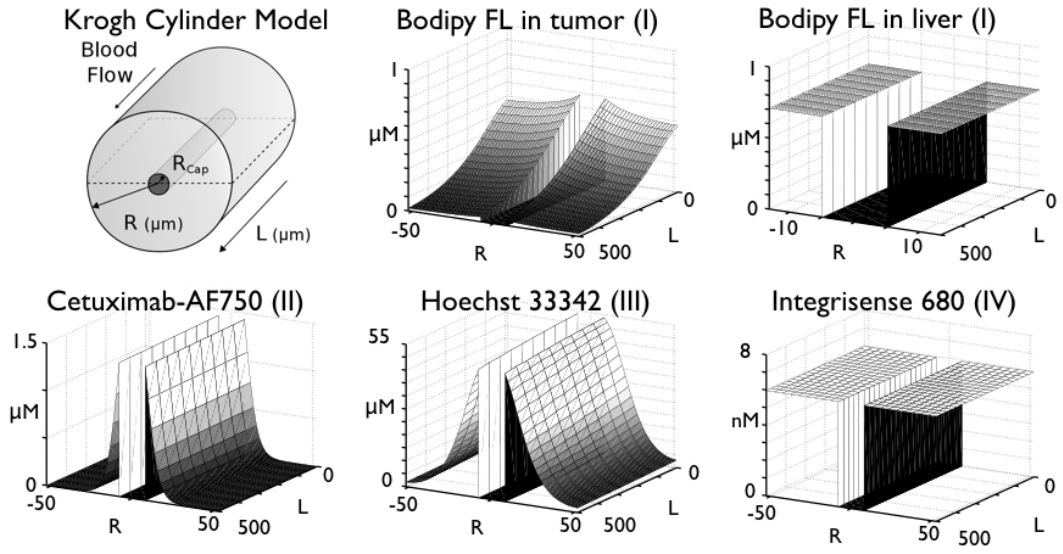

Figure 2.3 Simulations based on Krogh Cylinder Model.

The simulations show the concentrations of the drugs and imaging agent along the axial and radial gradients along with their predicted class of delivery in parentheses.

Macroscopic (stitched) images of the entire tumor were used to reconstruct the distribution of all four agents throughout the whole tumor (Fig 2.4). The BODIPY-FL signal is 8.6 times higher in the liver than the tumor ($p < 0.0001$). This is consistent with the model predictions where much higher blood flow rates occur in the liver[51]. Cetuximab demonstrates a perivascular distribution in the tumor and no detectable signal in muscle that lacks human EGFR. Hoechst 33342 also exhibits a perivascular distribution within the tumor and labels nuclei in the surrounding muscle. Integrisense 680 shows a more uniform signal throughout the tumor, although it is higher in areas composed of macrophages and lower but detectable on tumor cells. CD31 labeling of the slide with an AlexaFluor-555 labeled antibody shows vasculature

throughout the tumor and surrounding muscle. The signal in all images was higher than autofluorescence.

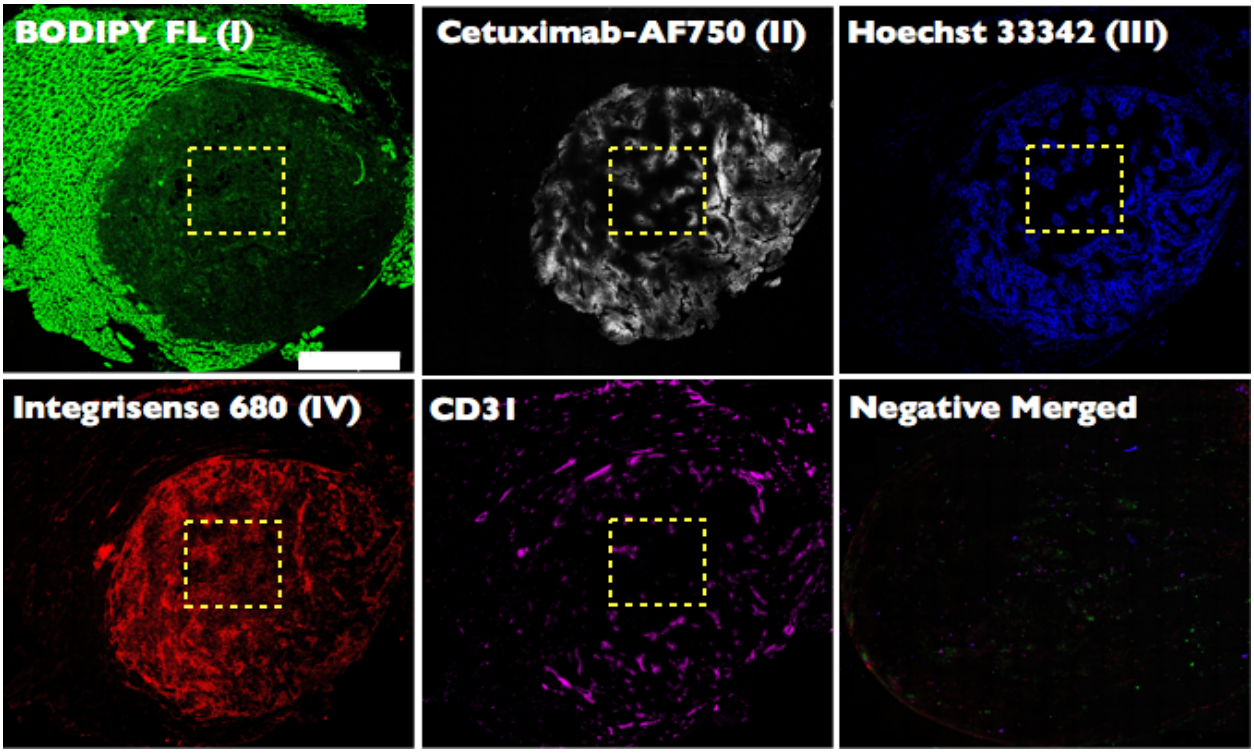

Figure 2.4 High resolution multichannel fluorescence images.

High-resolution images were stitched together to generate a whole tumor image with the class of delivery shown in parentheses. The CD31 *ex-vivo* stain label blood vessels in the tissue slice. The negative merged image is of a tumor slice with no drugs or imaging agents injected and window leveled identically to the other imager images in the figure. The yellow doted box is zoomed in in figure 2.5. Scale bar = 1000 μm.

Zooming in from the whole tumor to individual vessels, the local heterogeneity is more apparent (Fig. 2.5). BODIPY-FL cannot be detected easily since it has low tumor uptake and rapidly distributes, resulting in diffuse signal. Both Cetuximab and Hoechst 33342 show large gradients in signal around the vessels, with few but distinct examples of mismatch: both Hoechst 33342 signal without Cetuximab (yellow arrow) and Cetuximab signal without Hoechst 33342 (data not shown). Integrisense-680 shows a more diffuse fluorescence consistent with saturating binding sites.

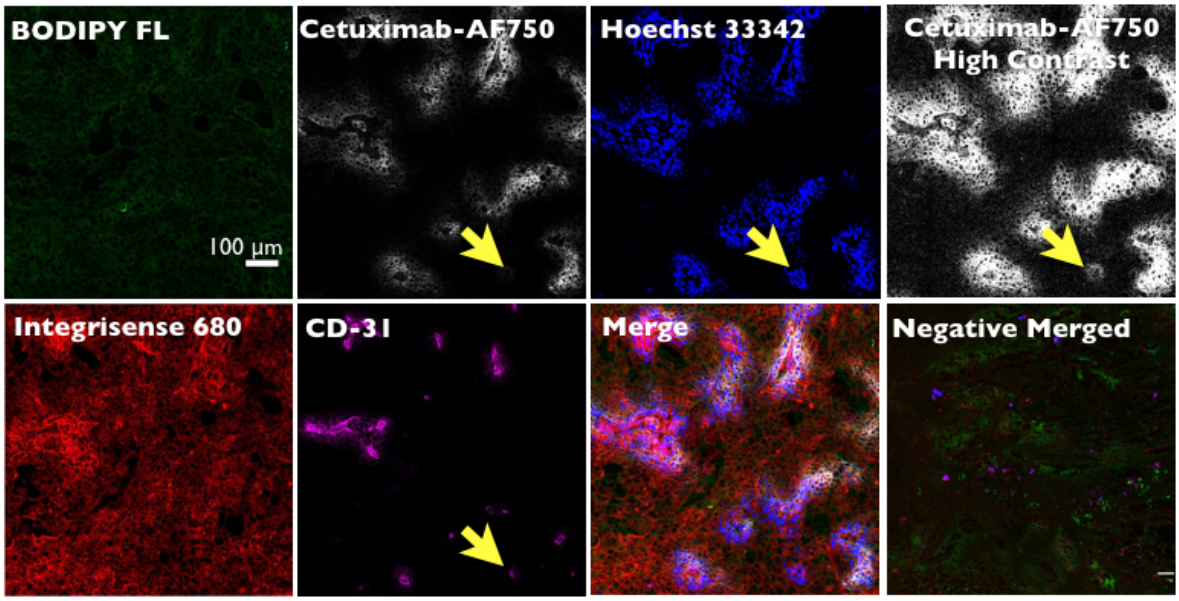

Figure 2.5 Cellular level images corresponding to the boxes in Fig. 2.4.

The yellow arrows point to a vessel, which causes prominent Hoechst 33342 staining but no apparent Cetuximab staining. Perivascular Cetuximab signal was seen only after increasing the contrast.

Hoechst 33342 uptake into cells is rapid, staining nuclei in seconds to minutes. Hoechst 33258, however, takes much longer to enter cells[63]. The nuclei reached saturation within 15 min with Hoechst 33342 but required over 2 hours in Hoechst 33258. Rapid cell uptake is predicted to quickly immobilize Hoechst 33342 near vessels, which can be seen at the macroscopic and cellular level (Fig 2.6). The slower cell uptake of Hoechst 33258 is predicted to yield a more homogeneous distribution as the drug diffuses farther into the tissue before entering cells and binding DNA. The overall tumor distribution and vessel level images capture this more uniform labeling, although the absolute signal intensity is much lower for Hoechst 33258 than Hoechst 33342.

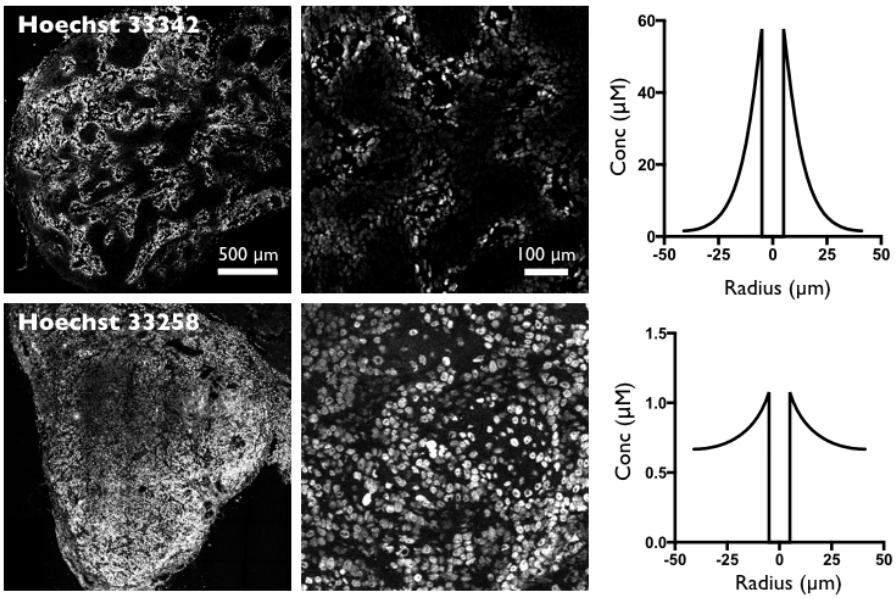

Figure 2.6 *In vivo* distribution and simulations for both Hoechst molecules.

Images and simulations for Hoechst 33342 (top row) and Hoechst 33258 (bottom row). (Left) Macroscopic whole tumor images, (center) higher resolution images and (right) radial plots predicting uptake for both molecules.

Integrisense-680 has a more uniform but faint distribution throughout the tumor. In regions primarily consisting of A-431 cells, it has a reasonably high correlation coefficient with *ex vivo* anti-$\alpha_v\beta_3$ labeling (Fig. 2.7). However, there is also a significant signal in tumor macrophages. Based on estimates of pinocytosis in macrophages[64], the signal in macrophages from fluid phase uptake is ~70% higher than the low $\alpha_v\beta_3$-expression A-431 cells. In addition, the Integrisense can bind to integrins on the macrophages.

The Cetuximab staining shows a perivascular pattern when targeted *in vivo* (Fig 2.7). *Ex vivo* labeling of the slide with a non-competitive antibody shows significantly more EGFR farther from the vessels that was not targeted by the probe. The resulting Pearson correlation coefficient is lower as a result.

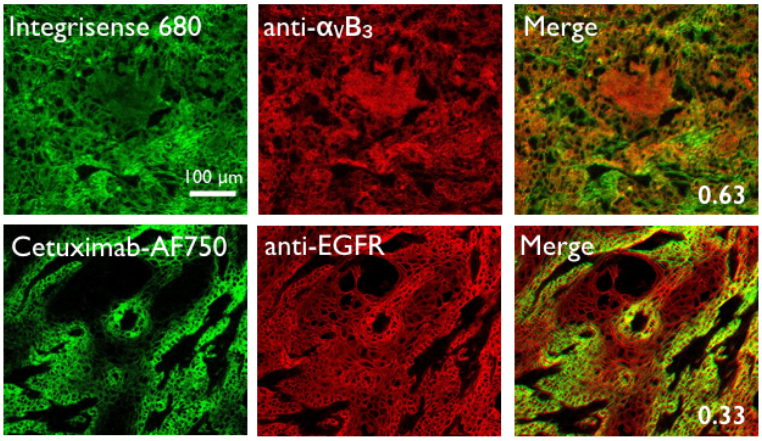

Figure 2.7. *Ex vivo* and *in vivo* stains for $\alpha_v\beta_3$ and EGFR.

Tumor sections were labeled *ex-vivo* with anti-$\alpha_v\beta_3$ (top middle) or anti-EGFR (bottom middle) AlexaFluor 555 antibody and compared to the in vivo signal (left). The Pearson correlation coefficient was high (0.63) for Integrisense 680 and lower (0.33) for cetuximab in agreement with predictions.

2.5 Discussion

Drug distribution in tumors is difficult to study due to the heterogeneity in the physiology/tumor microenvironment combined with the effects of drug properties. The variability includes both intra- and inter-tumor tissue heterogeneity as well as temporal changes. To parse out the effect of drug properties on tumoral distribution, we used multi-channel imaging within the same tumor to study the distribution of four different agents in the same tumor microenvironment. The imaging was paired with partial differential equation simulations of these agents to compare the theoretical distribution with the experimental results. Overall, there was excellent agreement with the theoretical predictions for all 5 simulated agents that varied in molecular weight, target specificity and expression, plasma clearance, and protein binding.

Mathematical models are being used increasingly to explore the impact of tumoral distribution[47]. They have several strengths including the ability to rapidly simulate a range in parameters, such as permeability or target expression, to understand the impact on distribution. Investigating these parameters solely with animal experiments would take a range of models at

increased time and cost. With mathematical simulations, parameters can be independently varied to isolate the impact of each, and values can easily be adjusted for the clinical scenario, which is ultimately the goal of the process. These mathematical models can also be used in designing focused animal experiments and interpreting the data, reducing the total number, time, and cost of these experiments while increasing confidence in the results.

The model used in this paper consists of a tissue and cellular level analysis of time dependent concentrations around blood vessels in tumors due to specific and non-specific mechanisms of uptake. Mathematically, it is a set of non-linear partial differential equations modeling the time-dependent concentration in two spatial dimensions. A graphical user interface (GUI) was developed to quickly modify the parameters used as inputs into the model (Fig. 2.8). By incorporating blood flow, extravasation, diffusion, and local binding and metabolism, a wide range of agents can be simulated and compared. This is in contrast to many models that make simplifying assumptions that limit the type of molecule that can be examined. For example, oxygen can quickly equilibrate across the blood vessel wall, but for agents such as antibodies, this would yield incorrect results. Compartmental models assume rapid diffusion through the tissue (no spatial gradients), which does not accurately capture many small molecules (e.g. doxorubicin and Hoechst 33342) and macromolecules (e.g. antibodies and nanoparticles). Models that assume uniform concentrations along the length of blood vessels (no axial gradients) may be valid for some drugs (e.g. highly plasma protein bound small molecules and biologics such as antibodies) while over-predicting uptake of small molecules with less plasma protein binding. By incorporating all the major steps in delivery to the tissue, the simulations are much more broadly applicable, and no simplifying assumptions need to be made *a priori*.

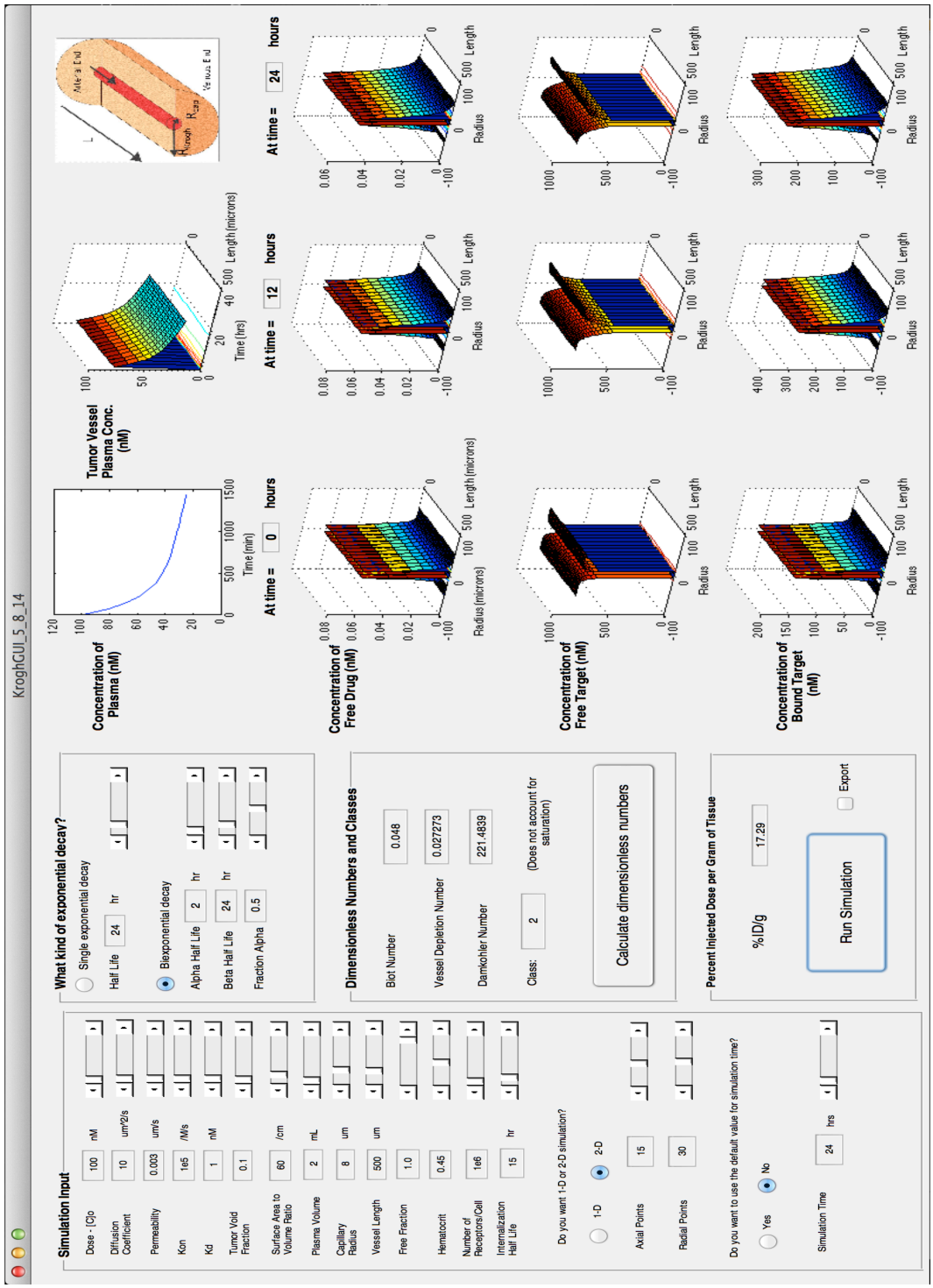

Figure 2. 8 Graphical User Interface (GUI) for Krogh Cylinder Simulations

This PDE model predicts four broad classes of pharmacokinetic distribution in tumors. The first is blood flow limited agents. This class includes many small molecules that have low plasma protein binding, so they have a large free fraction that rapidly extravasates across the vessel wall. They quickly diffuse through the tissue (no diffusion limitations) and saturate the binding sites (no binding limitations). Examples of this type of agent are many small molecules in healthy tissue[48]. Here, the non-specific uptake is based on lipophilic distribution in the tissue. This is linear with drug logP values and tissue lipid content, and therefore it never saturates (unlike class IV). The short diffusion distances result in few to no interstitial transport limitations (unlike class III), and the small size allows rapid extravasation (unlike class II). The result is that the agents are blood flow limited, and compartmental models use this assumption in their development.

Large molecules like biologics have limited extravasation between the endothelial cells, resulting in permeability limited uptake. This can be seen in validated models for biologics[51,52,56]. Here, compartmental models assumed extravasation as the rate-limiting step, and these models focus on exchange between the tissue and vascular system based on convective and diffusive mechanisms. For tumors, elevated interstitial pressure results in diffusive uptake being the dominant mechanism[65,66], but healthy tissue has significant convective extravasation and lymphatic drainage[67]. The heterogeneity often seen with antibodies can be captured with this model. The heterogeneity results due to rapid binding relative to interstitial transport (diffusion) and not directly because of low permeability. Cetuximab rapidly binds to the millions of receptors on the A431 cells before it can diffuse away from the vessel. Only after the cells adjacent to the vessel are saturated do the antibodies diffuse deeper into the tissue. Internalization and metabolism by these cells may permanently prevent this from occurring[68].

Lower affinity antibodies can dissociate and diffuse farther in the tissue resulting in more homogeneous distribution[69,70], although the rate-limiting step in uptake is still extravasation.

Diffusion limited drugs are often the least reported in the literature. These agents cannot be easily simulated with compartmental models due to the spatial gradients that develop in the tissue[71]. A typical class III agent is a small molecule (that can extravasate quickly, unlike class II) with high plasma protein binding (which buffers the free drug concentration along the length of a capillary, preventing class I designation). It may also have a non-saturable mechanism of localization (e.g. high uptake in membranes) or high target expression (DNA binding of Hoechst dyes), so it is not limited by binding or metabolism. Unlike other classes that may be either homogeneous or heterogeneous in tissue, this molecule must have spatial gradients within the tissue.

The final class of agent, class IV or binding and metabolism-limited agents, cannot be generalized based on their physiochemical properties and can encompass small molecules and macromolecules with widely varying properties. These agents saturate their binding sites with additional probe that lacks free target to engage (or enzyme for activation[64]). With no more targets (binding site limited), the extra probe intravasates back into the blood. Because of this, the uptake in a particular tissue is correlated with the number of targets, which is ideal for imaging agents. For Integrisense, a low number of targets gave a low overall signal, and increasing the number of $\alpha_v\beta_3$ binding sites in the tissue resulted in a much higher uptake in the tissue[61]. This intuitive result is often not the case for other agents such as antibodies[40]. Therefore, class IV agents are ideal for quantitative imaging.

Multichannel imaging allows the direct observation of distribution of multiple agents within the same tissue (Fig. 2.4). By stitching together images taken at high resolution, the

pattern of uptake across the entire tumor could be reconstructed. Comparing different drugs in the same tissue, the differences can be directly attributed to drug properties and not variability in the tumor microenvironment, strengthening the conclusions. BODIPY-FL was chosen as a class I agent due to its small size, relatively low plasma protein binding (for a fluorophore), and green fluorescence which did not interfere with the other three agents. The higher blood flow velocity in liver tissue (70-500 μm/s[72,73]) relative to tumors (20-200 μm /s[74]) resulted in higher uptake in the liver than in the tumor. Cetuximab-AF750 extravasated from functional vessels and gave a perivascular pattern of uptake typical of high affinity biologics against highly expressed targets[37,75,76]. Hoechst 33342 has a high level of plasma protein binding (99.3%), so it fills the functional vessels within the tumor without significant depletion and has long been used as a measure of perfused vessels[58,59]. This can be seen by comparing CD31 staining with Hoechst 33342 and cetuximab-AF750, where several CD31 stained vessels show a complete lack of Hoechst or cetuximab staining indicating the vessel had collapsed prior to injection of any of the agents. Integrisense-680 had staining throughout the tumor and lacked the perivascular pattern of cetuximab-AF750 and Hoechst 33342. The large dose injected relative to the low target expression resulted in a saturation of the binding sites and a more even distribution.

Using the high-magnification images, the pattern around individual vessels could be examined (Fig. 2.5). Within the tumor, little BODIPY-FL could be distinguished, although the average signal was statistically higher than negative control tumors ($p < 0.01$). Any probe entering the tumor quickly diffuses away from the vessel. Although we used a cross-linking agent to covalently fix the molecule to the tissue, some of the drug may have washed away before it reacted. The higher levels in the liver still resulted in significant signal for this blood

flow limited agent. The Integrisense-680 signal is higher (due to binding) and stains cells throughout the tumor, both consistent with model predictions.

Comparing the cetuximab-AF750, Hoechst 33342, and CD31 staining, there are some CD31 vessels that stain for only cetuximab or Hoechst 33342. Unlike CD31 vessels that lack both probes and are likely collapsed, staining of only one compound shows that it was functioning at some point during the experiment. Transient blood flow in tumor vessels is a well-known phenomenon where the disrupted pressure gradients result in transient cessation and even reversal of flow[77]. Cetuximab-AF750 was injected 24 hrs prior to sacrifice, while Hoechst 33342 was injected 3 hrs beforehand. It is therefore not unexpected that some vessels would stain with the cetuximab-AF750 and then stop functioning at some point before the injection of Hoechst 33342. However, since the antibody is present the entire time Hoechst 33342 is in the blood, vessels that stain only with Hoechst 33342 are not expected. The likelihood of a vessel not functioning for the 21 hrs between the injections and then suddenly functioning for a few minutes after the Hoechst 33342 injection (where the majority of uptake occurs before its rapid clearance) is also low. This has been seen in other tumor models as well with Trastuzumab antibody and DIOC7 as a vascular stain[75]. One explanation is that the injection itself, either the probe or agents in the formulation, can alter blood pressure and tumor blood flow[78], resulting in induced changes in blood flow patterns. If the contrast is increased on the cetuximab-AF750, there is staining around the vessels that initially appear to be stained only with Hoechst 33342 indicating that there was antibody in these vessels when they were delivering Hoechst 33342. Therefore, we hypothesize that the injection of Hoechst altered the tumor blood flow, resulting in these patterns and consistent with transient blood flow and model predictions.

Despite the established use of Hoechst 33342 to stain functional vessels in tumors, the kinetic rates of uptake have not been measured in much detail[79,80]. It has been reported that the uptake of a very similar dye, Hoechst 33258, is much slower. Different modes of binding and diffusion have been postulated for biologics and we wanted to see if small molecules could follow the same patterns. The modes include fast or slow binding and fast or slow dissociation. High-affinity antibodies exhibit fast association and slow release, and it appears Hoechst 33342 follows this pattern of quickly entering the cell, binding the target, and dissociating slowly. However, if Hoechst 33258 entered cells at a rate much slower than diffusion through the tissue, then it could distribute more homogeneously before entering the cells (effectively immobilized) and binding to the DNA. *In vitro* cell culture experiments showed saturation after 15 min with Hoechst 33342 versus 2 hours with Hoechst 33258, and the modeling data indicated that the Hoechst 33258 would distribute more homogeneously (albeit at a lower concentration per cell, Fig. 4). After injecting the same dose, this was exactly what was observed *in vivo*. We could not quantitatively compare the images since the intensity differences were too great to image both at the same microscopy settings (Hoechst 33342 was saturated at the settings required for Hoechst 33258). However, qualitatively, the pattern and intensity were consistent with predictions (Fig 2.6). This example, where simply switching an ethoxy group to a hydroxyl group results in such a drastic change in distribution, is one reason why predictions based exclusively on structure (and no *in vitro* experiments) remain challenging. This also provides an example where modeling helps explain a counter-intuitive situation where rapid cell uptake results in poor distribution and poor cell uptake yields a more homogeneous distribution.

The modeling for the Hoechst dyes required a separate code to accurately simulate the distribution. The code used previously for antibodies[81] and small molecules[47,53] was based on a

simplifying assumption for diffusion. Antibodies do not cross cell membranes, so diffusion occurs exclusively in the extracellular space, and the other small molecules crossed cell membranes fast enough to equilibrate between the intracellular and extracellular space relative to diffusion. The Hoechst dyes straddled these two extremes where the cellular uptake rate was on the same time-scale as diffusion in the tissue. Therefore, the cellular uptake rate had to be explicitly modeled in the equations.

For Integrisense-680, modeling predictions indicated the dose was much higher than necessary for saturation, and a low level of uptake was expected throughout the tumor. In regions primarily consisting of A-431 cells, there is a Pearson correlation coefficient of 0.55. However, in non-tumor cells, the Integrisense-680 signal is slightly higher. This could be due to $\alpha_v\beta_3$ binding sites on macrophages[82], although the antibody reportedly cross-reacts with mouse antigen. Alternatively, we calculated whether fluid phase uptake would be sufficient for the higher macrophage signal. Although particle shape[35], surface coatings[83,84], and size[85,86] affect uptake, even PEGylated molecules that have low interaction are taken up by these cells[38]. Using a previous estimate of fluid phase uptake by activated macrophages in the model[64], the predicted concentration from non-specific fluid phase uptake was twice that of the binding to A431 cells. Either binding or fluid phase uptake could contribute to the higher macrophage uptake than A431 cell uptake, but they are both consistent with a lack of transport limitations and uptake limited by local binding or (fluid-phase uptake and) metabolism.

Cetuximab-AF750 is limited by extravasation based on previous reports[34,53]. The dose used was sub-saturating, so only cells adjacent to blood vessels were labeled. This results in a lower Pearson correlation coefficient. A larger dose would saturate all the binding sites and

result in a more homogeneous distribution (and higher Pearson correlation coefficient) as shown in tumor spheroids[68] and xenografts[37,87].

One of the biggest hurdles to using models in research is the extensive effort required to develop a model and parameterize all the rates. Although software exists for compartmental models, the assumptions for compartmental models are sometimes valid and other times not[88]. To facilitate the use of this partial differential equation model, we have generated a graphical user interface (GUI) for the simulations. This allows a user to quickly simulate a wide range of agents, from small molecules to biologics and nanoparticles, without coding. The tumor physiology parameters can also be varied to study the impact on distribution in a matter of seconds, facilitating the use of the model in designing experiments and interpreting results.

2.6 Conclusion

In conclusion, we have used multi-channel imaging of four agents in a tumor and compared the distribution to a partial differential equation model. The model distinguishes four different rate-limiting steps in uptake, which has practical applications in combination therapies that normalize the vasculature[21,89], which may have synergistic or antagonistic effects. Experimentally, this group of agents could be used in conjunction with radiolabelled probes. By combining the fluorescent agents with autoradiography of an imaging agent or tritiated therapeutic, a comparison can be made between the new probe and the known fluorescent agents. This can help parse out the distribution of the radiolabelled agent due to target interaction versus the local tumor microenvironment[90,91]. Together, a combined theoretical and experimental approach can help in designing experiments, interpreting animal results, and developing improved therapeutics and imaging agents.

2.7 Experimental Methods

Mathematical model

The mathematical simulations were based on a previously published model[53]. Briefly, the model consists of non-linear partial differential equations with axial and radial gradients around a Krogh cylinder representation of tumor vessels. Time-dependent mixed boundary conditions determine the extravasation and depletion along the length of the vessel, and diffusion across a pseudo-homogeneous tissue with saturable binding and local metabolism dictate the tissue distribution. Equations are solved using finite differences in MATLAB (Mathworks), and a sparse Jacobian is specified to reduce computation time. Parameterization is also challenging with literature values often sparse and sometimes contradictory, especially for small molecules where equilibrium values are more readily available than kinetic rates. A table of parameters used in the predictions is listed in the supplementary data.

Differential equations for Graphical User Interface simulations:

1. $$\frac{\partial C_{total}}{\partial t} = D_{eff}\left[\frac{1}{r}\frac{\partial C_{total}}{\partial r} + \frac{\partial^2 C_{total}}{\partial r^2} + \frac{\partial^2 C_{total}}{\partial z^2}\right] - \frac{k_{bind}}{\varepsilon} C_{total}(T_0 - B) + k_{release}B$$

2. $$\frac{\partial T_{overall}}{\partial t} = R_s - \frac{k_{bind}}{\varepsilon} C_{total}(T_0 - B) + k_{release}B - k_e(T_0 - B)$$

3. $$\frac{\partial B_{overall}}{\partial t} = \frac{k_{bind}}{\varepsilon} C_{total}(T_0 - B) - k_{release}B - k_e B$$

4. $$\frac{\partial C_{plasma}}{\partial t} = -v\frac{\partial C_{plasma}}{\partial z} - \frac{2P}{(1-H)R_{cap}}\left(f_{free}C_{plasma} - \frac{C_{total}}{\varepsilon}\right)$$

Boundary conditions:

1. $$\left.\frac{\partial C_{total}}{\partial r}\right|_{r=R_{Krogh}} = \left.\frac{\partial C_{total}}{\partial z}\right|_{z=0} = \left.\frac{\partial C_{total}}{\partial z}\right|_{z=L} = 0$$

2. $$D_{eff}\left.\frac{\partial C_{total}}{\partial r}\right|_{\square=R_{cap}} = P\left(f_{free}C_{plasma} - \frac{C_{total}}{\varepsilon}\right)$$

3. $C_{plasma}\big|_{z=0} = C_{plasma,0}\left(Ae^{-k_\alpha} + (1-A)e^{-k_\beta}\right)$

4. $\frac{\partial C_{plasma}}{\partial z}\Big|_{z=L} = 0$

Initial conditions:

1. $C_{total} = B_{overall} = C_{plasma} = 0$

2. $T_{overall} = T_0$

Mathematical equivalence of epsilon (void fraction) and R (immobile fraction)

$C_{immobile} = RC_{free}$

$C_{total} = C_{immobile} + C_{free} = C_{free}(1 + R)$ and $C_{free} = \frac{C_{total}}{1+R}$

Assuming only the free fraction can diffuse and bind. The concentrations are in terms of total drug, so total drug concentrations are divided by 1+R.

For antibodies and other biologics that cannot enter cells, the total tissue concentration (moles per total tissue volume) is averaged over both intracellular and extracellular space. Since the molecules are confined to the extracellular space, the effective concentration is higher than the total average, so the total concentration is divided by epsilon.

$$C_{effective} = \frac{C_{total}}{\varepsilon}$$

While the terms both convert the total tissue averaged concentration to an effective concentration, they have opposite effects on the magnitude. The void fraction, epsilon, varies between 0 and 1, so dividing by this value increases the effective concentration. For small molecules that are often highly immobilized to proteins and membranes, the free concentration is often lower than the total concentration, and R is generally much larger than 1. This is analogous

to how the volume of distribution can be much larger than the tissue volume of a small molecule drug, since the free concentration can be a small fraction of the total concentration.

Note that the effective diffusion coefficient must still be adjusted by the immobile fraction (relative to the diffusion coefficient when all the drug is free in solution):

For the diffusion coefficient, it is assumed that whatever fraction is bound to proteins or taken up by membranes is the same inside and outside the cell. It is also assumed that this binding happens immediately in the extracellular compartment, so the effective diffusion coefficient is scaled by the factor R. This also occurs for the boundary condition, so the free drug able to intravasate is adjusted by R.

From Crank[92]:

$$\frac{\partial C_{free}}{\partial t} = D\nabla^2 C_{free} - \frac{\partial C_{immobile}}{\partial t}$$

$$\frac{\partial C_{free}}{\partial t} = \frac{D}{1+R}\nabla^2 C_{free}$$

Multiply both sides by the constant (1+R):

$$\frac{\partial C_{free}(1+R)}{\partial t} = \frac{D}{1+R}\nabla^2\{(1+R)C_{free}\}$$

$$\frac{\partial C_{total}}{\partial t} = \frac{D}{1+R}\nabla^2 C_{total} = D_{eff}\nabla^2 C_{total}$$

Differential equations for Radial Only simulations

1. Free Extracellular Drug

$$\frac{\partial C_{ext,overall}}{\partial t} = D_{eff}\left(\frac{1}{r}\frac{\partial}{\partial r}\left(r\frac{\partial C_{ext,overall}}{\partial r}\right)\right) - k_{in}\frac{(1-\varepsilon)}{\varepsilon}C_{ext,overa\square l} + k_{out}C_{int,overall}$$

2. Intracellular Drug

$$\frac{\partial C_{int,overall}}{\partial t} = k_{in}\frac{(1-\varepsilon)}{\varepsilon}C_{ext,overall} - k_{out}C_{int,overall} - \frac{k_{on}}{(1-\varepsilon)R}(T_{0,overall} - B_{overall})C_{in\square,overall} + k_{off}B_{overall}$$

3. Bound Drug

$$\frac{\partial B_{overall}}{\partial t} = \frac{k_{on}}{(1-\varepsilon)R}(T_{0,overall} - B_{overall})C_{int,overall} - k_{off}B_{overall}$$

Boundary Conditions

1. $\left.\frac{\partial C_{ext,overall}}{\partial r}\right|_{r=R_{Krogh}} = 0$

2. $D_{eff}\left.\frac{\partial C_{ext,overall}}{\partial r}\right|_{r=R_{cap}} = P\left(f_{free}C_{plasma} - \frac{C_{ext,overall}}{\varepsilon(1+R)}\right)$

Initial Conditions

1. $C_{ext,overall} = C_{int,overall} = B_{overall} = 0$

Summary of Parameters for Simulations

Bodipy FL

In vitro live cell imaging showed the intracellular signal of BODIPY-FL was twice that of the extracellular signal, so epsilon was set to 2. The hydrodynamic radius for BODIPY-FL is ~85% that of olaparib-BODIPY FL. Scaling the permeability from Thurber et al. 2014 between olaparib-BODIPY FL and oxygen, this results in a 20 um/s permeability. For simulations in the liver, the velocity was set to 70 μm/s[73]. The value did not change for higher flow rates of 0.5 mm/s [72]. An equivalent residence time occurs for a velocity of 25 μm/s and vessel length of 180 μm, which was used in the GUI.

Hoechst 33342 – Full Krogh cylinder simulation

For the cellular uptake model (radial distribution only), the on rate is calculated assuming all of the drug can bind to the target. (For example, assuming instant equilibration between the total extracellular concentration and intracellular concentration, the intracellular concentration is

increased by a factor of R over the total extracellular concentration (bound plus free). This is divided by R to result in a rate based on the total extracellular concentration. For the full Krogh cylinder model, only the free drug can bind, so for consistency with the radial distribution model, the Krogh cylinder model on rate has to be multiplied by the bound to free ratio, R, which is equivalent to epsilon.

The permeability was scaled using a hydrodynamic radius of 0.7 nm from Schmidt et al. 2009 and permeability from Thurber et al. 2014

Integrisense-680

Permeability is based on 1.432 kDa molecular weight, Schmidt et al. conversion to hydrodynamic radius and permeability.

The tumor is saturated after 30 min, but imaged after 24 hrs when most of the probe has been internalized. To show the saturation, the simulations are run for 30 min.

Table 2.2 Parameters for Krogh Cylinder Simulations

	Bodipy FL in Tumor	Cetuximab-AF750	Hoechst 33342	Integrisense 680	Hoechst 33342 (radial only)	Hoechst 33258 (radial only)
Dose	50 nmol	30 ug	300 ug (15 mg/kg)	2 nmol	300 ug (15 mg/kg)	300 ug (15 mg/kg)
C_0	4.54 μM*	143 nM*	348 μM**	1.4 μM	348 μM**	343 μM**
Diffusion Coefficient	40 um^2/s	10 um^2/s	100/80 um^2/s	40 um^2/s	200/80 um^2/s	200/20 um^2/s
Permeability	20 um/s	0.003 um/s	10 um/s	0.3 um/s	4.7 um/s	0.46 um/s
k_{on}	NA	10^5/M/s	ε*15000 /M/min or $2x10^4$/M/s	10^5/M/s	15000 /M/min	500 /M/min
k_{in}	NA	NA	assume instant equilibration	NA	1.5/min	0.25/min
K_d	NA	0.3 nM	1.42 nM[93]	4.1 nM	1.42 nM[93]	1.42 nM[93]
Epsilon (ε)	2*	0.2	80	0.4	80**	20**
S/V	60/cm*	60/cm*	60/cm*	60/cm	60/cm*	60/cm*
Plasma volume	1.4 mL	1.4 mL	1.4 mL	1.4 mL	1.4 mL	1.4 mL
Capillary radius	8 μm	8 μm	8 μm	8 μm	5 μm	5 μm
Vessel Length	500 μm	500 μm	500 μm	500 μm	NA	NA
Fraction Bound	89.7% +/-3.8%*	0	99.3% +/-0.4%*	94.9% +/-2.3 *	99.3% +/-0.4%	98.8% +/-0.9%* (high affinity to albumin[94])
Hematocrit	0.45	0.45	0.45	0.45	0.45	0.45
Receptors/ cell	0	4 $x10^6$	85$x10^6$ (ref [95])	10^4 (ref [96])	85$x10^6$ (ref [95])	85$x10^6$ (ref [95])
k_e	NA	1.9e-4/s or 4.4e-6/s***	0	1.3e-5/s or 4.4e-6/s[97]	k_{in} /R	k_{in} /R
Fraction alpha	0.562*	0.56*	0.995[98]	0.92[97]	0.995[98]	0.987*
Alpha half life	2.6 min*	3 hr*	2 min[98]	6 min	2 min[98]	1.3 min*
Beta half life	30.4 min*	70 hr*	1 hr[98]	210 min	1 hr[98]	3.0 hr*
Simulation time	2 min	24 hrs	3 hrs	30 min	3 hrs	3 hrs

*Measured
**Calculated
*** Cy5 Dye is trapped within cells for ~44 hr half life

For Bodipy FL in liver, the only differences were that the S/V was 580/cm and vessel length was 180 μm.

Cell lines and Imaging Agents

A-431 cells were obtained from ATCC (Manassas, VA). Cetuximab (Bristol-Myers Squibb; Princeton, NJ) was conjugated with Alexa Fluor 750 (Life Technologies; Eugene, OR) according to the manufacturer's instructions. Anti-mouse CD31 (Biolegends; San Diego, CA; Cat. No. 102402) and anti-EGFR (R&D Systems; Minneapolis, MN; Cat. No. AF231) antibodies were labeled with Alexa Fluor 555 (Life Technologies; Eugene, OR) in a similar manner. Integrisense-680 (Perkin Elmer, Waltham, MA), Hoechst 33342, Hoechst 33258, and BODIPY-FL propionic acid (Invitrogen, Grand Island, NY) were used without further purification.

Plasma protein binding of Integrisense-680, Hoechst 33342 and 33258, and BODIPY-FL propionic acid were measured using a Rapid Equilibrium Dialysis (Thermo Scientific; Rockford, IL) plate according to the manufacturer's instructions. Mouse plasma (Innovative Research) was mixed with either 20 μM BODIPY FL, 50 μM of Hoechst dye, or 1 μM for Integrisense 680. After equilibration, the buffer in each chamber was adjusted to 50/50 mouse plasma and PBS to eliminate effects of protein binding on fluorescence. The signal was measured using either a SpectraMax M5 Microplate (Molecular Devices; Sunnyvale, CA) reader or Odyssey CLx (Licor; Lincoln, NE).

In vitro experiments

A-431 cells were plated overnight in 96-well plates. Hoechst dyes were diluted with L-15 media (without phenol red) and 10% FBS to concentrations of 10 and 100 μg/ml each. A Microplate reader maintained at 37°C was used to measure fluorescence (excitation 350 nm, emission 450 nm), and the signal was background subtracted using wells with no cells. Experiments were conducted in triplicate, averaging 5 wells each time.

The kinetic rates of cellular uptake were determined by using a two-compartment model to fit the experimental data shown below. The probe was assumed to cross the plasma membrane by passive diffusion[79,80] into an intracellular compartment and then transport to the nucleus and bind the DNA. When combining with the PDE model, the intracellular probe was considered immobile.

Assumptions:

1) Extracellular concentration is constant

2) Equilibrium is maintained between intracellular free drug and intracellular membrane bound drug

3) Amount of target (DNA) is constant (T_o=T+B)

The final equations used to model the system are:

$$\frac{\partial C_i}{\partial t} = k_{in}\, C_e - k_{out}\, C_i - \frac{k_{on}\, k_{out}}{k_{in}} C_i\, T_o + \left(k_{off} + \frac{k_{on}\, k_{out}}{k_{in}} C_i\right) B$$

$$\frac{\partial B}{\partial t} = \frac{k_{on}\, k_{out}}{k_{in}} C_i\, T_o - \left(k_{off} + \frac{k_{on}\, k_{out}}{k_{in}} C_i\right) B$$

where, C_i and C_e (M) are the drug concentrations in the intracellular and extracellular compartment; k_{in} and k_{out} (min^{-1}) are the rates of cellular uptake and loss of the drug from the cell; k_{on} and k_{off} ($M^{-1}\ min^{-1}$) are the binding and dissociations rate constants, respectively; and T_0, T, and B (M) are total, unbound, and bound target sites (DNA), respectively. The solution to these equations was fit to the experimental data to determine the rate constants using fmincon constrained optimization algorithm in MATLAB (Mathworks; Natick, MA).

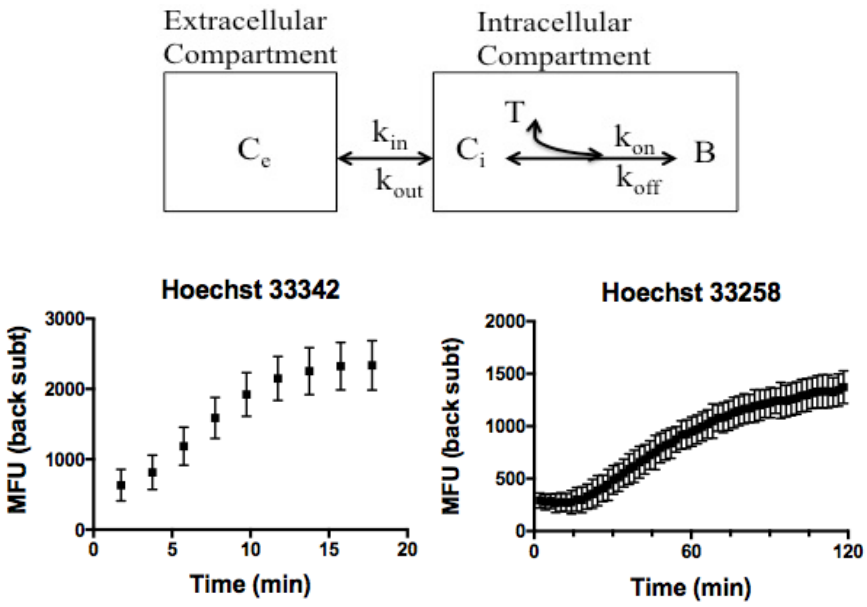

Figure 2.9 Cellular uptake model and experimental data for both Hoechst molecules

(Top) Two compartment model used to derive the coupled ODE's for Hoechst uptake. (Bottom) *In vitro* cellular uptake data for both molecules. MFU = Background subtracted mean fluorescence units.

In-vivo Experiments

A-431 cells were used to grow tumor xenografts in nude mice (Jackson Laboratory; Bar Harbor, ME). All experiments involving mice were conducted in compliance with the University of Michigan University Committee on Use and Care of Animals (UCUCA). The cells were harvested using Trypsin-EDTA (0.05%), resuspended in PBS at a concentration of 1.5 million cells/50 µL, and injected subcutaneously in each hind limb while the mouse was anesthetized using isoflurane at 2% and 1 L/min oxygen. When the longest axis of the tumor was 5–10mm, 0.2 nmoles of Cetuximab and 2 nmoles of Integrisense 680 were injected intravenously 24 hours before euthanizing the mouse. 15 mg/kg of Hoechst 33342 or 33258 and 50 nmoles of Bodipy FL were injected 3 hours and 2 minutes before euthanizing, respectively. The tumors were then

resected along with the liver, snap frozen in OCT compound using isopentane cooled with dry ice. The tumors and liver were sectioned into 6 μm slices on a cryostat.

Slides were imaged using an upright Olympus FV1200 confocal microscope equipped with 405, 488, 543, 633 and 750 nm laser lines. High-resolution images of the entire tumor were created by stitching together individual images taken with a 20X objective and a motorized stage. Since BODIPY-FL was the only drug not bound to a target, these slides were pretreated with Ethyl-3-[3-dimethylaminopropyl] carbodiimide (EDC) (Sigma Aldrich; St. Louis, MO) before imaging this channel. 75 μl of a 0.5M solution of EDC in PBS was added to the tissue for 15 min followed by a 3x3 minute wash with PBS.

For *ex-vivo* labeling of EGFR, slides were incubated with 75 μl of a 20 nM solution of Alexa Fluor 555 conjugated anti-EGFR antibody at room temperature for 25 minutes followed by a 3x3 minute wash with PBS. The anti-mouse CD31 antibody was imaged in a similar manner. For integrin staining, slides were incubated at room temperature for 25 minutes with 75 μl of a 20 nM solution of a primary anti-$\alpha_v\beta_3$ antibody (R&D Systems; Minneapolis, MN; Cat. No. MAB 3050), followed by a 3x3 minute wash in PBS, 15 minute incubation in 75 μl of a 40 nM solution of the secondary anti-rabbit-TRITC (Sigma Aldrich; St. Louis, MO; Cat. No. T6778), 3x3 minute wash, and imaged. JACoP, a plug-in in FIJI, was used to analyze the *in-vivo* and *ex-vivo* labeling and generate a Pearson correlation coefficient[99].

Plasma Clearance

Plasma clearance studies of the drugs were conducted on C57BL/6J mice. The agents were dissolved in 75 μl of PBS and injected intravenously via the tail vein. Samples were obtained retro-orbitally or from the saphenous vein using heparin coated capillary tubes. 10 μl of

the blood was mixed with 20 µl of PBS-EDTA and centrifuged to remove cells. Plasma was pipeted into a 384 well plate, and the signal was measured on a Microplate reader or Odyssey.

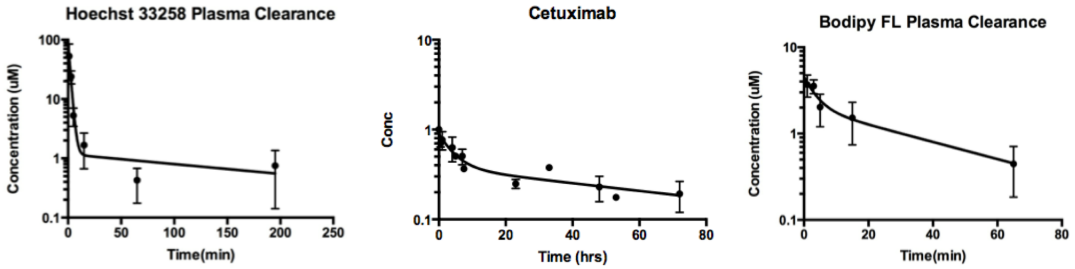

Figure 2.10 Plasma clearance curves for Hoechst 33258, Cetuximab and Bodipy FL.

Chapter 3: Orally Available Near Infrared Imaging Agents

3.1 Publication Information

Bhatnagar S, Verma KD, Hu Y, Khera E, Priluck A, Smith DE, Thurber GM 2018. Oral Administration and Detection of a Near-Infrared Molecular Imaging Agent in an Orthotopic Mouse Model for Breast Cancer Screening. Molecular pharmaceutics 15(5):1746-1754.

Modifications have been made to the published document to adapt the content to this dissertation.

3.2 Abstract

The early detection of diseases can have a profound impact on patient outcomes. Annual screenings in high-risk populations can assist in the early detection of these diseases but the implementation of annual screenings can be an issue with low compliance rates. The development of a technique, as proposed in this dissertation, of orally available near infrared imaging agents can help improve compliance rates, as the technique is completely non-invasive and safe with the use of non-ionizing radiation. The reason this technique is novel and has not been developed earlier is that orally available agents and imaging agents have very different properties. Orally available agents generally have low molecular weights and are lipophilic whereas imaging agents have higher molecular weights and are hydrophilic. This chapter deals with the synthesis of five different imaging agents to determine the combination of properties that would allow for an efficient orally available imaging agent. Out of the five imaging agents

studied, the IRDye800CW agent had good physicochemical properties and sufficient oral absorption to have promise in the detection of diseases in mouse models.

3.3 Background

The ability to non-invasively detect sites of disease for early diagnosis and treatment remains a desirable but elusive goal in medicine. In cancer, for example, detection of stage 1 cancers is associated with a greater than 90% 5-year survival rate, and identification of premalignant lesions often results in a cure[1], providing a strong incentive for early detection. Two of the standard methods of detection involve minimally invasive blood tests and medical imaging[100], each with benefits and drawbacks. Blood tests generate large amounts of molecular information but lack spatial information to identify the source of the biomarker. Imaging modalities can pinpoint precise locations but typically only yield anatomical data. Molecular imaging modalities can provide both, but these involve radiation and/or high cost, prohibiting their use in widespread screening of healthy populations with low incidence rates[101]. Orally available near infrared imaging agent have significant advantages over both blood testing and current clinical imaging modalities. This technique can be used for completely non-invasive, non-ionizing molecular imaging for disease diagnosis.

A primary advantage of blood tests is the comprehensive sampling of body tissues due to the efficient exchange of molecules within the circulatory system. However, this also serves as a major drawback. The lack of spatial information requires identifying molecules specific to the site of disease, and the large dilution of biomarkers in the systemic circulation and interstitial fluid requires exquisite sensitivity that until recently precluded bedside diagnosis[102,103]. Variability in secretion, metabolism, and excretion rates further erodes the sensitivity and specificity of blood tests, particularly for the early diagnosis of cancer[104]. Despite the tremendous

incentive to develop methods for early detection, these drawbacks have so far eluded attempts at generating a universal blood screening test for cancer[105,106].

Medical imaging covers a suite of modalities including X-rays, X-ray computed tomography (CT), magnetic resonance imaging (MRI), ultrasound (US), nuclear imaging (positron emission tomography - PET and single-photon emission computed tomography - SPECT), and non-ionizing radiation (near-infrared fluorescence and spectroscopy). Compared to blood tests, these methodologies yield precise spatial information from centimeter down to subcellular resolution[107]. However, these modalities lack the molecular information provided by blood tests, hampering their sensitivity and specificity.

Molecular imaging provides the promise of combining spatial and molecular information[10]. However, the prevalent use of ionizing radiation in these techniques (PET and SPECT) makes the cost-benefit ratio inappropriate for widespread screening of diseases with low incidence rates without pre-selection[108,109]. While progress is being made, safer alternatives that lack ionizing radiation such as microbubbles in ultrasound[110,111] and nanoparticle MRI contrast[112] have yet to provide large-scale clinical applications in screening. Topical applications reduce systemic exposure to the probe but are restricted to certain tissues and surgical applications[113-115]. The high costs of several screening modalities, such as PET, SPECT, and MRI, can also be prohibitive in large populations when incidence rates are low[109,116].

Near-infrared light has been used for several decades as both a research tool and in clinical applications. Introduced in the 1950's[117], indocyanine green is employed as a fluorescence marker in the clinic, primarily as a vascular agent due to its high plasma protein binding and hepatic clearance indicator due to exclusive removal by the liver into the bile[118-121]. Recently, NIR imaging has garnered increased attention as fluorescent dyes and imaging

equipment have become more prevalent and commercially available[122]. The photophysical properties of fluorescence can also be leveraged to provide mechanistic and microenvironmental details[38,123-127]. While visible light can generally only penetrate several cell layers into tissue before scattering and absorption degrade the signal intensity, NIR light in the 650 – 900 nm 'window' can penetrate centimeters into tissue with much lower scattering and absorption[17,19]. Scattering and absorption (primarily from hemoglobin) of NIR light has long been used for non-invasive measurement of blood oxygenation and is currently being investigated for detection of oral and breast cancers[128,129] and functional mapping of the brain surface[130] in the clinic. Importantly, the autofluorescence signal from tissue in the NIR window is extremely low, providing high sensitivity and target-to-background ratios (TBR) even with low signal from deeper inside tissue[16,17,19,131]. Recently, time resolved fluorescence imaging has been used to image cerebral blood flow underneath the skull for stroke detection[132,133] and through the hand for early diagnosis of rheumatoid arthritis[134,135].

NIR techniques have similar challenges for screening that are faced by other imaging modalities. Applications that do not use exogenous probes are primarily detecting anatomical (histological) changes that may be confounded by inflammation, fibrosis, or other benign conditions for cancer screening. Imaging probe-based techniques can target specific disease-associated molecules, but the invasive delivery mechanism (e.g. intravenous infusion of ICG) are better suited to populations with a high probability of benefit[136] (such as a cancer or stroke patient). NIRF has been successfully used in angiograms of the eye[137], imaging the cerebrospinal fluid[138], hepatic function[19], and colon polyp identification[19,115], among several others. One rapid area in growth is the development of intraoperative imaging agents for more complete resection of tumors and visualization of vascular and nerve tissues for surgical guidance[139-143]. However,

intravenous delivery is not conducive to widespread screening of large populations with low incidence. The other feasible routes of administration are oral and sub-cutaneous, which would allow patients to self-administer the imaging agent.

The advantages of oral over intravenous or subcutaneous administration can be grouped into three categories: safety, cost, and compliance (Table 3.1). Although the risk of serious reactions to imaging agents is low (e.g. 0.05-0.2% for moderate to severe reactions from ICG[144] and 0.01-0.2% for severe reactions to iodine contrast agents[145]), these can still be unacceptably high when testing a large and potentially healthy population. For reference, there are ~40 million mammograms in the US each year[146]. Oral delivery is generally the safest route and can sometimes drive tolerance rather than sensitivity. The cost of intravenous and subcutaneous administration is generally higher given the requirement for sterile delivery. This is particularly acute for intravenous delivery, where the additional medical costs of personnel administration and monitoring can far outweigh any change in the cost of materials that are ~$1 per day for small molecule drugs or cents per day with generics[147]. In addition, patients strongly prefer SC delivery to IV (91.5%[148]) and oral delivery to SC (93%[149]). Medical personnel also prefer SC delivery due to fewer complications than IV[148]. Finally, the finite clearance rate of imaging agents often requires a waiting period of several hours after administration such as folate-targeted agents[139] and ICG[150,151]. Given the low compliance rates for mammography without required multiple visits (e.g. first visit for intravenous administration and safety monitoring followed by a second visit for imaging) or an extended visit (remaining at the imaging location for several hours), this could severely compromise compliance.

Table 3.1 Criteria of selecting route of administration

	Intravenous (IV)	Subcutaneous (SC)	Oral (PO)
Safety	Allergic reactions seen more often after parenteral than oral delivery (e.g. penicillin, iron supplements[152,153])**		Generally considered safest route; often used for de-sensitization[154]
Cost	Highest – sterile material, medical supervision, low material cost	Moderate – sterile material, possible training, low material cost	Low – no training or monitoring by medical personnel, moderate material cost
Compliance* patient preference	91.5% of patients prefer SC administration to IV[148]	93% of patients prefer PO delivery to SC[149]	Preferred route of administration by patients.
Compliance* logistics	Extended visit (multiple hours) or two separate visits required	Self-administration feasible, but may require training	Simple self-administration, no training required

* - US compliance rates (without any imaging agent administration) range between 70-80%[155]
** - Anaphylaxis is a life-threatening condition that can present within minutes to hours after exposure[156]. May require monitoring particularly after intravenous administration.

Most of the above mentioned benefits are exclusive to administration for screening purposes in a healthy population. For patients undergoing potentially life-saving surgery like cancer resection, the required hospitalization and monitoring mitigates the cost-benefit ratio for oral delivery. Likewise, the cost of intravenous delivery relative to surgery is negligible. Compliance rates may still favor oral delivery if the patient needs to make multiple visits to the hospital, but administration immediately before surgery or during a preoperative visit would lower this benefit.

One major reason why oral administration of molecular imaging agents has never been reported previously is the disparate physicochemical properties required for oral absorption versus efficient targeting. It is widely appreciated that high oral bioavailability for drug-like compounds requires low molecular weight (< 500 Da) and high lipophilicity[157]. In contrast, efficient targeting agents often favor higher molecular weights for specific binding and low

lipophilicity to reduce off-target interactions. Hydrophilic molecules are generally poorly absorbed, and negatively charged drugs have even worse absorption. For example, the FDA approved drug, alendronate, has only 0.7% oral bioavailability in humans (0.2% in mice) despite its small size (250 Da)[158]. Aside from bioavailability, the binding affinity and retention of these molecular imaging agents must be high enough to target the receptor and be retained over the long period of time between the absorption/clearance phase and imaging. Overall, orally delivered molecular imaging probes require stability in the gut, intestinal absorption, low first-pass extraction in the liver, efficient targeting from the systemic circulation, background clearance, and compatible optical properties for detection at clinical depths

In order to overcome the significant challenges of orally delivering imaging agents, we developed a series of imaging agents with the same targeting ligand and varying NIR fluorophores to create imaging agents with a wide range of physicochemical properties. Testing these *in vitro* and *in vivo* helped determine what properties were most important for orally available imaging agents.

3.4 Results

The criteria in table 3.2 were selected for our proof-of-concept studies. While not all these criteria are necessary for developing orally administered molecular imaging agents, they were used to provide the highest chance of success in the shortest development time. We selected a low molecular weight targeting ligand against integrin receptors. This extracellular target has high expression on several cell types (e.g. in cancer - activated endothelium, macrophages, and tumor cells) for robust expression. Importantly, the target also internalizes with a sufficient rate for trapping the imaging agent over extended periods of time. This target also has a series of

targeting ligands developed against it for therapeutic purposes[60,159-162]. Many of these agents have gone through rounds of medicinal chemistry optimization for high oral bioavailability such as chemical stability in the GI tract, low first-pass metabolism, moderate plasma protein binding, and low toxicity. This agent has also been shown to maintain targeting following conjugation to several fluorophores[97], allowing us to manipulate the physicochemical properties while maintaining target binding[163].

Transport analysis indicates these molecules are likely binding-site and internalization limited[164] meaning that reducing protein binding/colloidal interactions is not as important as permeability surface area product (PS/V) limited agents. Plasma protein binding also impacts systemic clearance rates, which determines the absolute uptake in target and non-target tissues. Because the background signal from these agents is close to autofluorescence, a reduction in total signal may lower the target signal while the background does not decrease significantly (because it is dominated by tissue autofluorescence), thereby lowering the target to background ratio. Therefore, plasma protein binding in this scenario increases the contrast.

Table 3.2 Target and ligand selection design criteria

	Criteria	Rationale
Target Selection (Integrin)	Extracellular target	Easily accessible from blood and rapid washout of unbound probe
	High expression in several cell types (tumor cells, macrophages and activated endothelium)	Robust detection for screening and sensitivity with NIR imaging[107]
	Internalizes probe at a significant rate	Lowers the required affinity[165]
	Well studied ligands against target	Circumvent the molecular screening step
Ligand Selection (Peptidomimetic)	Low molecular weight	Increase the oral absorption
	High stability	Prevent protease and/or acid degradation in GI tract to increase oral absorption

	Low toxicity	Maintain large safety margin for screening potentially healthy patients
	Low first pass metabolism	Low liver uptake/metabolism to increase oral absorption
	High affinity, maintained after conjugation with fluorophores	Enable efficient and specific targeting even with variable plasma concentrations

Imaging Agent Synthesis

The structure of the peptidomimetic (2) and reaction scheme to generate the imaging agents (3) are shown in Fig. 3.1. The fluorophores selected used in this study were IRDye 800CW, Alexa Fluor 680 (AF680), Sulfo-cyanine7 (Sulfo-cy7), CellTrace Far Red DDAO (DDAO) and Bodipy 650/665-X (Bodipy650).

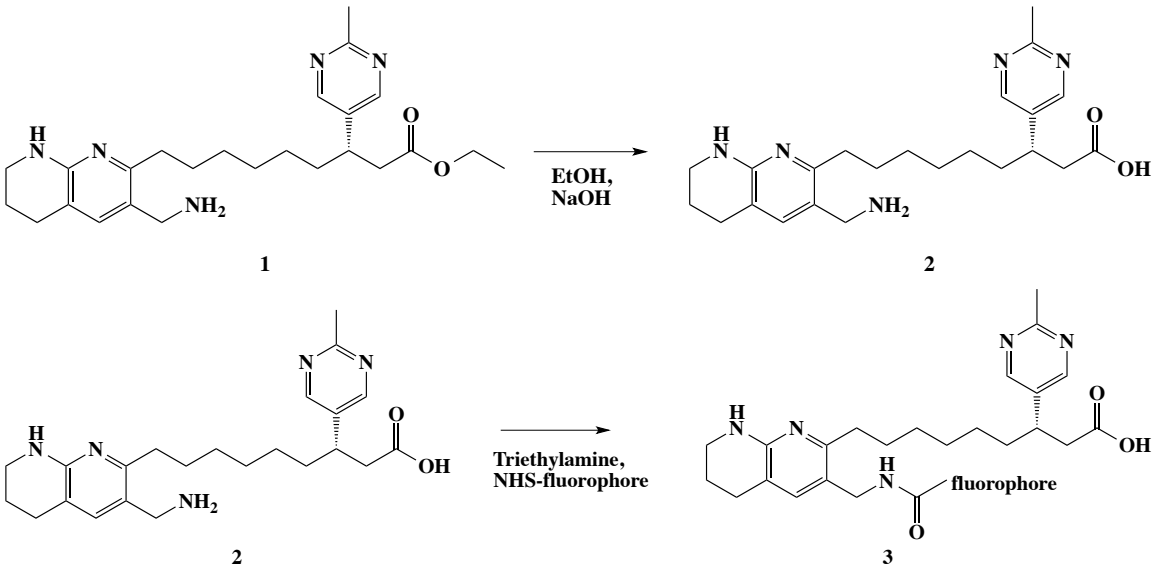

Figure 3.1 Reaction scheme for imaging agent synthesis

Imaging Agent Structures

Figure 3.2 shows the structures of all five imaging agents with a constant targeting ligand that binds primarily to integrin $\alpha_V\beta_3$ and varying NIR fluorophores to change the physico-chemical properties of the resulting imaging agents.

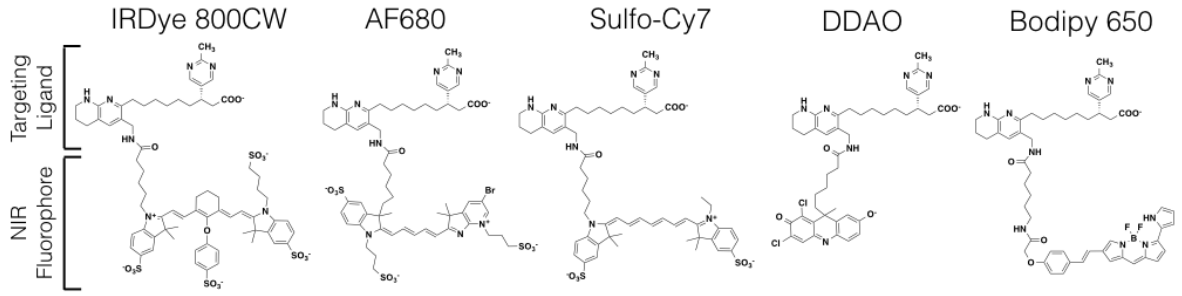

Figure 3.2 Structures of the imaging agents

Imaging Agent Properties

All five imaging agents were tested for properties like affinity, plasma protein binding and logD in *in vitro* assays. These properties along with the excitation and emission wavelengths of the imaging agents are shown in Table 3.3. The binding affinities range from single digit nanomolar to double-digit nanomolar. The agents had moderate to high plasma protein binding and a range from very hydrophilic (negative log D values) to lipophilic molecules (positive log D values). The excitation and emission wavelengths were either in the 600-700 nm or 750-800 nm range. The agents with wavelengths in the 750-800 range have much higher sensitivity due to the lower absorption and scattering of these wavelengths in human tissue.

Table 3.3 Physicochemical and optical properties of the imaging agents

	IRDye800CW	AF680	Sulfo-Cy7	DDAO	Bodipy650
Molecular Weight (Da)	1393	1249	1102	799	939
Formal Charge	-4	-3	-2	-2	0
PPB (%) ± S.D.	91 ± 2	78 ± 3	96.2 ± 0.7	96 ± 2	99.6 ± 0.4
Log D ± S.D.	-3.9 ± 0.5	-3.9 ± 0.5	-2.4 ± 0.2	1.1 ± 0.1	1.9 ± 0.1
Excitation/ Emission(nm)	774/789	679/702	750/773	648/656	646/660

The three main criteria used to determine whether or not the imaging agents would work well in this technique were high bioavailability, high specific targeting and ideal *in vivo* optical properties (Fig 3.3).

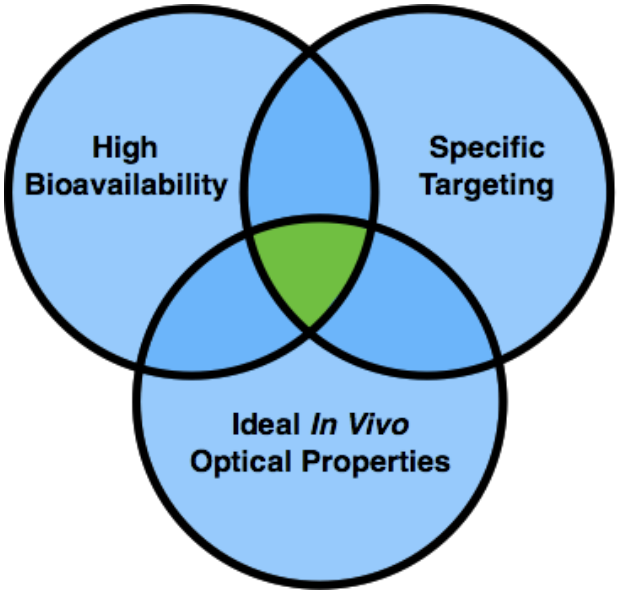

Figure 3.3 Venn diagram showing the three main design criteria for developing orally available imaging agents

In order to test the high specific targeting criteria, we imaged all the agents with cells with the antigen ($\alpha_V\beta_3$ +) and cells without the antigen ($\alpha_V\beta_3$ -). In this experiment, the cells without the antigen mimic healthy tissue, which has low to no expression of the antigen that is highly expressed on diseased cells, like in the case of cancer. Figure 3.4 shows that cells with the antigen have a significant amount of extracellular signal from the imaging agents whereas in the antigen negative cells the only imaging agent showing signal is the Bodipy650 agent. The bar graph highlights this data by introducing a blocked sample as well, where the antigen positive cells are blocked with a non-fluorescent integrin binder but still shows high signal from the Bodipy 650 agent. The BODIPY 650 agent has lipophilicity most similar to oral therapeutics such as cyclosporine A (logP = 2.92[166], F = 30%[167]), resulting in high non-specific sticking to

antigen-negative cells. The failure to meet the high specific targeting criteria led to the elimination of the Bodipy650 agent from being tested *in vivo*.

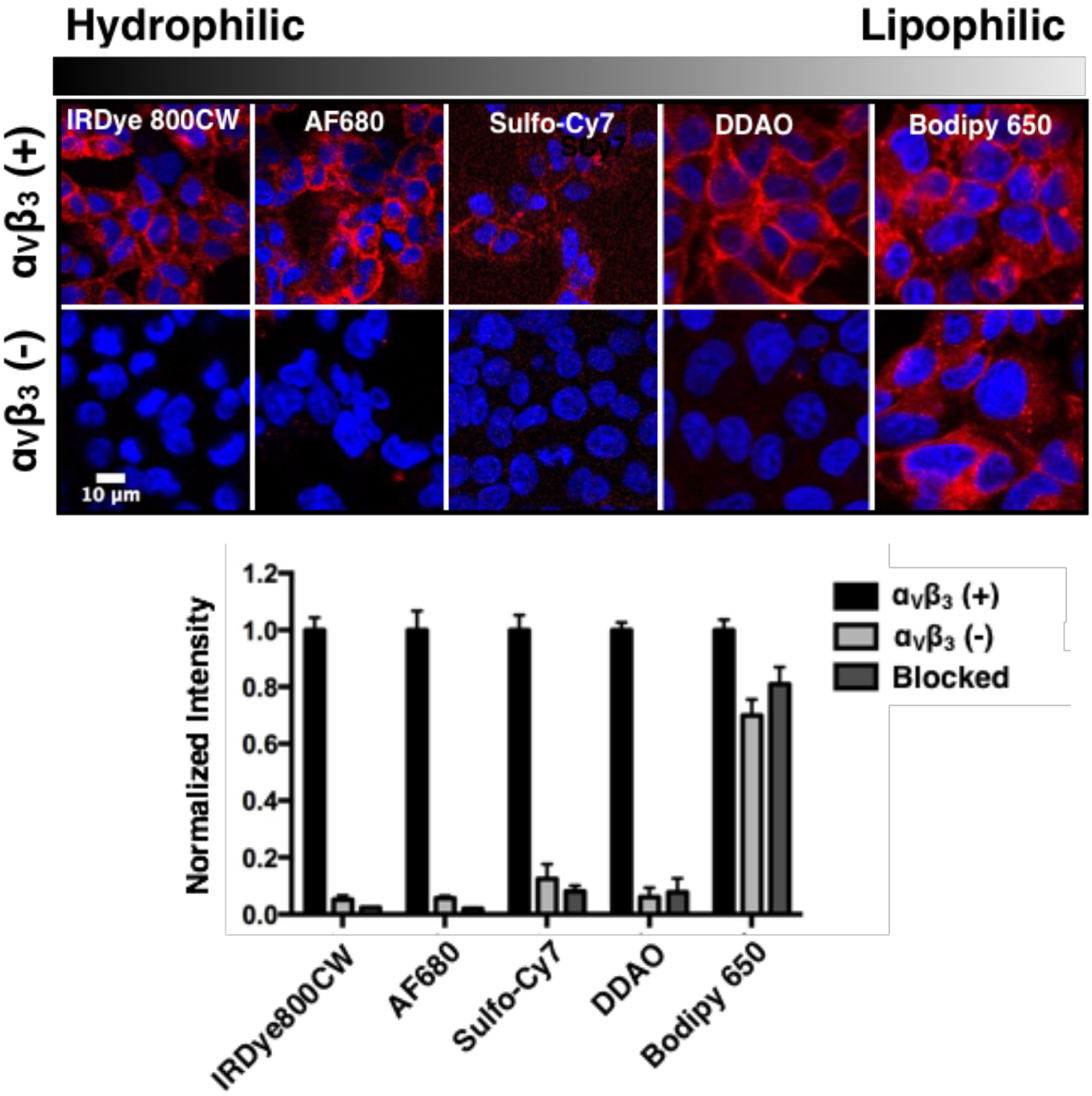

Figure 3.4 *In vitro* specificity of the imaging agents

HEK-293 cells with and without the antigen ($\alpha_V\beta_3$) showing extracellular labeling in the cells with the receptor. Cells without the receptor show sticking of the Bodipy650 agent. Quantitative data for non-specific interactions of the imaging agents using antigen negative ($\alpha_v\beta_3$(-)) and blocked controls normalized to the antigen positive cells ($\alpha_v\beta_3$(+)) show high non-specific signal from the Bodipy 650 agent.

The non-specific uptake rates of these imaging agents into antigen negative cells were measured to give an estimate of the signal expected from healthy tissues *in vivo*. This data was plotted against plasma protein binding which serves as a proxy for lipophilicity of a drug. The higher the plasma protein binding, the more lipophilic a drug is and the longer the uptake half life of the agent, the lower the signal would be obtained from healthy tissue. The linear relationship in the data can serve as a quick way to determine non-specific uptake by conducting an *in vitro* plasma protein binding assay without having to do any cell experiments. Fig. 3.5 shows this data without the DDAO agent. The reason for this was that while conducting the experiment we realized that the fluorescence of the agent decreases significantly when cells internalize the agent. On further investigation we found that hydoxy group on the fluorophore has a pKa of ~5 which causes the fluorescence to decrease when the in the acidic environment of endosomes and lysosomes. Since the DDAO agent loses fluorescence when internalized it did not meet the idea *in vivo* optical properties criteria, it was eliminated from being tested *in vivo.*

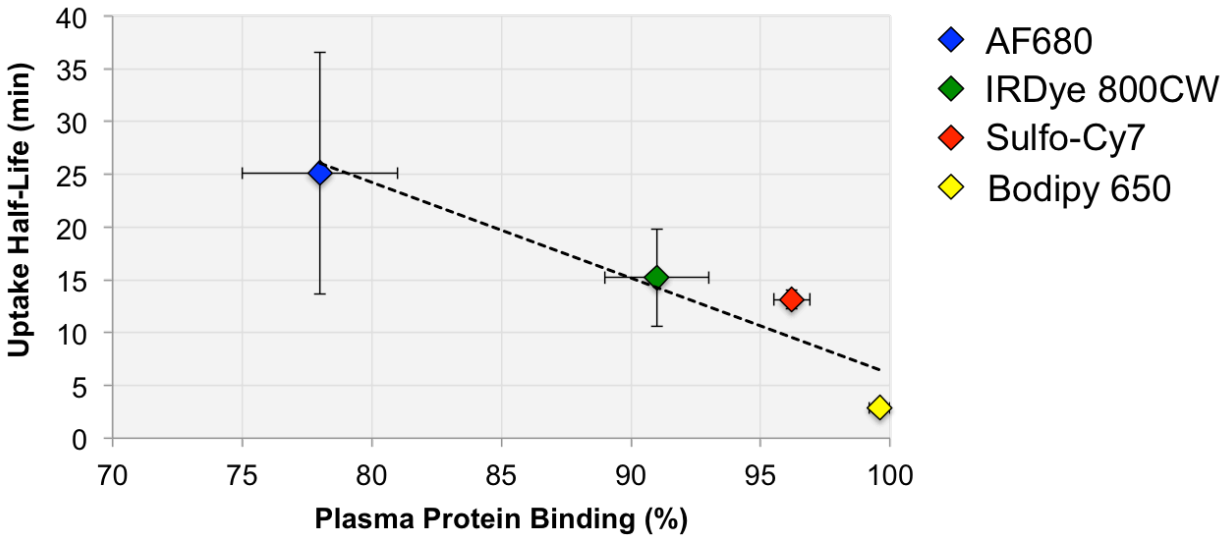

Figure 3.5 Linear trend between non-specific uptake and PPB (proxy for lipophilicity)

Based on the criteria shown in fig 3.3, the Bodipy650 and DDAO agents were eliminated from consideration. The remaining agents, IRDye800CW, AF680 and Sulfo-Cy7 were tested for

oral absorption in black-6 mice. The imaging agents were formulated in water and dosed at 1mg/kg. The mice were placed in a metabolic cage and their urine was collected for a period of 24 hours. The fraction of each imaging agent that was absorbed is shown in Fig 3.6. Overall, the oral absorption of these polyanionic conjugates was surprisingly high (Fig. 3.6) and since the IRDye800CW agent had the highest amount absorbed, it was selected for testing applications like breast cancer and rheumatoid arthritis detection.

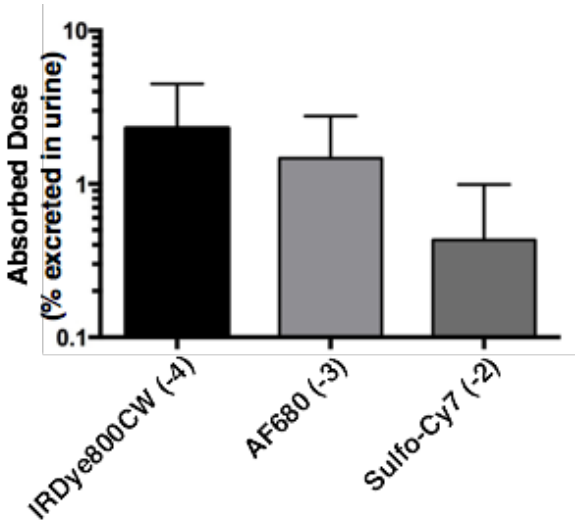

Figure 3.6 Orally absorbed dose (%)

3.5 Discussion

Development of a near-infrared orally available molecular imaging agent is inherently challenging, which is likely why, to the best of our knowledge, it has never been reported to date. There is an intrinsic dichotomy between physicochemical properties for high oral bioavailability and efficient targeting. Orally bioavailable agents are typically lipophilic with a low molecular weight to increase absorption. Efficient imaging agents are often hydrophilic with a higher molecular weight to reduce non-specific sticking/membrane partitioning and have a large binding surface for increased affinity and specificity. Additionally, the bright near-infrared

cyanine dyes towards the more ideal 800 nm region of the NIR spectra, due to lower absorption in human tissue, are higher in molecular weight.

To design agents with the highest likelihood of success, we used several target and ligand criteria (Fig. 3.2). These design parameters included selecting an extracellular target for easier access from the blood, high expression (> 10^5 receptors/cell), and preferably a significant internalization rate (<= 15 hr half-life). The target must have a known small-molecule binder (to bypass the *de novo* screening step) with high affinity (< 10 nM K_D), a low molecular weight (< 500 Da), few heteroatoms to increase the likelihood of intestinal absorption, and preferably a known site for fluorophore conjugation with a minimal impact on affinity. Ideally, the agent would be selected from a drug candidate that had preliminary oral bioavailability of the targeting ligand to avoid first-pass metabolism complications in the liver. While it is likely that not all of these criteria are necessary for all orally available probes, it gave the highest chance of success.

Several agents fit our design criteria, but we chose a small molecule integrin binding agent as the targeting ligand. Although monovalent cyclic RGD has proven to be a poor imaging agent due to its low affinity[168,169], higher affinity variants have demonstrated promising results[170-172]. Integrins, primarily $\alpha_v\beta_3$, are expressed in a variety of diseases including cancer (both tumor cells and activated endothelium) and on macrophages in other inflammatory diseases[173-175]. These integrins are expressed on the cell surface at high levels and are internalized within the target cell to residualize the agent[97]. Several integrin binders have made it to phase III clinical trials and are well tolerated at extremely high doses (grams per m^2 twice weekly for 16 week[176]). In fact, several have failed due to lack of efficacy[177]; a negligible pharmacological effect is actually ideal for an imaging agent (no on-target toxicity). The particular scaffold selected in this work had high bioavailability as a ligand (83% in dogs[178])

showing no signs of first-pass metabolism. The structure is a relatively simple peptidomimetic with available crystallography data[179]. A known modification site and series of fluorescent agents have been successfully developed for small animal imaging as the commercially available "Integrisense" series of imaging agents[97,180,181]. Given the unprecedented nature of the approach, this significant background data helped avoid several potential pitfalls for this proof-of-principle study.

Given the lack of precedent in the literature, we set out to generate a series of molecular imaging agents that varied in physicochemical properties to study the balance between oral bioavailability and targeting efficiency. Having decided on the target and ligand based on our earlier mentioned criteria, the ligand was reacted with five different NIR fluorophores such that we had a wide range of properties to identify the best suited for an orally available imaging agent. The IRDye800CW, AF680 and Sulfo-Cy7 agents, based on sulfated cyanine dyes, are hydrophilic in nature and have the highest affinities to the target, making them least likely to have off site interactions like sticking to healthy tissue. The DDAO agent has the smallest size and is lipophilic, increasing it chances of being orally absorbed. The Bodipy 650 agent has lipophilicity similar to a lot of commercially available therapeutics giving it the best chance of oral absorption, but also a high likelihood of having non-specific interactions.

High bioavailability, ideal *in vivo* optical properties and specific targeting (Fig 3.3) were used to evaluate the imaging agents. *In vitro* assays to measure the non-specific interactions of these agents showed the high amount of sticking of the Bodipy 650 agent to antigen negative cells, which did not meet the specific targeting criteria. Although the high lipophilicity of the agent makes it a great candidate to be highly orally absorbed, the same lipophilicity also causes it to non-specifically stick to antigen negative cells. Therefore, even if a significant fraction of the

dose is absorbed, this agent in unlikely to be able to provide good contrast between diseased and healthy tissues. The lack of specific targeting led to the elimination of the Bodipy 650 agent.

While measuring the rates at which all the agents are non-specifically taken up into antigen negative cells, we realized that the DDAO agent had poor optical properties. This was not evident from the fluorophore optical properties but while running experiments it became clear that when the agent was internalized into cells, the fluorescence of the agent dropped significantly. This is because one of the hydroxyl group on the fluorophore has a pKa of ~5, which impedes its ability to fluoresce brightly in acidic conditions. As agents are internalized into cells, they go from endosomes to lysosomes, both of which have an acidic environment hindering the DDAO agent's ability to fluoresce brightly. The ideal imaging agent for this technique needs to be internalized by cells for up to a few days, so that the agent from the rest body can clear and increase the contrast between the diseased and healthy tissue. Not meeting the ideal *in vivo* optical properties criteria led to the elimination of the DDAO agent.

The remaining three imaging agents were tested for bioavailability and they absorption was high considering the molecular weight of the agents (>1000 Da) and the high negative charge. Extensive research has been conducted into increasing the oral absorption of macromolecules. These investigations include polyanionic agents such as chondroitin sulfate[182], unfractionated heparins[183], anionic dendrimers[184-186], and anionic formulations to improve absorption of these and other compounds[187-192]. Fig. 3.7 shows the oral absorption of several hydrophilic molecules (clinical data unless otherwise stated) in comparison with the current agents[193-202]. The three agents reported here (black) are within the range of reported clinical and animal studies. Alendronate (-2 charge, 249 Da) has lower absorption. Fondaparinux is a charged

oligosaccharide with -10 charge and MW = 1728 and low absorption (light blue). When formulated to reduce pH and enzymatic degradation, much higher rates of absorption can be achieved (hatched light blue). Uncharged PEG (green) has lower absorption with larger molecular weight (3350 Da), similar absorption around the same size, and higher absorption with lower molecular weight. This is unexpected, since anionic charges typically reduce absorption. However, the anions may contribute to improved absorption (while still low compared to lipophilic small molecule drugs) since larger anions (chondroitin sulfate, a polydisperse anionic polymer, MW = ~21 kDa[203] and ardeparin, average MW = 6 kDa, range 2-15 kDa) have been reported with similar absorption (yellow). Some evidence suggests that these polyanionic molecules can modulate tight junctions to increase paracellular transport[191]. Polyanions, such as heparin, have also been shown to modulate tight junctions in other epithelial tissues such as the lung[204].

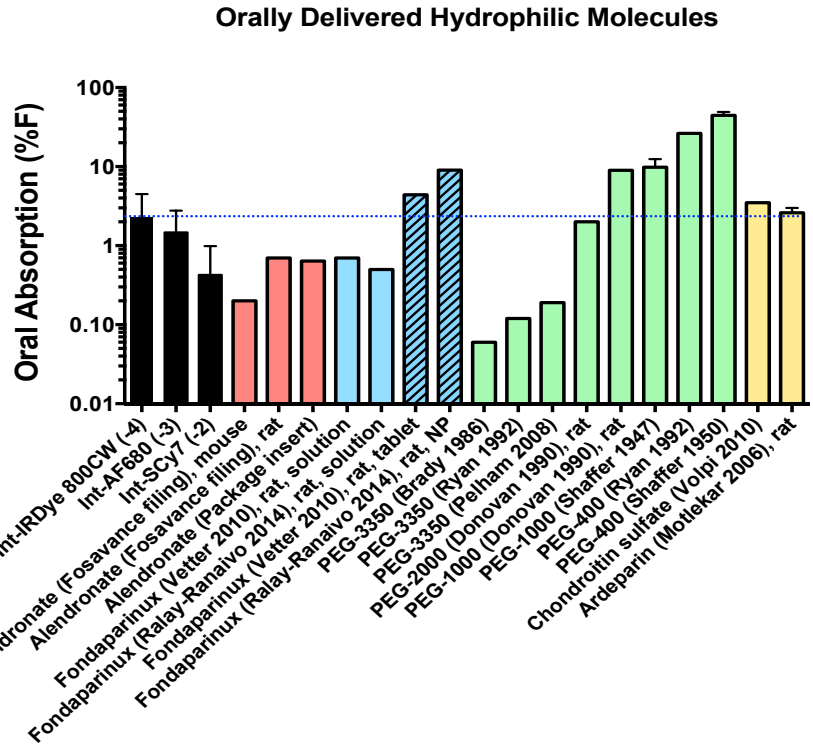

Figure 3.7 Oral absorption of anionic molecules

In addition to absorption, metabolism and/or excretion within the GI tract and liver (first-pass metabolism) can greatly impact systemic distribution following oral delivery. The low molecular weight heparin, fondaparinux is degraded within the GI tract, likely resulting in the higher absorption following formulation as a tablet or nanoparticle[193,194]. Similarly, charged dyes like ICG and some asymmetric cyanine dyes can undergo significant hepatobiliary excretion[205,206], making these agents unsuitable for oral delivery.

Lipophilic small molecule drugs can achieve very high oral absorption, and 30% is often a goal for pharmaceutical development[207]. Unlike biologics, which can be expensive to manufacture, the cost of small molecule drugs is typically low. The single dose (e.g. once a year for screening) compared to daily administration also results in insignificant materials costs, which can be compensated by the lack of sterile equipment and medical personnel costs for administering intravenous agents. However, variability in absorption is typically a larger issue. Because the background tissue autofluorescence is so low in the 800 nm region of the spectrum, the sensitivity is very high in this range, providing a low minimum amount of probe. Safety is a concern for maximum dose, but similar integrin targeting agents are well-tolerated at extremely high doses (*grams* per m^2 twice weekly for 16 weeks[176]). A more practical concern would be a lack of contrast due to high absorption and background signal. This occurs at super-saturating doses of the imaging agent, when high plasma concentration increases the background but can no longer increase the target signal due to receptor occupancy. For this target, the high expression on multiple cell types results in very high doses needed for saturation, yielding an excellent 'imaging window' analogous to a large 'therapeutic window' in drug development.

3.6 Conclusion

In conclusion, the large disparity in properties between orally available molecules and molecules that have high specificity towards their target, we synthesized a series of imaging agents with a wide range in properties. *In vitro* testing of these agents led to the selection of the three hydrophilic agents due to their high affinity to the target, lack of non-specific interactions and ideal *in vivo* optical properties. The oral absorption of these three agents was measured in mice, with IRDye800CW having the highest absorption. To maximize the likelihood of success, the IRDye800CW was selected for the detection of breast cancer and rheumatoid arthritis following oral delivery of the agent.

3.7 Experimental Methods

Imaging Agent Synthesis

The agents were generated similar to previous reports[163]. Briefly, the targeting ligand (ChemPartner, Waltham, MA) synthesized as an ester was re-suspended in DMSO at a concentration of 300 mg/ ml. The ester group on the integrin binder was hydrolyzed to a carboxylic acid by mixing it with 150 μL of ethanol and 7 μL of 1M NaOH per mg of drug with continuous stirring overnight. This mixture was then neutralized with 1M HCL and the solvents were evaporated. IRDye 800CW was obtained from LI-COR (Lincoln, NE)), Alexa Fluor 680, BODIPY 650/665-X and CellTrace Far Red DDAO were obtained from Life Technologies (Carlsbad, CA), and Sulfo-Cyanine7 was obtained from Lumiprobe (Hallandale Beach, FL) in the NHS ester form. The hydrolyzed integrin binder was reacted with the fluorescent dyes in a 2:1 molar ratio in the presence of 2 μL of triethylamine per mg of drug. The reaction was run overnight and purified using a preparative scale Luna C18(2) column (Phenomenex; Torrance,

CA) on a Shimadzu reverse phase HPLC. Full purification methods are provided in the supplementary data in Table S6. The purified products were run on a MALDI-TOF (High affinity IRDye800CW agent: m/z calculated 1397, found 1396; AF680 agent: m/z calculated 1253, found 1253; Sulfo-cyanine7 agent: m/z calculated 1103, found 1104; DDAO agent: m/z calculated 800, found 798; Bodipy 650 agent: m/z calculated 939, found 940; low affinity IRDye 800CW agent: m/z calculated 1397, found 1399). The purities of these agents (254 nm) were measured on HPLC (High affinity IRDye800CW agent: 95% (99.9% fluorescence purity); AF680 agent: 96.5%; Sulfo-cyanine7 agent: 88% (99.4% fluorescence purity); DDAO agent: 92%; Bodipy 650 agent: 87.5% (99.2% fluorescence purity); low affinity IRDye 800CW agent: 97.4% (99.9% fluorescence purity)).

Table 3.4 Purification methods and MALDI results

	Mobile Phase	HPLC Method	Retention Time	Expected MW	Observed MW
IRDy800CW	A: 25mM TEAA in water B: MeCN	25% B 0-6 min, 25-45% B 6-24 min	14 min	1397.682	1395.922
AF680	A: 0.1% TFA in water B: 0.1% TFA in MeCN	5-30% B 0-12 min, 30-60% B 12-16min	13.25 min	1253.351	1253.314
Sulfo-Cyanine7	A: 25mM TEAA in water B: MeCN	15-60% B 0-20 min	15 min	1103.405	1104.727
DDAO	A: 0.1% TFA in water B: 0.1% TFA in MeCN	20-95% B 0-15 min	9.75 min	800.8	796.8
Bodipy 650	A: 0.1% TFA in water B: 0.1% TFA in MeCN	20-95% B 0-15 min, 95% B Hold 15-16 min	11.5 min	938.9	940.1

Cell Lines

All reagents mentioned below were obtained from Life Technologies (Carlsbad, CA) unless specified otherwise. MDA-MB-231 and HEK-293 cells were purchased from ATCC (Manassas, VA) and grown in DMEM with 10% FBS and 1% Penicillin-Streptomycin (supplemented with 1% L-Glutamine for MDA-MB-231). HEK-293 cells, which express endogenous α_v but not β_3[208] were transfected with the β_3 integrin subunit (Addgene plasmid 27289) to generate an $\alpha_v\beta_3$ positive line. Cells were transfected with Lipofectamine 2000 according to the manufacturer's instructions and selected with 1 mg/mL G418 in the media.

Characterization (logD, PPB, affinity)

The binding affinity of all agents was measured using the transfected HEK-293 cells. The cells were harvested and incubated in triplicate with varying concentrations of the agents in suspension for 3 hours on ice. The cells were washed with PBS and run on an Attune acoustic focusing cytometer to quantify the fluorescence. Dissociation constants for each of the agents were determined by analyzing the data on Prism (GraphPad Software; La Jolla, CA). The large amount of non-specific signal generated from receptor-negative cells for the lipophilic BODIPY-650 agent was subtracted from the receptor positive cell line signal for an accurate measurement of the specific receptor dissociation constant.

Transfected and untransfected HEK-293 cells were plated on chamber slides and allowed to attach overnight. The cells were incubated with either 10 nM of the agent (IRDye 800CW and AlexaFluor 680) or 50nM (Bodipy 650/665-X, DDAO, and Sulfo-Cyanine7) for 25 minutes at 37 °C and washed with fresh media. The cells were then imaged on an Olympus FV1200 confocal microscope using the 405, 635, and 748 nm lasers.

Plasma protein binding (PPB) of the agents was measured using a Rapid Equilibrium Dialysis (Thermo Scientific; Rockford, IL) plate according to the manufacturer's instructions. Mouse plasma (Innovative Research; Novi, MI; Cat. No. C57BL6) was mixed with 1 μM of the agents. After equilibration, the buffer in each chamber was adjusted to 50% mouse plasma in PBS to eliminate effects of protein binding on fluorescence. The signal was measured using an Odyssey CLx (LI-COR; Lincoln, NE).

The $logD_{7.4}$ for all the agents was measured using a protocol adapted from Miller et al[209]. The agents were prepared at a concentration of 5-50 μM in octanol-saturated phosphate buffered saline (PBS, pH 7.4). 200 μL of this solution was mixed with 200 μL of PBS-saturated octanol. The mixture was stirred at 700 rpm for 24 hours. For lipophilic agents, the aqueous phase concentration was directly measured using fluorescence with the mass balance yielding the logD. Hydrophilic compounds with minimal loss in the aqueous phase were measured using a second extraction step. After the first equilibration, 150 μL of the octanol was mixed with 50 μL of fresh octanol-saturated PBS to extract the probe in the octanol phase and measure the aqueous fluorescence. During the fluorescence read-out, the samples and calibration curves were diluted in 0.5% PBS-BSA to minimize precipitation and sticking to the vessel surface.

In Vivo Oral Absorption

Eight week old C57BL/6 female mice (n = 3-4 per cohort) were used to measure the oral absorption of the imaging agents. All experiments involving mice were conducted in compliance with the University of Michigan University Institutional Animal Care and Use Committee (IACUC). The mice were fasted for 4-6 hours and then dosed with 1 mg/kg of the imaging agent via oral gavage and placed in a metabolic cage for a period of 24 hours. Urine was collected

from these cages at the end of 24 hours. The urine was diluted 10 fold in 0.1% PBS-BSA to prevent the agent from sticking to vessel surfaces. This was then measured on an Odyssey CLx to determine the amount of fluorescent agent present in the urine. This was quantified using a calibration curve of each agent.

Chapter 4: Breast Cancer Screening in an Orthotopic Mouse Model with an Orally Available Near Infrared Molecular Imaging Agent

4.1 Publication Information

Bhatnagar S, Verma KD, Hu Y, Khera E, Priluck A, Smith DE, Thurber GM 2018. Oral Administration and Detection of a Near-Infrared Molecular Imaging Agent in an Orthotopic Mouse Model for Breast Cancer Screening. Molecular pharmaceutics 15(5):1746-1754.

Modifications have been made to the published document to adapt the content to this dissertation.

4.2 Abstract

Molecular imaging is ideal for disease screening by providing precise spatial information of disease-associated biomarkers, something neither blood tests nor anatomical imaging can achieve. However, high costs and risks of ionizing radiation for several molecular imaging modalities have so far prevented a feasible and scalable approach for screening[109]. Clinical studies have demonstrated the ability to detect breast tumors using non-specific probes such as indocyanine green[151,210], but the lack of molecular information and required intravenous contrast agent does not provide a significant benefit over current non-invasive imaging techniques. Here we demonstrate that negatively charged sulfate groups, commonly used to improve solubility of

near-infrared fluorophores, enable sufficient oral absorption and targeting of fluorescent molecular imaging agents for completely non-invasive detection of diseased tissue such as breast cancer. These functional groups improve the pharmacokinetic properties of affinity ligands to achieve targeting efficiencies compatible with clinical imaging devices using safe, non-ionizing radiation (near infrared light). Together, this enables the development of a 'disease screening pill' capable of systemic absorption, target binding, background clearance, and imaging at clinically relevant depths for breast cancer screening. This approach should be adaptable to other diseases and molecular targets for use as a new class of disease screening agents.

4.3 Background

Molecular imaging has the potential to provide significant improvement in breast cancer screening. While therapy has been rapidly advancing towards molecular characterization, screening relies on anatomical differences that have several limitations[109]. These include the lack of molecular information to identify aggressive tumors versus those that pose no mortality risk (over-diagnosed tumors)[211,212] and the lack of contrast in dense breast tissue that carries increased risk, particularly prevalent in younger women[213,214]. These limitations have led to an estimated $4 billion being overspent on false-positives and overdiagnosis[215]. The shortcomings in sensitivity and specificity of anatomical imaging have motivated research in new imaging and systemic detection modalities[106,216], including near-infrared imaging[217,218]. Current scanners are capable of imaging tumors less than 2 cm in diameter that are imbedded deep in breast tissue at the contrast levels we report here[219,220], and further improvements in complementary technologies, such as photoacoustic imaging, are likely to push the detection limits even smaller[221].

Many integrin-targeted imaging agents are currently being investigated in clinical trials (e.g. 8 RGD-based probes reviewed recently[222]). The high level of expression on multiple distinct cell types, including stromal tissue, is advantageous for early screening because of an anticipated robust detection sensitivity (e.g. all tumors will require neovasculature beyond a certain size, immune cell infiltration is associated with greater risk of recurrence even with small lesions like DCIS[223]). The typically high level of expression on these cells types also increases the dose-window for imaging by lowering the chances of receptor saturation (which would reduce contrast).

Table 4.1 Integrin expression levels on various cell types

	Expression level (receptors/cell)	Refs
Activated endothelium	$1.7x10^5$	[224]
Macrophages	$2x10^5$	[225]
Tumor cells	$\sim 5\text{-}10x10^4$	[226,227]

In addition to detection sensitivity, the tumor expression of $\alpha_V\beta_3$ integrin is associated with more aggressive tumors due to increased angiogenesis and more aggressive forms of DCIS[228]. This is particularly poignant as analyses of large data sets indicate that the current use of mammography is over-diagnosing and treating women[229,230]. The over-diagnosis of women with breast lesions is particularly problematic with some estimates indicating a cost of $4 billion per year[215]. The rate of overdiagnosis can be reduced with the right selection criteria, such as high grade DCIS in younger women[231]. Molecular imaging agents have the potential to better differentiate aggressive lesions versus benign conditions, and these promise will have to be tested in the clinic. For example, microvessel density (endothelial targeted cells) is higher in DCIS with a high proliferative index, HER2 expression, and Comedo-type lesions[228]. There is very low macrophage infiltration (macrophage-targeted cells) in normal breast and benign

proliferative disease but this is elevated in DCIS and even higher with invasive carcinoma[232]. The presence of these markers early in breast cancer development is critical for detecting early stage cancers and high-risk DCIS, which is ideal for initial screening purposes.

A significant benefit from using molecular imaging agents is expected to be the ability to detect aggressive breast cancers in younger women and/or women with dense breast tissue. Women with dense breast tissue have a markedly increased risk for invasive breast cancer[233] and have a higher risk of dying from their cancer (e.g. following DCIS[234]). Because the detection is based on fluorescence from a molecularly targeted agent (and not tissue density differences), the sensitivity and specificity is not expected to be highly dependent on breast tissue density. Note that for non-specific NIR probes, differences in uptake have been noted from tissue differences alone, motivating a targeted probe approach[150]. Additionally, the propagation of NIR is similar between breast tissue types[235] This benefit has been demonstrated with radiolabeled integrin targeting agents in the clinic, where sensitivity to lesions was higher in women with dense breast tissue[236]. The utility of the approach will need to be verified in clinical trials, but it may find a role in screening younger women who do not benefit from mammography and/or used in conjunction with mammography where sensitivity and specificity can be greatly improved with dual modalities[236].

As mentioned in Chapter 3, the route of administration of a molecular imaging agent for screening purposes is critical for a feasible and scalable approach, where the target rates for mammography are already difficult to achieve[237]. Oral delivery is safer, less expensive and likely to have a higher compliance compared to other routes of delivery. Therefore, in this study we orally deliver an integrin binding agent in orthotopic breast cancer mouse models to show the applicability of the technique in the detection of breast cancer.

4.4 Results

High uptake and specificity of imaging agent in breast cancer

Using an orthotopic xenograft model of breast cancer (MDA-MB-231 cells injected in the mammary fat pad), mice were dosed with 5 mg/kg of the IRDye800CW by oral gavage and imaged at 6, 24, and 48 hours post injection (Fig. 4.1). The tumors had significant uptake by 6 hours, and the intestinal signal cleared at the later time points to yield high contrast by 24 and 48 hours (tumor to background ratios of ~4 at 48 hours).

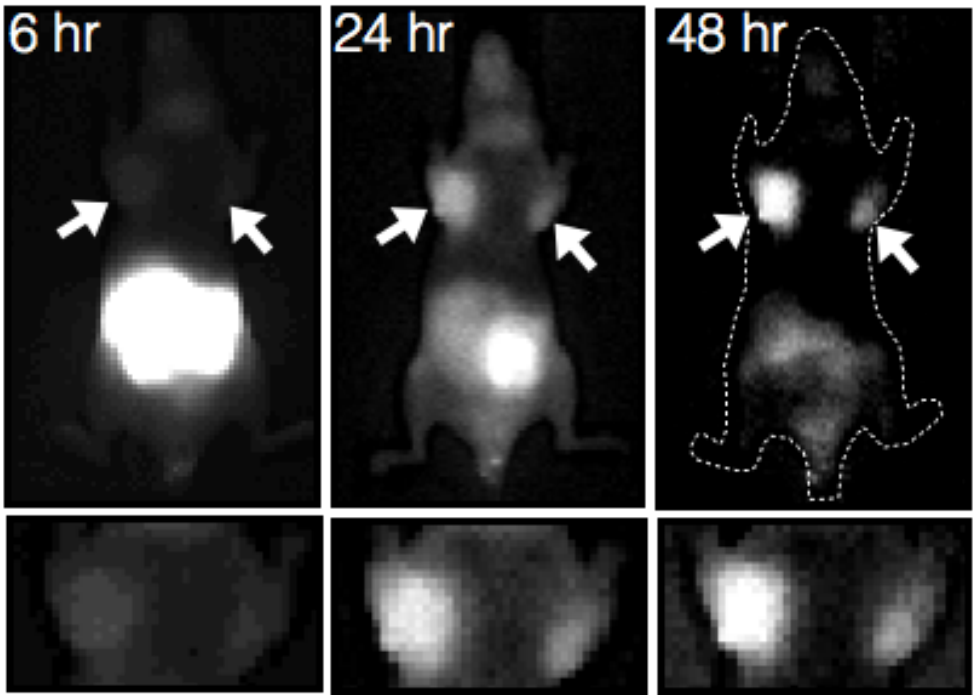

	6 hours	24 hours	48 hours
Measured Intensity ($\times 10^8$)	1.5 ± 0.3	1.6 ± 0.3	1.3 ± 0.3
TBR	1.7 ± 0.1	2.8 ± 0.2	3.9 ± 0.7

Figure 4.1 Whole animal fluorescent images, intensity and TBR for the IRDye800CW agent

The image intensity shows that the amount of the probe in the tumor stays relatively constant over a period of 48 hours owing to the residualizing nature of the NIR fluorophore[238]. To demonstrate specificity, we used a low-affinity stereosiomer since the two most common

techniques, blocking specific uptake or using an antigen negative tumor, were not feasible. The structures for both the agents are shown in figure 4.2.

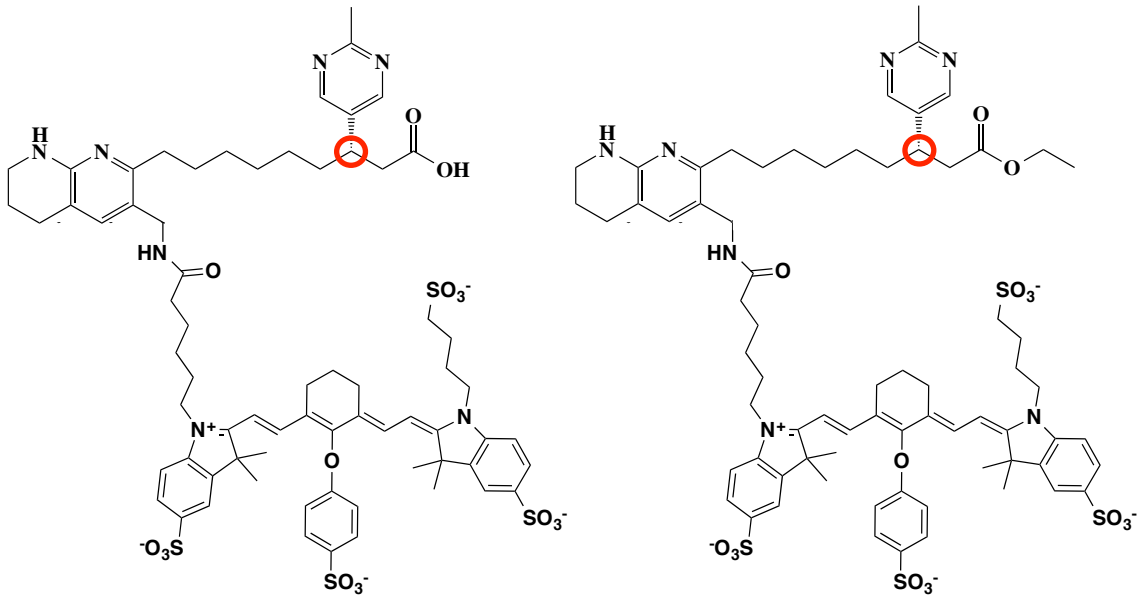

IRDye800CW Agent IRDye800CW Agent Stereoisomer

Figure 4.2 Structure for the IRDye800CW agent and its stereoisomer with the chiral carbon highlighted in the red circle.

The IRDye800CW agent stereoisomer has an affinity to integrin, which is an order of magnitude worse than the affinity of the IRDye800CW agent. The lower affinity would theoretically lead to lower uptake in the tumors, which is exactly what Fig. 4.3 shows indicating that the IRDye800CW agent is taken up through specific interactions with the integrin receptor. This is important as we are trying to obtain molecular information about the tumor. The whole animal fluorescence intensity and biodistribution showed dramatically lower uptake for the stereoisomer. Biodistribution data at 48 hours (Fig. 4.4) correlated well with the whole animal images (Fig. 4.1 and 4.3) showing that the amount of agent in the tumor was significantly higher in the tumor for the IRDye800CW agent compared to the stereoisomer.

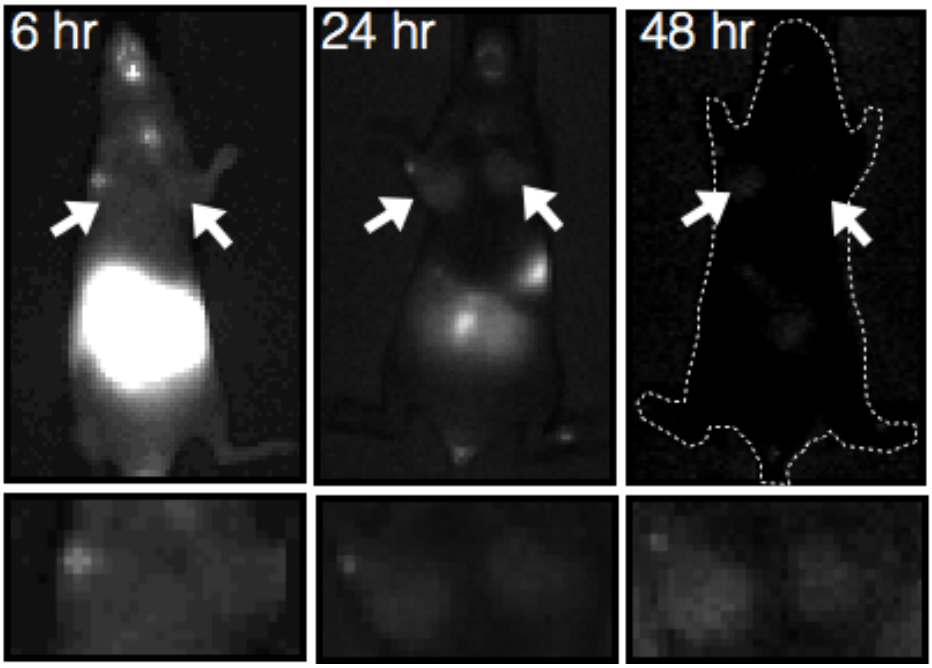

	6 hours	24 hours	48 hours
Measured Intensity ($\times 10^8$)	0.78 ± 0.08	0.3 ± 0.1	0.22 ± 0.7
TBR	1.1 ± 0.4	1.8 ± 0.2	1.8 ± 0.2

Figure 4.3 Whole animal fluorescent images, intensity and TBR for the IRDye800CW agent stereoisomer

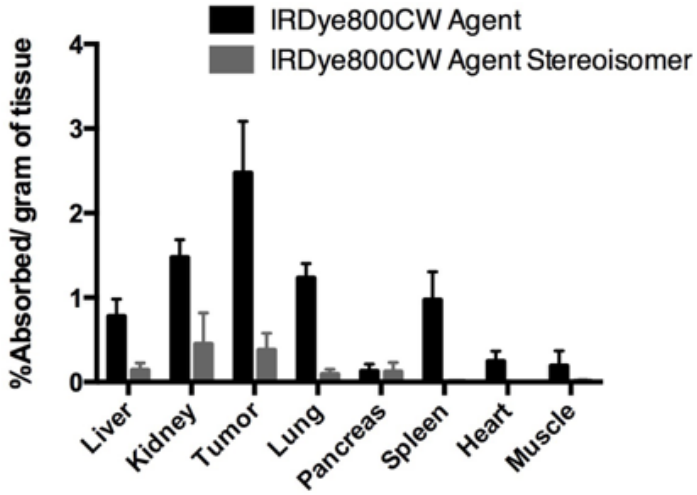

Figure 4.4 Biodistribution data of the IRdye800CW agent and stereoisomer at 48 hours

The IRDye800CW agent panel in Fig 4.4 shows signal from the orally delivered agent, Mac3 panel labels the macrophages in the tissue slice, the CD31 labels all blood vessels, integrin labels all available $\alpha_V\beta_3$, and Hoechst labels the nuclei of all cells. The IRDye800CW agent image is blurry as it was taken at a different resolution that the other images. The signal from the agent was diffuse throughout tissue requiring a macroscopic image of the tissue. All the other labels were *ex vivo* to identify the different cell types in the slice. Integrins are expressed at high levels on breast cancer cells, tumor associated macrophages, and neovasculature, providing robust detection by diversifying the cellular targets. The rapid tumor penetration of this low molecular weight compound and intermixed cell types in this model[47] resulted in relatively uniform signal throughout the tumor with potentially higher uptake by tumor associated macrophages shown by the overlap of the first two panels (Fig. 4.5).

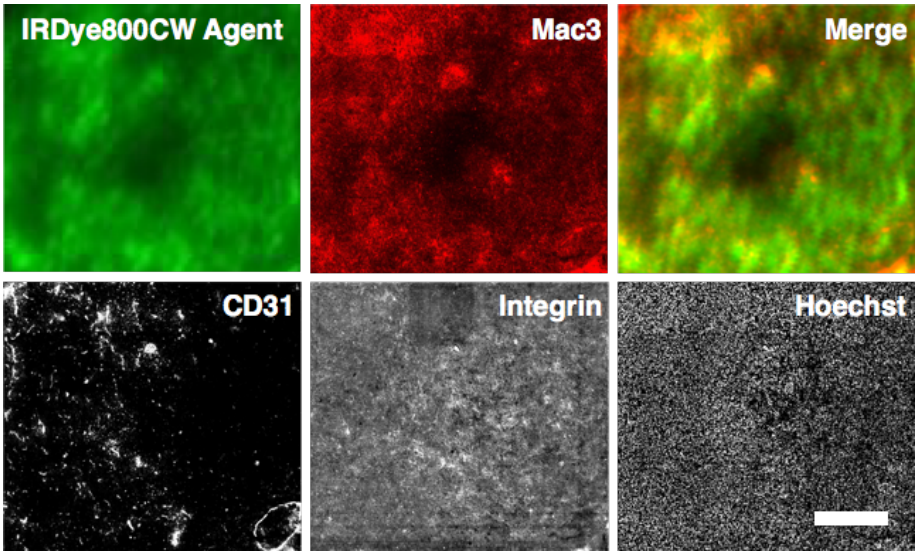

Figure 4.5 Histology of tumor tissue with the IRDye800CW agent and other ex vivo stains

Macroscopic images of tumor histology slide taken on an Odyssey CLx (IRDye800CWagent) and Olympus FV1200 confocal microscope (other channels). The orally delivered agent shows a diffuse pattern in tumors compared to the negative control (not shown). The intensity appears to be slightly higher in regions with higher macrophage density versus tumor cells or blood vessels (CD31). The slides were labeled with the AF680 agent ex vivo (integrin) and stained with

Hoechst 33342 to show the presence of cells and integrin throughout the tissue. Scale Bar = 500 μm**.**

4.5 Discussion

Oral delivery and non-invasive detection of near-infrared fluorescent molecular imaging agents has significant advantages over other screening modalities including low cost, increased safety, portability, and non-invasive molecular imaging results. They also have the promise to provide spatial and molecular information to a physician using a method less invasive than a blood test. Particular advantages over intravenous delivery of these agents include a lower risk of anaphylaxis due to oral, which is an important consideration for screening a healthy population, needle-free and pain-free self-administration for improved patient compliance, and the potential application in resource-limited settings without the need for medical facilities and sterile reagents

The IRDye800CW agent gave excellent contrast in the orthotopic breast cancer model. To better understand the temporal imaging window, mice were imaged at 6, 24 and 48 hours after oral gavage. Similar to intravenously delivered agents, the signal intensity was highest at earlier times, but the TBR increased at longer times (Fig. 4.1). Forty-eight hours yielded TBR values averaging 4 (n=3 mice). Mice were sacrificed at this time to measure the biodistribution with 2.5% orally absorbed dose per gram remaining in the tumor two days after oral gavage. The optimal imaging time, days after delivery, exemplifies one of the strengths of this approach. Oral delivery, in contrast to intravenous injection, does not require multiple visits for agent delivery and a return visit for imaging.

One of the main goals of this technique is to provide molecular information about the tumor along with detection, which is something that mammography cannot provide. Thus, to make sure that we are obtaining molecular information we need to make sure that the imaging

agent is being taken up specifically in the tumor through interaction with the $\alpha_V\beta_3$ receptor. In order to test this specific uptake in the tumor, a stereoisomer of the ligand was conjugated with IRDye800CW to create a low affinity imaging agent. The affinity of the IRDye800CW agent is 5.1nM for $\alpha_V\beta_3$ while it is 40nM for the stereoisomer. This allowed us to use the stereoisomer as a negative control, while still maintaining all the properties of the imaging agent other than affinity. Traditional negative controls like blocking or antigen negative controls were not feasible for these *in vivo* experiments. Since the imaging agent is orally absorbed over the period of several hours (Fig 4.6), it would require an impractical amount of non-fluorescent ligand to completely block all the integrins within the tumor. Antigen negative controls would not work either since $\alpha_V\beta_3$ is expressed on activated macrophages and neovasculature, which are present in almost all tumor types. The controls showed that the stereoisomer was taken up significantly lower in the tumor and other organs (Fig. 4.4) in spite of having similar oral absorption (Fig. 4.6). Healthy tissue expresses $\alpha_V\beta_3$ at low levels explaining the low uptake in healthy tissues. This control clearly shows that the imaging agent is being taken up in the tumor specifically and the lack of the control uptake was due to its lower affinity towards the target.

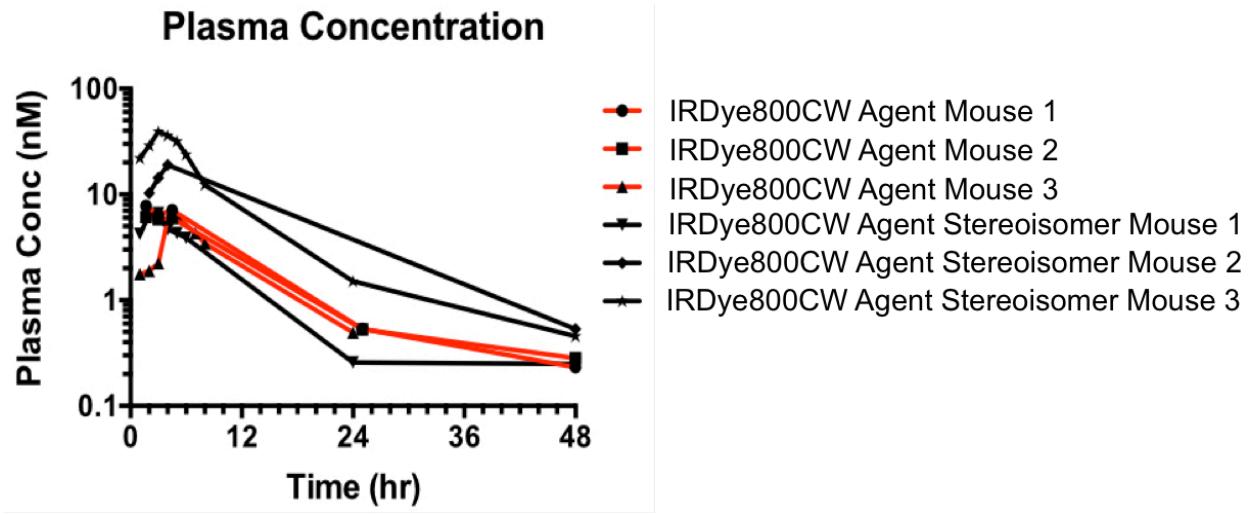

Figure 4.6 Plasma clearance following oral administration

Mammography is the current gold-standard for breast cancer screening[239] but the large number of false positives and negatives[215,240,241] could be improved through more specific and sensitive imaging, particularly for younger women with denser tissue[242]. Extensive work on NIR optical tomography[128] and fluorescence imaging[151] has demonstrated excellent tissue penetration of NIR light in breast tissue[243]. $\alpha_v\beta_3$ is upregulated on both activated endothelium and breast cancer cells[244] and expression correlates with a more aggressive phenotype and bone metastasis[245,246]. Ultimately, this technique may pair well with clinically used ultrasound of the breast[247]. Analogous to PET-CT, NIR fluorescence would provide molecular information and ultrasound would generate anatomical reference in an inexpensive, hand-held format[248,249] for enhancing the selectivity and specificity of breast cancer detection.

Many integrin-targeted imaging agents are currently being investigated in clinical trials (e.g. 8 RGD-based probes reviewed recently[222]). The high level of expression on multiple distinct cell types, including stromal tissue, is advantageous for early screening because of an anticipated more robust detection sensitivity (e.g. all tumors will require neovasculature beyond a certain size, immune cell infiltration is associated with greater risk of recurrence even with small lesions like DCIS[223]). The typically high level of expression on these cells types also increases the dose-window for imaging by lowering the chances of receptor saturation (which would reduce contrast).

In addition to detection sensitivity, the tumor expression of $\alpha_V\beta_3$ integrin is associated with more aggressive tumors due to increased angiogenesis and more aggressive forms of DCIS[228]. This is particularly poignant as analyses of large data sets indicate that the current use of mammography is over-diagnosing and treating women[229,230]. Molecular imaging agents have the potential to better differentiate aggressive lesions versus benign conditions, and reduce the

rate of overdiagnosis through better detection of at-risk tumors, such as high grade DCIS in younger women[231]. For example, microvessel density (endothelial targeted cells) is higher in DCIS with a high proliferative index, HER2 expression, and Comedo-type lesions[228]. There is very low macrophage infiltration (macrophage-targeted cells) in normal breast and benign proliferative disease but this is elevated in DCIS and even higher with invasive carcinoma[232]. The presence of these markers early in breast cancer development is critical for detecting early stage cancers and high-risk DCIS, which is ideal for initial screening purposes.

Several clinical studies have demonstrated the feasibility of imaging breast tumors deep within breast tissue. These studies have primarily used indocyanine green (ICG), which is a non-targeted contrast agent that is approved by the FDA.

Table 4.2 Clinical breast cancer imaging studies

	Tumor size	Contrast	Ref
ICG	~1 cm	(absorption)	[218]
ICG	1.5, 1.6, and 2.5 cm	3.5 to 5.5	[210]
ICG	1.6 and 1.1 cm	1.5 to 1.8	[250]
Omocyanine	2.9, 1.8, 2.4, 7.4, 3.4 cm	1.8 to 2.8	[150]
ICG	2.5 cm (mean), range 1.1 to 5.2 cm	0.25 to 0.64	[151]

Probing breast tissue using light (diaphanography) dates back to the 1920's but made substantial advances in the late 1990's and early 2000's due to improvements in imaging equipment and tomographic techniques[251]. Corlu et al. was the first to publish fluorescence imaging of human breast tumors using ICG. The fluorescence imaging gave the best contrast, and other studies have indicated that fluorescence is better than absorption with low background concentrations[220]. Despite the promising results found in several trials, untargeted contrast agents do not perform better than mammography alone[252], and there is a strong need for targeted contrast agents[150].

Many additional studies have tested the limits of detection both theoretically and with optical phantoms. Tumors less than 2 cm[219] can be detected in the contrast ranges achieved here in mice, and the absolute concentrations of IRDye800CW are much higher than those detected using a clinical breast imaging system[253], indicating the contrast achieved with these orally delivered agents is suitable for clinical detection using diffuse optical tomography, as used in the studies with Omocyanine from Table 4.2.

A significant benefit from molecular imaging is the ability to detect aggressive breast cancers in younger women and/or women with dense breast tissue. Women with dense breast tissue have a markedly increased risk for invasive breast cancer[233] and have a higher risk of dying from their cancer (e.g. following DCIS[234]). Because the detection is based on fluorescence from a molecularly targeted probe (and not tissue density differences), the sensitivity and specificity is not expected to be highly dependent on breast tissue density[235]. (Note that for non-specific NIR probes, differences in uptake have been noted from tissue differences alone, motivating a targeted probe approach[150].) This benefit has been demonstrated with radiolabeled integrin targeting agents in the clinic, where sensitivity to lesions was higher in women with dense breast tissue[236]. The utility of the approach will need to be verified in clinical trials, but it may find a role in screening younger women who do not benefit from mammography and/or used in conjunction with mammography where sensitivity and specificity can be greatly improved with dual modalities[236].

Results from this study demonstrate that molecules can overcome the significant physical and kinetic barriers for sufficient oral delivery and targeting of molecular imaging agents. Hydrophilic molecules, particularly anionic drugs, have low oral bioavailability and high patient-to-patient variability in absorption. Rapid hepatic clearance of near-infrared dyes like

indocyanine green could further lower systemic absorption through first-pass extraction[205]. However, several polyanionic molecules have shown measurable absorption following oral delivery[183,254]. Oral heparin, another sulfonated macromolecule, is susceptible to stomach acid degradation, but with proper formulation, absorption in animal models ranges from 3% to 38%[193,194,255,256]. A Phase III clinical trial demonstrated effective absorption [255]. Similarly, negatively charged chondroitin sulfate has measurable absorption in humans[201], as does polyanionic dendrimers in animal models[186].

Unlike therapeutics that often have a narrow window between toxicity and efficacy (and higher material cost for continual daily administration), the absorption of imaging agents is more tolerable to patient-to-patient variability. The upper limit here is target saturation (where higher doses would lower contrast) since even gram doses of anti-integrins are well-tolerated[176], and the lower bound is image noise from autofluorescence. The optimal 800 nm imaging channel and high target expression provide a large window for achieving efficient contrast.

Besides total absorption, there are significant hurdles in targeting due to the slower absorption rate following oral delivery compared to intravenous delivery. A dissociation rate of days at 37°C would be required to maintain significant signal until the probe is fully absorbed and cleared from background tissue. However, by selecting internalizing targets, the anionic charge can aid in trapping the dye within cells for days[238]. Despite the long time period between delivery and imaging, this is still favorable from a patient compliance standpoint, since intravenous delivery of low molecular weight agents requires a minimum of hours to develop contrast. This would necessitate extended or multiple clinical visits – the first to receive an intravenous dose and monitoring for adverse reactions followed by an imaging visit several hours to days later. While this may not be an impediment for life-saving surgery with

intraoperative imaging[139], it could have a major impact on patient compliance in screening large healthy populations. Because material costs for small molecules are often low (e.g. $1 per dose for small molecule drugs[147]), the associated costs of medical personnel and sterile intravenous delivery would likely be higher than any cost savings from improved bioavailability from more invasive routes.

In the current approach, contrary to radiolabeled probes[163], some plasma protein binding is beneficial by slowing clearance relative to absorption, increasing the plasma concentration, and improving target signal relative to background autofluorescence (Fig. 4.6). Therefore, the plasma protein binding mediated by the high anionic charge also plays a role in enabling orally delivered molecular imaging agents.

There are several current limitations and areas for improvement with this approach. First, the 2.5% absorbed dose results in variability between mice. While this variability does not impact the contrast significantly since both tumor signal and background are approximately linear with absorbed dose, mice at the very low end of the absorption profile risk having autofluorescence lower the contrast to noise ratio. Improved formulation could increase the absorption and lower the variability, thereby reducing the dose needed. Second, clinical trials with intravenously delivered non-specific contrast agents have highlighted the difficulty in imaging tumors in the breast near the chest wall, similar to mammography. Improvements in alternative detection methods, such as optoacoustic imaging, may provide better detection in this region. Finally, although the current probe provides molecular information, which is an improvement over anatomical images, a single biomarker will not be able to differentiate all tumor types. Additional biomarkers, e.g. from dual-channel imaging at a second NIR wavelength with a different probe, could significantly increase the diagnostic specificity. The use of

negatively charged probes should be adaptable to other small molecule targeting ligands against different surface markers.

4.6 Conclusion

In conclusion, the high negative charge density on the IRDye800CW agent enabled sufficient absorption, reduced non-specific uptake, facilitated targeting by extending the clearance half-life, and increased retention through cellular trapping to yield efficient targeting contrast in a small animal model of breast cancer for detection at clinically relevant depths. It was able to provide a TBR of 4 at 48 hours post administration of the imaging agent in comparison with the stereoisomer, which only had a TBR of 1.8, highlighting the efficient uptake through specific interactions with the $\alpha_V\beta_3$ receptor. To our knowledge, this is the first demonstration of a disease screening approach using oral administration of a molecular imaging agent, and these mechanisms should be applicable to additional probes and disease targets for developing a series of molecular imaging agents for non-invasive screening.

4.7 Experimental Methods

In Vivo Imaging

MDA MB 231 cells were used for tumor xenografts in nude mice (Jackson Laboratory; Bar Harbor, ME). The cells were harvested using Trypsin-EDTA (0.05%), re-suspended in Matrigel (Corning; Corning, NY) at a concentration of 5 million cells/50 μL. Mice were anesthetized using isoflurane at 2% and 1 L/min oxygen and the cells were injected subcutaneously by the first nipple in the mammary fat pad to avoid fluorescence signal from the gut when imaging. The tumors were imaged once the longest axis of the tumor reached 7-10 mm.

Tumor-bearing mice were anesthetized and imaged in an IVIS Spectrum (Perkin Elmer; Waltham, MA) at 6, 24 and 48 hours post injection.

Tumor-bearing mice were fed AIN-93M non-fluorescent chow (Harlan; Indianapolis, IN; Cat. No. TD.94048) for 2 weeks before oral gavage and were fasted for 4-6 hours pre-oral administration. Mice (n = 3 per cohort) were imaged on an IVIS Spectrum (Perkin Elmer; Waltham, MA) at 6, 24, and 48 hours after administration of the agent, and the LivingImage software (Perkin Elmer; Waltham,MA) was used to measure the signal intensity in the tumor and TBR. The biodistribution protocol is adapted from Oliviera et al[257]. In short, the mice were euthanized at 48 hours post administration and all their organs were resected. The organs (part of the tumor was frozen in OCT for histology slides) were minced with a razor blade and weighed. They were placed in Eppendorf tubes and digested using a collagenase (Worthington Biochemical; Lakewood, NJ; Cat. No. CLS-4) solution (5 mg/ ml) in RIPA buffer (Boston BioProducts; Ashland, MA) at 37°C for 20 minutes. The organs were sonicated, digested for 30 minutes at 37°C using a 50:50 trypsin and RIPA buffer solution and sonicated again. The resulting mixture was plated in a dilution series in a black walled 96-well plate and imaged using the Odyssey CLx. Absolute quantification was obtained by comparison with a calibration curve. The uptake values were normalized to the average amount of probe that reached the systemic circulation (absorbed dose) per gram of tissue (versus injected dose per gram (%ID/g) used for intraveneous delivery).

Histology

Frozen blocks of the tumor in OCT were sectioned into 14 uM slices on a cryostat. The slices were first imaged on the Odyssey CLx in the presence of PBS to prevent the tissue from drying out. This slice was then stained ex-vivo with Hoechst 33342 (Thermo Fisher Scientific;

Cat. No.H3570), the AF680 conjugated probe (due to its higher affinity), Cetuximab (Bristol-Myers Squibb, Princeton, New Jersey) labeled AF750, anti-Mac3 antibody (BD Biosciences, San Jose, CA: Cat. No. 553322) labeled AF555 and anti-CD31 (BioLegends, San Diego, CA; Cat. No. 102402) labeled AF488. These slides were then washed in PBS and imaged on an Olympus FV1200 confocal microscope equipped with 405, 488,543, 633 and 748 nm laser lines.

The integrin image in Fig. 4 was post processed to remove stitching artifacts. We used the ImageJ FFT bandpass filter, suppressing horizontal and vertical lines with a cut-off of 2500 pixels and 0 pixels with a 5% tolerance.

Chapter 5: Orally Available Near Infrared Imaging Agents for the Detection of Rheumatoid Arthritis

5.1 Publication Information

Bhatnagar S, Khera E, Liao J, Eniola V, Hu Y, Smith DE, Thurber GM. Self-Administration of Near-Infrared Fluorescent Imaging Agents for the Early Detection of Rheumatoid Arthritis. *Submitted*.

Modifications have been made to the published document to adapt the content to this dissertation.

5.2 Abstract

Rheumatoid arthritis (RA) is an inflammatory autoimmune disease that causes irreversible damage of the joints. However, effective drugs exist that can stop disease progression, and there is intense interest in early detection and treatment to improve patient outcomes. Imaging has the potential for early detection, but current methods lack sensitivity and/or are time-consuming and expensive. In this study, we examined self-administration of molecular imaging agents in the form of sub-cutaneous and oral delivery of an integrin binding near-infrared (NIR) fluorescent imaging agent to increase patient compliance for regular screening of RA. This technique, in comparison to current imaging modalities, has relatively low cost, high safety profile with the use of non-ionizing radiation, the ability to provide spatial and molecular information and is minimally invasive. This study shows significant uptake of an

IRdye800CW agent in inflamed joints of a CAIA mouse model compared to healthy joints, irrespective of the method of administration. The results were extrapolated to clinical depths using a 3D COMSOL model of NIR fluorescence imaging in a human hand. With target to background concentration ratios greater than 5.5, which is achieved in the mouse model, these probes have the potential to identify arthritic joints following oral delivery at clinically relevant depths.

5.3 Background

Rheumatoid arthritis (RA) is a chronic joint disease marked by pain and inflammation [258] that affects 0.5% to 1% of the population worldwide [259]. Despite several existing treatments and recent advances in disease therapy, remission rates and morbidity remain a critical concern for RA patients [260]. Given the irreversible damage caused by joint inflammation and prevalence of effective disease modifying drugs, it is widely viewed that earlier treatment is needed for more effective management of RA. There is also some evidence that early intervention, specifically in cases of RA, has the potential for curative treatment[261]. However, current blood tests do not have adequate sensitivity and specificity for accurate diagnosis, and these tests do not provide insight into local joint conditions. Therefore, new quantitative diagnostic methods are needed to identify the pathology at an early stage to reduce disease morbidity [262]. An inflamed synovial membrane is one of the earliest indications of the onset of RA [263]. Conventional imaging methods such as ultrasonography, provide a valid assessment of synovitis [264] but lack sensitivity for early arthritis signs [265]. Contrast enhanced magnetic resonance imaging (MRI), with its excellent soft tissue contrast, is able to provide details about inflammation within the joints and predict the disease progression at an early stage [266], but this method is time-consuming and expensive for routine screening applications [267].

Optical molecular imaging is considered a promising alternative method for early stage RA detection. It has the advantage of providing specific molecular information without the use of ionizing radiation used in PET and SPECT molecular imaging methods. There have been several reported correlations between the severity of joint inflammation and fluorescence intensities from molecular probes [134,268,269]. Indocyanine green (ICG), a non-specific dye that binds to plasma proteins, has been studied in a few reports since it is the only clinically approved near-infrared (NIR) dye [270]. Although ICG has been reported to differentiate RA joints from healthy joints during later stages of the disease [271], detection at the earliest stages, ideally subclinical inflammation for screening purposes, remains challenging and unrealized [134,135,272].

In order to make early detection of RA feasible using optical molecular imaging, it requires a route of administration that is safe, inexpensive, and convenient for patients (to improve compliance). Self-administration methods like subcutaneous injection (SC) and oral delivery (PO) are ideal for screening large portions of the population as it saves time, medical personnel costs, and are preferred by patients [148,149]. Intravenous delivery, the most common form of delivery of imaging agents, has a higher risk of adverse reactions [144,145]. While these absolute values are low, the risk in screening large numbers of patients, particularly in a healthy population, sets a high bar. Additionally, even the fastest clearing agents require imaging to take place several hours post administration to allow for the imaging agent to clear from the body, which results in multiple or extended visits to the clinic. These visits can increase cost from health care professional time required to dose the patients in a sterile manner and monitor the patients in case of adverse events. Self-administration of these imaging agents would allow for a single visit to the clinic for imaging thereby mitigating the costs of screening.

We developed an integrin ($\alpha_V\beta_3$) binding imaging agent that has been shown to efficiently target breast cancer in an orthotopic mouse model via oral administration (Chapter 4). We hypothesized that due to the high expression of $a_v\beta_3$ integrins on activated macrophages and the high macrophage infiltration in RA, we could use methods of self-administration to detect inflammation of the joints in arthritis. These imaging agents are comprised of a targeting ligand that binds integrin of the form $a_v\beta_3$ [97] conjugated to a negatively charged NIR fluorophore. Given the different transport rates in the synovial tissue compared to tumors, we tested two methods of self-administration: subcutaneous and oral delivery. In contrast to breast cancer, where a significant amount of NIR clinical imaging has been conducted to show the feasibility of imaging tumors imbedded deep within the breast tissue (Table 4.2), much of the clinical NIR imaging in RA has been done with non-targeted agents such as ICG. In order to efficiently test the translatability of these molecular imaging agents to humans at clinically relevant length scales, this study employed a three dimensional (3D) simulation utilizing previously validated models of diffuse light fluorescence imaging [273,274] to determine the necessary concentrations and targeting efficiency required for clinical early arthritis detection. To simulate the light scattering in an arthritic hand, we first used CAD software to construct the hand and synovial space around the metacarpophalangeal joint (MCP) of the middle finger based on published MR images. The fluence rate of emission light was then simulated using a finite element mesh function in COMSOL Multiphysics.

5.4 Results

Near-Infrared Integrin Imaging Agents and their Properties

The previous chapter showed that the negative charge on imaging agents can facilitate targeting following oral delivery by increasing the target specificity, extending circulation in the body long enough to be taken up by antigen positive cells, retaining the agent in cells after receptor mediated internalization (due to their residualizing nature), and increasing oral absorption. In this study, we employ this method for the detection of RA and study the differences between two negatively charged imaging agents – IRDye800CW and AF680 agents – for more detailed structure-function relationships. The structure and physicochemical properties of the two imaging agents are shown in figure 5.1. The two agents have similar molecular weights, formal charge and binding affinities, with the most notable differences being in their plasma protein binding (Table 5.1).

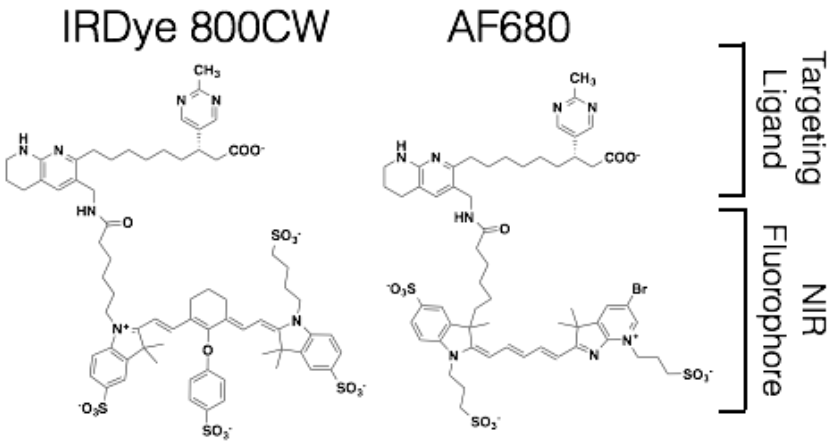

Figure 5.1 Imaging agent structures

Table 5.1 Physicochemical properties of both agents

	IRDye800CW	**AF680**
Molecular Weight	1393	1249
Excitation/Emission(nm)	774/789	679/702
Charge	-4	-3
Affinity ± S.D. (nM) [$\alpha_v\beta_3$]	1.7 ± 0.3	2.7 ± 0.6
Affinity ± S.D. (nM) [$\alpha_v\beta_5$]	1.5 ± 0.4	2.1 ± 0.4
Affinity ± S.D. (nM) [$\alpha_{iib}\beta_3$]	Not detectable	Not detectable
Effective Affinity ± S.D.	0.7 ± 0.3	1.1 ± 1.7

(nM) [RAW 264.7 cells]		
PPB ± S.D. (%)	91 ± 2	78 ± 3
% Absorbed - SC*	91 ± 10	100 ± 10
% Absorbed - PO*	2.3 ± 2.2	1.5 ± 1.3

Near-Infrared Integrin Imaging Agents Target Inflamed Joints after Subcutaneous Injection

To study the effect of the physicochemical properties of the two agents on absorption and targeting, they were administered subcutaneously in CAIA mouse models. Both agents are rapidly absorbed with high subcutaneous bioavailability (Table 5.1). Images at 48 hours post SC injection (Fig. 5.2) showed that the inflamed joints (arrow) had significantly higher signal than non-inflamed joints (arrowheads) for the IRDye800CW agent but was similar for the AF680 agent. Healthy mice were also injected with the same doses of the both agents, and showed significantly lower signal for the IRDye800CW agent ($p<0.0001$) and not significantly different signal for the AF680 agent when compared to inflamed joints (Fig. 5.2).

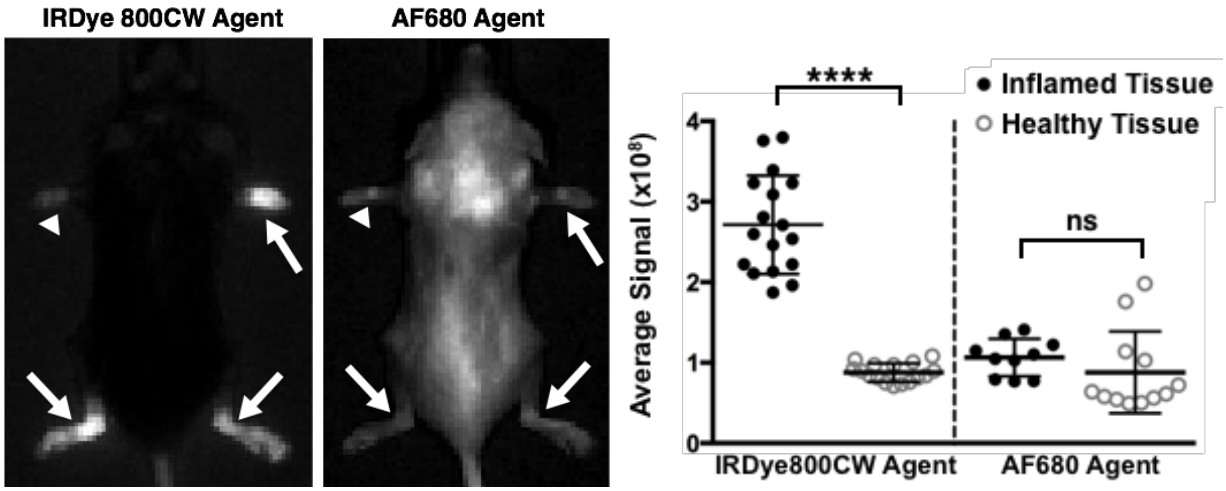

Figure 5.2 RA detection and average signal difference between inflamed and healthy tissue post SC delivery at 48 hours.

The biodistribution data shows lower uptake of the AF680 probe likely due to the faster clearance of the AF680 probe from the body (Fig. 5.3) [163]. The above results along with the higher oral absorption led to the selection of the IRDye800CW agent for oral delivery.

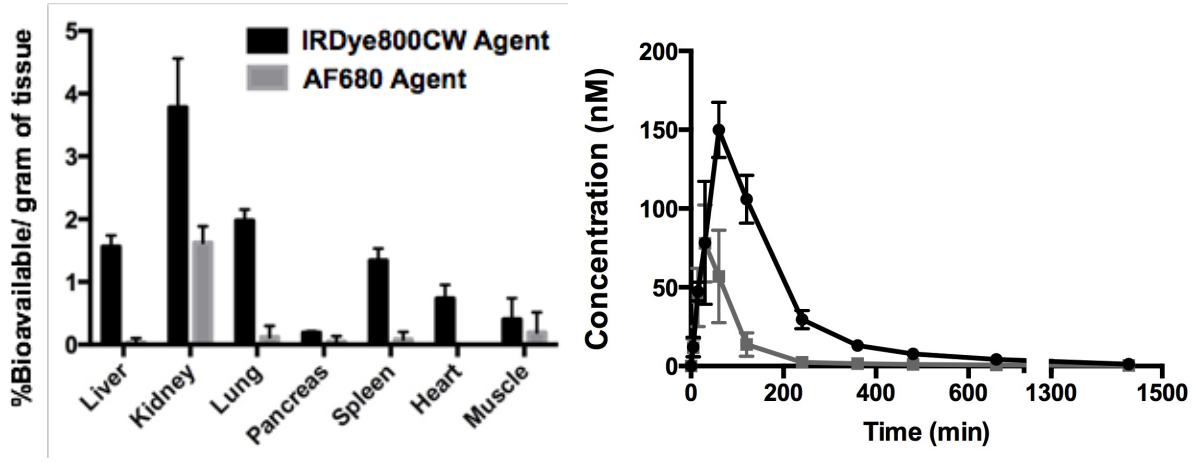

Figure 5.3 Biodistribution and plasma clearance at 48 hours post SC delivery

Oral Delivery of IRDye800CW Integrin Agent Targets Macrophages in Inflamed Joints

The IRDye800CW agent showed high uptake in inflamed joints when delivered subcutaneously and orally. A low affinity stereoisomer of the targeting ligand was conjugated with IRDye800CW and dosed orally in mice with inflamed joints. SC delivery gave the highest specific signal at 6 hours post administration versus 24 hours for PO delivery. This is likely attributed to the kinetics of absorption for the two routes of administration. The time of maximum plasma concentration for SC and PO delivery are 1 hour and 2.5 hours[275] post administration, respectively. The signal in the healthy joints continued to drop with time, which increased the contrast between inflamed and healthy paws at 48 hours (Fig. 5.4). The low uptake of low affinity agent in the joints of these mice confirmed the targeting specificity of the high affinity agent.

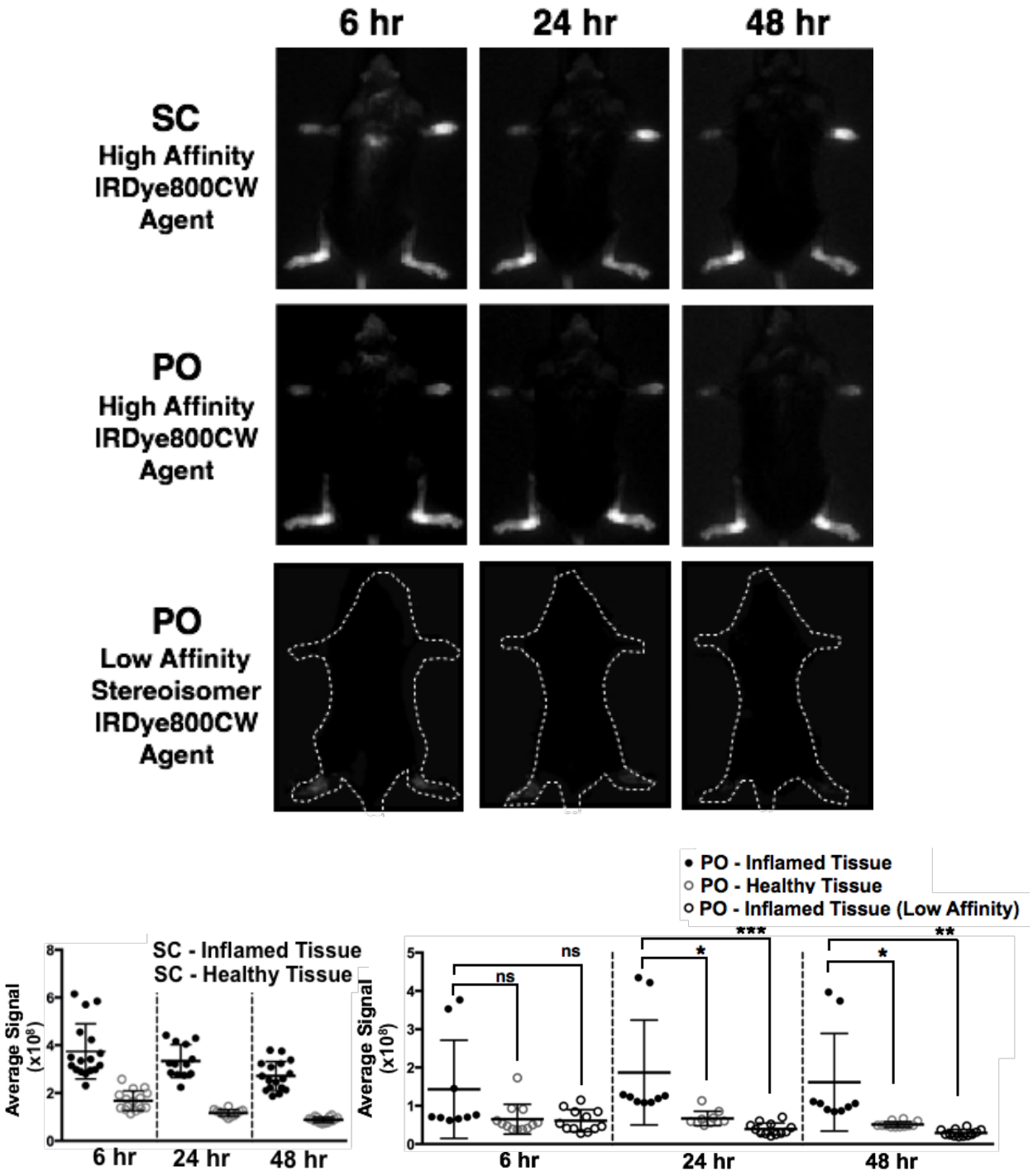

Figure 5.4 Whole animal fluorescence images and average signal at 6, 24 and 48 hours

The biodistribution data was similar for the high affinity agent irrespective of the route of delivery and significantly lower for the low affinity binder.

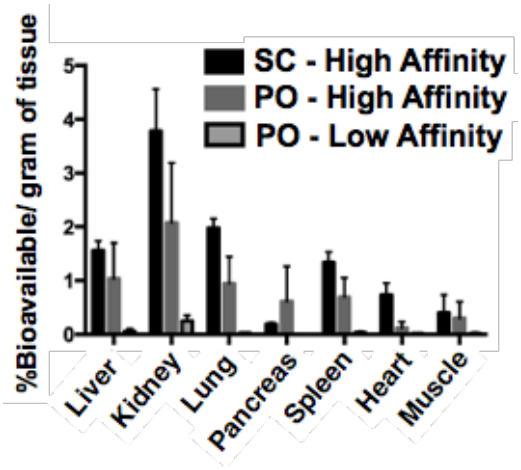

Figure 5.5 Biodistribution data at 48 hours post delivery

Ex-vivo labeling of histology slides showed macrophage infiltration in the inflamed ankles and lack of staining in the healthy ankles (Fig. 5.5). The presence of macrophages correlated with significant uptake of the orally delivered IRDye800CW agent in inflamed ankles, and low uptake of the low affinity stereoisomer highlighted the specificity of the imaging agent.

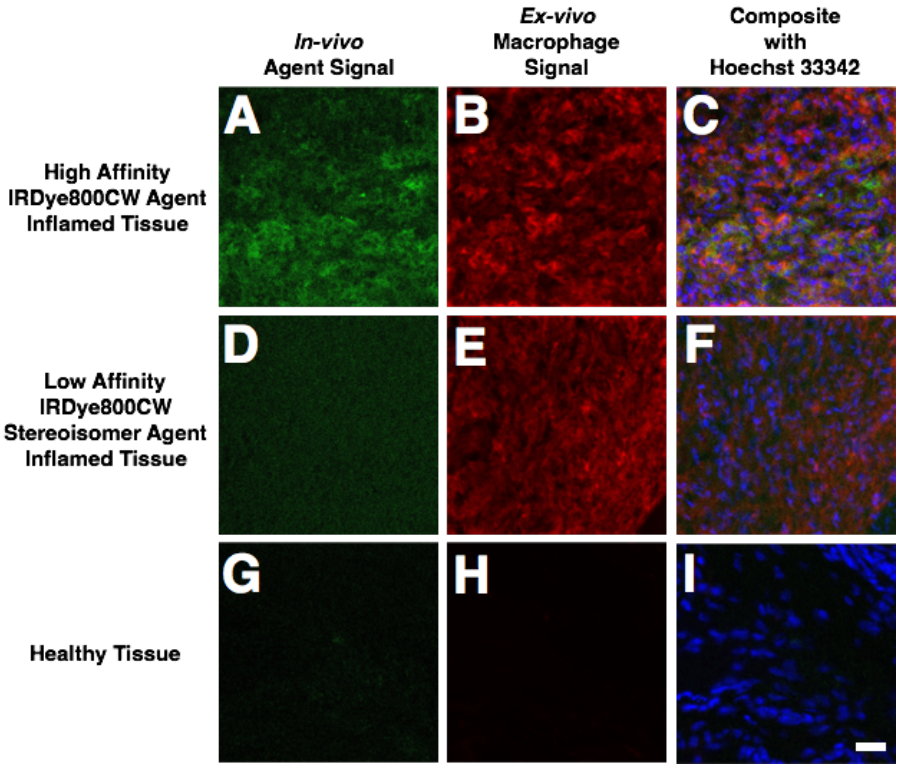

Figure 5.6 Histology staining of ankle tissue from mice

Computational Modeling Indicates Targeting Efficiencies are Sufficient for Detection at Clinical Depths

A potential limitation of this technique for detecting clinical RA is the depth of imaging of NIR fluorescence. To facilitate translation between the animal model results and clinical depths, we created a CAD model of a human hand to simulate NIR epifluorescence imaging of targeted molecular imaging agents in the synovial tissue at clinically relevant depths (Fig.5.6). Based on the thickness of the tissue relative to the scattering length of NIR light, the diffusion approximation was used along with a light source located one scattering length within the top surface of the hand. The joint location is below this depth based on MRI images. High resolution images of the hand joint [276] were used to generate a 3D model of the synovial space where molecular imaging agents would bind their target during inflammation. The shape and thickness of the synovial space was based on sagittal, coronal and transverse images of the joint.

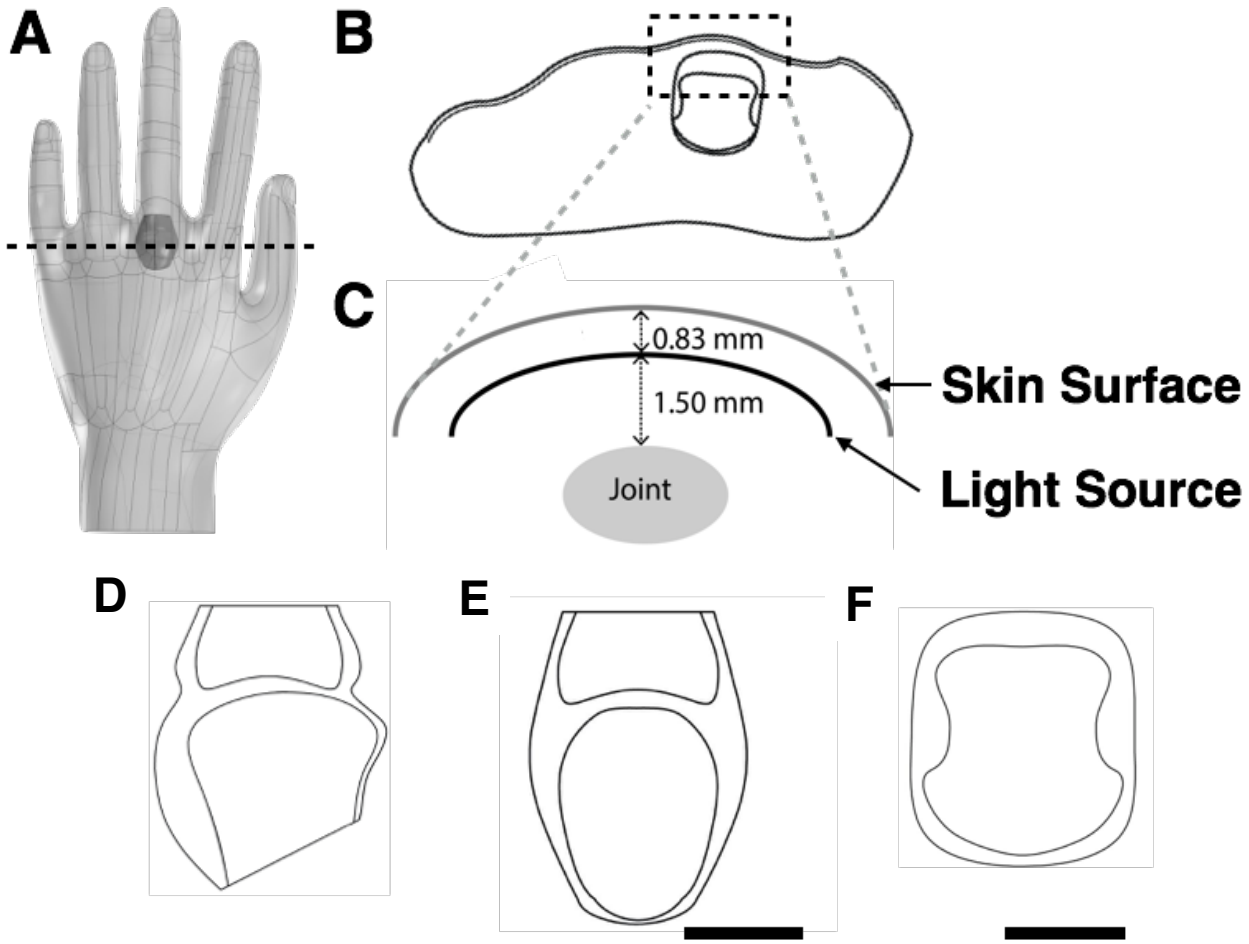

Figure 5.7 Schematics of hand and joint placement used in the COMSOL model

(A) CAD file of the hand and synovial space with 0% swelling. (B) A cross-sectional view (at the dotted line in A) of the synovial space based on an MRI of the metacarpophalangeal joints from Nieuwenhuis et al. [277]. (C) A zoomed in representation of the box in B showing the light source placed one scattering distance below the skin surface. (D-F) Model of the synovial membrane based on MR images from Theumann et al[276]. Scale bar = 10 mm.

A two-step simulation in COMSOL was employed where the excitation light was first simulated from a planar source shining on top of the hand and used to calculate the imaging agent absorption and emission. The excited agent then acted as the source for the emission light simulation. The imaging agent concentration in the synovial tissue was varied while the concentration in the remainder of the tissue was kept at a constant level to capture background autofluorescence and non-specific agent accumulation in healthy tissue. Surface fluence was

used to determine the image intensity while varying the concentration ratio between the synovial tissue and hand. Optical phantoms were used to validate the simulations, and the experimentally measured TBR values were similar to those predicted by the simulation. The concentration ratios between the synovial space and surrounding tissue (e.g. 10:1) were proportional to the TBR as expected (Fig 5.7). The discrepancy between the optical phantom and the simulations likely resulted from the increased experimental depth, measured at 3.4 mm for the 5:1 and 2.6 mm for the 10:1 phantoms, compared to the depth of 2.3 mm in the simulation.

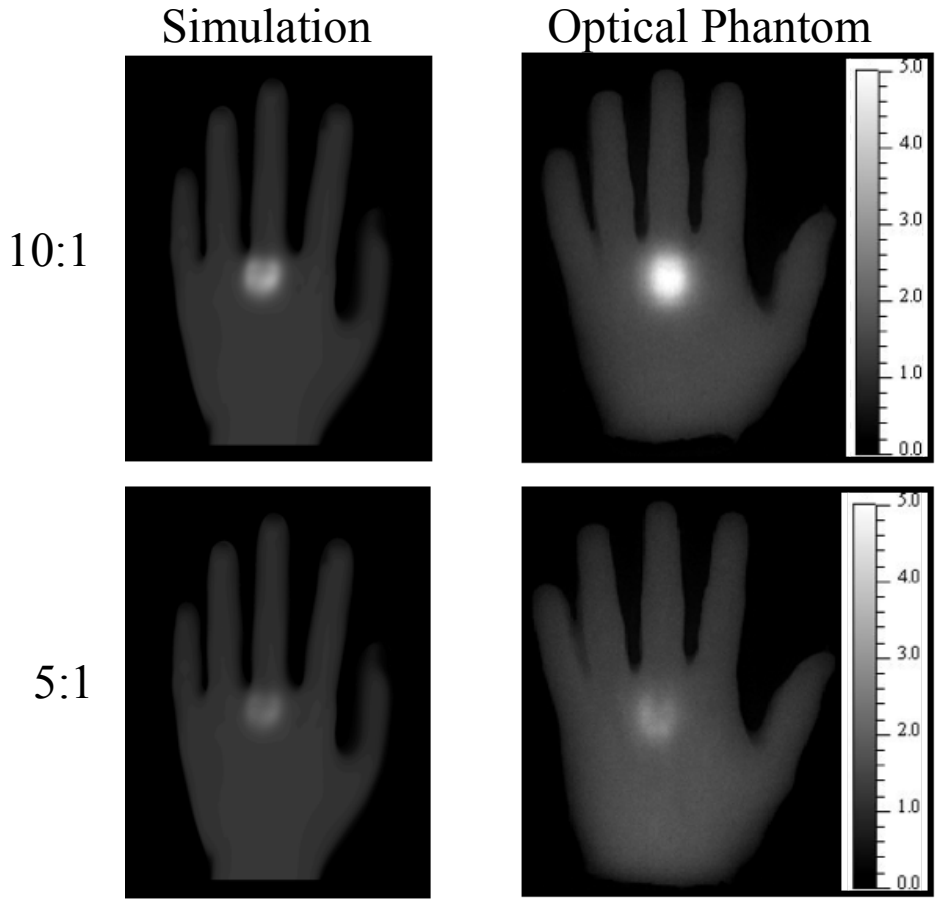

Concentration Ratio	COMSOL Predicted TBR	Optical Phantom TBR	Phantom depth (mm)
10:1	3.1 ± 0.1	3.2 +/- 0.7	2.6 +/- 0.5
5:1	1.92 ± 0.09	1.7 +/- 0.1	3.4 +/- 0.9

Figure 5.8 COMSOL model and optical phantom results

For positive identification of an inflamed joint, the signal must be higher than the background variability (the contrast to noise ratio). While the actual values may vary due to the reasons listed above, 64% variability in the background intensity was chosen as a reasonable estimate of late imaging time background standard deviation and the origin of this value is explained further in the discussion section. Since the average signal from the joint would be compared to a background signal with a measured standard deviation, assuming a Gaussian distribution in the background signal compared to a fixed value of joint signal, the threshold CNR for detection is similar to a z statistic. From the cumulative normal distribution table, a CNR of 1.65 gives a 95% probability of positive signal relative to the background. Therefore, interpolating the CNR values from Table 5.2, probes with 5.5:1 and 6.5:1 concentration ratios between synovial tissue and background tissue are necessary for a 95% and 98% probability of positive detection of inflammation, respectively. Based on the estimated concentration ratios from mice, this level of contrast is achieved with these agents following either oral or SC delivery (Fig. 5.8).

Table 5.2 TBR values from COMSOL model for varying concentration ratios

TBR	10:1	5:1	2:1	1:1
0%	3.1 ± 0.1	1.92 ± 0.09	1.23 ± 0.06	1.04 ± 0.05
5%	3.2 ± 0.1	1.98 ± 0.09	1.25 ± 0.06	1.04 ± 0.05
10%	3.3 ± 0.1	2.01 ± 0.09	1.26 ± 0.06	1.04 ± 0.05
20%	3.4 ± 0.2	2.09 ± 0.09	1.29 ± 0.06	1.04 ± 0.05

Table 5.3 CNR values from COMSOL model for varying concentration ratios

CNR	10:1	5:1	2:1	1:1
0%	3.2 ± 0.2	1.4 ± 0.1	0.36 ± 0.09	0.07 ± 0.07
5%	3.4 ± 0.2	1.5 ± 0.1	0.38 ± 0.09	0.07 ± 0.07
10%	3.5 ± 0.2	1.6 ± 0.1	0.41 ± 0.09	0.07 ± 0.07
20%	3.8 ± 0.2	1.7 ± 0.1	0.44 ± 0.09	0.07 ± 0.07

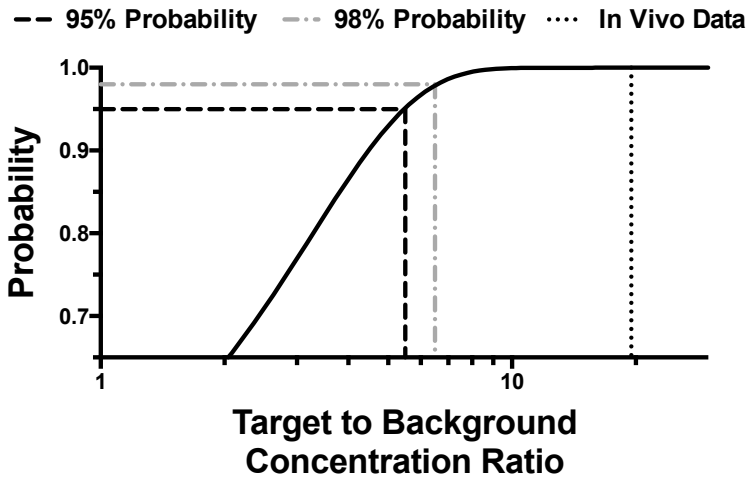

Figure 5.9 Probability of RA detection based on COMSOL results

Required concentration ratio for positive identification based on the z-statistic and the estimated concentration ratio achieved in the mouse model.

5.5 Discussion

Early detection of RA could enable therapeutic intervention before the disease has caused significant irreversible damage, thereby improving patient outcomes. Clinical data suggests that it may even be possible to cure the disease if diagnosed early and accurately[278]. Imaging results from ultrasound and MRI are a proven indicator of RA development independent of autoantibody status and clinical features. However, both methods have limitations for widespread screening. NIR fluorescence molecular imaging has the potential to detect the disease in a minimally invasive manner by providing both spatial and molecular information within the joints. This imaging modality would have several advantages over ultrasound by simultaneously capturing data from multiple joints using FDA approved NIR hand scanners and yielding quantitative molecular information from targeted probes. The cost of imaging and time for acquisition is also much less than MRI, and it has safety benefits from the use of non-ionizing radiation relative to PET and SPECT molecular imaging modalities. Current clinical efforts have focused on non-targeted ICG given its FDA approval for imaging in the clinic. However, the low

contrast provided by this non-specific protein-binding dye requires dynamic imaging [279] to parse increased uptake in the joints from normal background and surface vessel fluorescence. Targeted imaging could provide significantly higher contrast ratios for more definitive image analysis, diagnosis, and follow up testing. Therefore, researchers are exploring a variety of imaging agents including ^{99m}Tc-MDP [280], PSVue 794 [281], αCD11b-APC combined with MMP750 [282], NIR2-folate [283], MMP-3 specific polymeric probe using NIRF [284], protease activated NIRF probes (sensitive to Cathepsin B) [268], integrins [285,286] and AP39-TSC [287]. The research into new imaging agents continues in order to develop probes capable of detecting this early stage of the disease. However, many of these methods include intravenous delivery and/or radiolabels, and the required imaging agent uptake ratios and molecular targets have not been analyzed in a quantitative fashion over clinically relevant length scales. In this work, we used an integrin binding ligand conjugated with a NIR fluorophore and tested its ability to detect RA in a CAIA mouse model using SC and oral delivery. We also simulated NIR fluorescence imaging of targeted synovial tissue in a human hand while varying the target to background ratios using COMSOL Multiphysics to determine the translatability of this technique to humans.

Due to their efficient targeting and optical properties, the IRDye800CW and AF680 agents were delivered by SC and oral administration in a mouse CAIA model of RA. Our previous work showed high affinity for $\alpha_v\beta_3$ in transfected HEK-293 cells (Chapter 3). In the current study, we tested the affinity in a plate assay to 3 different heterodimers, $\alpha_v\beta_3$, $\alpha_{iib}\beta_3$ and $\alpha_v\beta_5$, and in mouse macrophage cells (RAW 264.7 cells). Interestingly, the affinity of the AF680 probe was much higher for $\alpha_v\beta_3$ in the context of cells. However, the slightly better affinity as measured using the plate assay and mouse macrophage cells is more consistent with the low uptake *in vivo*. Although the targeting ligand has high specificity for $\alpha_v\beta_3$ over $\alpha_v\beta_5$ [97], the

modification with these two dyes increases the cross-reactivity with $\alpha_v\beta_5$, which is also upregulated on macrophages [82]. However, no binding to $\alpha_{iib}\beta_3$ was detected (Table 5.1), which is important to avoid any safety issues with binding to this heterodimer on platelets[288]. Both the agents are structurally very similar, with the AF680 agents having the benefit of faster clearance from the body, which reduces background signals. However, the IRDye800CW agent performed significantly better than the AF680 during *in vivo* experiments. The rapid clearance of the AF680 agent is not beneficial when there is a significant absorption phase, such as SC or oral delivery, in contrast to IV delivery. Rapid clearance during the absorption phase results in lower maximum concentrations within the body. Another reason is that the autofluorescence in the 680 channel is higher than the 800nm channel, compounding the issue of low concentrations in the blood.

The IRDye800CW agent showed specific targeting and high target to background ratios in the CAIA mouse model when delivered subcutaneously, and given the similar kinetics following oral delivery, we hypothesized it would provide specific targeting following oral administration. Fig. 5.4 confirmed this hypothesis with the major difference between the two methods of administration being the higher variability in target tissue and background following oral delivery. The low-affinity stereoisomer of the IRDye agent had lower uptake following oral adminsitraiton than the healthy mice, indicating some binding to integrins in the healthy tissue. Microscopically, significant uptake is seen in macrophages in and around the synovium in inflamed joints (Fig. 5.6). Both delivery methods produce signals higher than seen in healthy joints, especially at later times. The subcutaneous route results in less variability in absorption; however, both the signal and background intensities are proportional to the absorbed dose, so the TBR is similar between both routes.

Based on the TBR achieved in the animal experiments, we next used computational modeling to scale the results to clinical depths. This was achieved by building an optical imaging COMSOL model to simulate various target to background concentration ratios and different extents of joint swelling (Fig. 5.7). The results showed that the TBR and CNR values are strongly affected by the target to background concentration ratio and only weakly impacted by the extent of joint swelling i.e. thickness of the synovium. The regions of interest used to calculate the TBR and CNR avoided the diffuse light at the edges of the joint. The optical phantom experiments were conducted to validate the *in silico* results, and these data were largely in agreement. The standard deviation for the experimental data was large owing mainly to the experimental error in placing the joint at a certain depth below the surface of the hand. The simulations had the joint at 2.33 mm from the surface, whereas experimentally that distance ranged from 2.5 to 4 mm.

Based on the COMSOL simulations, these results can be used to aid in NIR fluorescence molecular imaging agent design for RA. First, a minimum concentration ratio must be achieved for signal detection above background fluctuations. Random fluctuations of the background signal introduce noise to the image, impairing the image detectability. As it is important to distinguish true joint inflammation from signal fluctuations in normal tissue for accurate diagnosis, the detectability should be high, which is best described by the CNR [289]. The variability in background signal is a complex function of the imaging probe properties, background tissue physiology, imaging time versus pharmacokinetics, characteristics of the imaging system, and optical properties of the probe and tissue. In general, early imaging times after imaging agent delivery have the potential for increased heterogeneity in the background due to large gradients between the blood and tissue, while at longer times these gradients have

dissipated. Likewise, the background signal in the NIR region is often dominated by non-specific probe signal rather than autofluorescence, lowering the impact of optical properties and instrumentation (where spectral deconvolution, for example, would not improve the contrast for probe-dominated background signal). To obtain a reasonable estimate for this variability, reported mouse and clinical data were used to estimate the background standard deviation. These data were taken at long times after administration (24 hrs post-injection) to minimize variability due to transient redistribution from the blood. Assuming that the variability correlates with the background signal (i.e. a higher absolute background signal results in higher absolute variability such that the standard deviation is proportional to the signal), a previous report in mice indicated a background variability of 64% for antibodies 72 hr after delivery [274]. A clinical imaging sample indicated a background variability (after subtracting non-tissue signal from the in vivo background signal and error propagation) of 51% at 24 hrs post-injection of the small molecule ICG [290]. While the actual values may vary due to the reasons listed above, 64% variability in the background intensity was chosen as a reasonable estimate of late imaging time background standard deviation.

To estimate the required CNR values for clinical detection, we examined the probability of positive identification of an inflamed joint. According to the Rose Criterion, the CNR of an object must exceed 3 to 5 in order to be considered detectable [291]. It is also possible to identify signal with a CNR less than 3, but it suffers from a higher probability of misidentification. For example, an image with CNR of 2 has a probability to misidentify signals from one tissue to another of 16% [292]. However, the Rose Criterion applies to situations where the location of the target is unknown, such as identification of a breast tumor[293]. When imaging the hand, the intensity of signal from the joints is compared to the background (non-joint) tissue, both with

anatomically defined locations. Since the average signal from the joint would be compared to a background signal with a measured standard deviation, assuming a Gaussian distribution in the background signal compared to a fixed value of joint signal, the threshold CNR for detection is similar to a z statistic. From the cumulative normal distribution table, a CNR of 1.65 gives a 95% probability of positive signal relative to the background. This corresponds to a target to background concentration ratio of ~5.5:1 and a concentration ratio of ~6.5-1 is required for a 98% probability in detection.

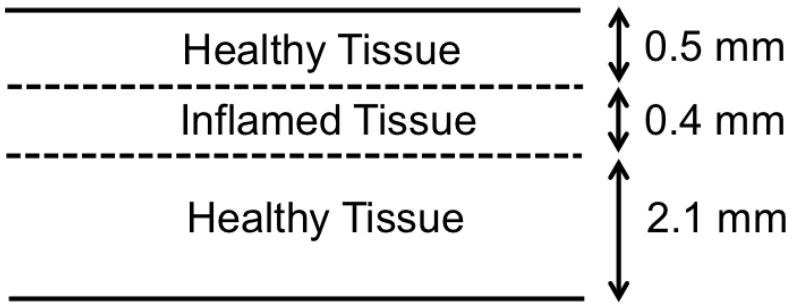

Figure 5.10 Concentration ratio scale up

Schematic of inflamed paw with epifluorescence imaging (excitation and emission occurring from the top). A healthy paw would have an identical schematic without the inflamed tissue.

Average healthy paws: 2.6mm
Average extent of inflammation: 0.4mm
Imaging intensity ratio between inflamed paws and healthy paws (TBR) = 4

Two approaches were used to scale the imaging signal intensity to the concentration ratio between inflamed and healthy paws: a simple linear scaling shown below and a diffuse light approximation of fluorescence intensity[294]. Both results gave similar answers, which was anticipated given the small thickness of the mouse paw relative to NIR light penetration. For the linear scaling, let the concentration in the inflamed tissue be X nM and in the healthy tissue be Y nM.

$$TBR = \frac{Concentration\ in\ Inflamed\ Paw}{Concentrati\square n\ in\ Healthy\ Paw}$$

$$TBR = \frac{0.5\ (Y) + 0.4\ (X) + 2.1\ (Y)}{2.6\ (Y)} = 4$$

Solving the equation, we get $\frac{X}{Y} = 19.5$

The concentration ratio of inflamed to healthy tissue is 19.5. By scaling the concentrations from the CAIA mouse model (Fig. 5.10), we demonstrate that this ratio is ~4 times larger than the theoretical requirement and should be sufficient for detection at clinical depths.

Simulations can also guide target selection. If the background signal from autofluorescence and non-cleared probe is on the order of 3-5 nM (which is highly dependent on the instrument but estimated based on the IVIS imaging system), a 10:1 ratio would require ~30 to 50 nM of probe in the target tissue. Assuming $5x10^8$ cells/mL, this requires ~40,000 to 60,000 receptors per cell if the target is universally expressed. If only 25% of the cells in the synovium express the target, these requirements reach ~200,000 receptors/cell. This is assuming an agent based on binding rather than amplification from enzyme activation. Few targets have this high level of expression, but the $\alpha_V\beta_3$ integrin and folate receptor are two promising candidates (Table 5.4). The $\alpha_V\beta_3$ expresses ~$1.7x10^5$ receptors per activated endothelial cell [224], $2x10^5$ receptors per macrophage [225], and 10^6 receptors per osteoclast [295]. It also has a clinical precedent with radiolabeled molecules [286]. Similarly, the folate receptor is expressed at $3.2x10^5$ receptors per macrophage [296] and has a clinical precedent [297]. Notably, radiolabeled agents achieved a 90 nM concentration within the joints [298]. Ultimately, these values may need to be updated when new experimental measurements are available, but they provide a benchmark for comparison during probe development.

Table 5.4 Potential targets for RA detection

Target	Expression	Drug	Size	Affinity	Reference
Integrin $\alpha_v\beta_3$	$1.7x10^5$ (endothelial cells) $2x10^5$ (macrophages) $1x10^6$ (osteoclasts)	Integrisense 750	1278 Da	4.2 nM	Kossodo 2010
		IRDye 800CW Agent	1397 Da	4.8 nM	Experimental
		AF680 Agent	1252 Da	0.3 nM	Experimental
		Antibodies	~150 kDa	0.1 nM	Barbas 1993
Folate Receptor	$3.2x10^5$ (activated macrophages)	Folic acid	441.4 Da	0.1 nM	Sudimack 2000
		^{99m}Tc-EC20	745.2 Da	3 nM	Leamon 2002
		EC0565	2740 Da	0.028 nM*	Lu 2015
		BGC 945	647.6 Da	~0.35 nM*	Gibbs 2005
RANK	-	RANKL	~35 kDa	0.109 nM	Zhang 2009
MMP	-	Sulfonamide Inhibitors	~400 Da	0.3 nM (MMP-13)	Lovejoy 1999
		Batimastat	478 Da	3 nM (MMP-1)	Botos 1996
		Marimastat	331 Da	5 nm (MMP-1)	Michaelides 1999
		Prinomastat	420 Da	17 nM (MMP-1)	Humphrey 2003
Adhesion Molecules	-	Rituximab	~145 kDa	Kd = 4.5 nM	Mössner 2010
		Ocaratuzumab	~145 kDa	Kd = 100 pM	
		Catumaxomab	~150 kDa	Kd = 0.56 nM	Ruf 2007
Chemokine Receptor	-	CXCL10 (IP-10)	8.8 kDa	Kd = 69 pM	Qin 1998
		CXCL9 (MIG)	11.7 kDa	Kd = 90 pM	
		MIP-1**β** (CCL4)	7.8 kDa	IC50 = 0.41 nM	Laurence 2001

Model Limitations

The order-of-magnitude values for fluorescence intensity and concentration ratios needed for clinical detection can provide guidance on the types of probes that should be developed. However, there are several limitations to the model. First, the 3D synovial space and hand are only approximations of the complex tissue structures present within the hand, which may impact light propagation. When drawing the joint in Solidworks, the exact 2D sketches of the joint were extracted from the three anatomical planes of its MR images (sagittal, coronal and transverse view). Then the 3D model was constructed by the lofting feature in Solidworks, using the three sketches of top, middle and bottom planes of the transverse view as bases, and sketches on sagittal and coronal planes as guidelines. Thus, although the model has the same anatomical cross-section views as the MR images, the overall 3D shape is an approximation based on the available MR images. Second, the optical phantom is also an experimental approximation of the behavior of light in living tissue. There are no internal boundaries in the optical phantom, and the absorption and scattering are homogeneous average values for tissue. Third, the variability in background signal intensity was estimated based on animal data and limited clinical data with ICG and could vary from the estimated value.

5.6 Conclusion

In conclusion, self-administered NIR fluorescence molecular imaging has strong potential to serve as an early detection method for rheumatoid arthritis due to its low cost, ease of use, and target specificity. The proper design of molecular imaging agents can ensure sufficient specific targeting to achieve the necessary sensitivity for accurate clinical screening and early therapeutic

intervention. The current COMSOL model results indicate sufficient signal at clinical depths for early detection of RA.

5.7 Experimental Methods

In Vivo Experiments

To determine the absorption following SC administration, 1.5 nmoles of the imaging agent (~0.1 mg/kg) were administered in separate 8-10 week old female black-6 mice via SC and intravenous (IV) injection (Fig. S2). Retro-orbital blood draws were conducted at 5, 15, 30, 60 120, 240, 360 and 1440 minutes post-administration for SC delivery and at 1, 3, 5, 15, 30, 60, 180, 360 and 1440 minutes post-administration for IV delivery. 10ul of blood was mixed with 20ul PBS-EDTA and spun down at 2000g for 1 minute. The plasma (supernatant) was then pipetted into a 384 well plate and the fluorescence of the sample was measured on the Odyssey CLx. The signal was converted into a plasma concentration of the imaging agent using a calibration curve in mouse plasma. Area under curves (AUC) for the mice were calculated using the trapezoidal rule and % absorbed was determined by the ratio of the AUC of SC to IV. For oral delivery, the percent absorbed was measured as previously reported in Bhatnagar et al[299].

The collagen antibody induced arthritis (CAIA) model was used for imaging (Chondrex; Redmond, WA). Female Balb/c mice of 8-10 weeks of age were used for this study. 1.5 mg of the antibody cocktail was administered by intraperitoneal (IP) injection into the mice (Jackson Laboratories; Bar Harbor, ME). 3 days later 50 ug of LPS was administered via IP injection. The extent of paw and ankle inflammation was measured using calipers, and once inflammation was seen (8-10 days after the antibody injection), the mice were administered doses of the imaging agents.

Imaging agents were administered by either SC injection (dorsal side between the shoulder blades) or oral to the CAIA model mice with inflamed joints or control mice with no inflammation. For SC, the mice were anesthetized using 2.5% isoflurane and the imaging agents were either co-administered at a dose of 1.5 nmole each in the same mouse or dosed individually at 1.5 nmole. For oral delivery, a 24-gauge needle (Fine Science Tools; Forster City, CA) was used to administer a 75 nmole dose. Post injection, the mice were imaged on an IVIS Spectrum (Perkin Elmer; Waltham, MA) at 6, 24 and 48 hours. After the 48-hour image the mice were euthanized and all their organs were resected for biodistribution. The ankle was snap frozen in OCT using isopentane cooled on dry ice for histology. The biodistribution protocol is previously reported (Chapter 4.7), but briefly the organs were minced with a razor blade, weighed, and digested in Eppendorf tubes using a collagenase (Worthington Biochemical; Lakewood, NJ; Cat. No. CLS-4) solution (5 mg/ ml) in RIPA buffer (Boston BioProducts; Ashland, MA) at 37°C for 20 minutes. The organs were sonicated, digested for 20 minutes at 37°C using a 50:50 trypsin and RIPA buffer solution and sonicated. A dilution series of the resulting mixture was scanned in a black walled 96-well plate using an Odyssey CLx. Absolute quantification was obtained by comparison with a calibration curve. The uptake values were normalized to the average amount of probe that reached the systemic circulation (absorbed dose) per gram of tissue.

Histology

The frozen ankle was sectioned into 10μm slices on a cryostat using a tungsten carbide blade. The tissue was not fixed to avoid loss of fluorescence signal. The slice was stained ex-vivo with an anti-Mac3 antibody (BD Biosciences; San Jose, CA) labeled with Alexa Fluor 555. The slides were then washed with PBS and imaged on an Olympus FV1200 confocal microscope with a 543 and 750 nm laser line.

Governing Equations for COMSOL Model

This model uses a steady state diffusion equation to approximate the propagation of light in highly scattering media based on the thickness of the human hand and high albedo of NIR light [274,276,277]:

$$\nabla \cdot -D\nabla u + \mu_a u = f$$

where u is the fluence rate of light, D is the diffusion coefficient, μ_a is the absorption coefficient, and f is the light source. Parameters used for the simulation are listed in Table S1 and S2. Both light properties of 800 nm and 680 nm dyes are considered. The problem is divided into two simulation steps: excitation followed by emission. For the excitation light:

$$\nabla \cdot -D\nabla u + \mu_a u = 0$$

The planar light source is positioned at one scattering distance below the top surface of the hand, where the scattering of the light is assumed to be isotropic (e.g. [274,300,301]). Fluorophores in the hand are excited by light based on their absorption coefficient and the photon density of the excitation light. They emit fluorescence signals based on their quantum yield, which propagates through the tissue and can be detected at the surface of the hand. Autofluorescence in the hand is also included in the model as an 'equivalent dye' concentration in the tissue. For the emission light:

$$\nabla \cdot -D\nabla u + \mu_a u = \eta \cdot \mu_{fx} \cdot u \cdot [C]_{joint}$$

Both the excitation and emission light simulations use Robin boundary conditions at the outer surface of the hand.

$$-\boldsymbol{n} \cdot -D\nabla u - u/(2 \cdot Cr) = 0$$

CAD Drawing of Hand MCP Joint Using SolidWorks

To obtain results at clinical relevant depths, a CAD hand file (GrabCAD; Cambridge, MA) was used and scaled to the size of a human hand. The planar light surface was created by duplicating the top surface of the hand using SolidWorks (SolidWorks; Concord, MA) and translating that surface one scattering distance beneath the top of the hand (Fig. 5.7). Next, the synovial space around the MCP joint in the middle finger of the hand was made using SolidWorks. The size and shape of the membrane (Fig. 5.7 D-F) was based on sagittal, coronal and transverse MR images of the MCP joint[276]. The size of the base case synovial membrane is referenced from the scale bar on the coronal and transverse views of the MR images. The membrane position in the hand is determined from the MR image.

Development of COMSOL Model

The Helmholtz equation in COMSOL Multiphysics (COMSOL Inc.; Burlington, MA) was used for simulating the light diffusion equation at steady state. The constructed CAD model was imported into COMSOL, and the parameters and boundary conditions of the diffusion equation were correspondingly assigned. The simulation involves two Helmholtz equations depicting the excitation and emission light separately. The finest tetrahedral mesh was used, and COMSOL solved the differential equations at a tolerance of 10^{-5} for four iterations. The simulated results were saved as images under volume mode for image post-processing.

Imaging Optical Phantoms

An optical phantom was used to validate the COMSOL predictions (Fig. 5.8). The same CAD file used for the COMSOL simulations was also used to make a replica of the synovial

space using 3D printing (Cube 2, Cubify). A silicone mold of a hand and the 3D printed synovial space was used to generate optical phantoms (Fig. 5.11), which consisted of 3% agarose gel (for structure), 1% Intralipid (Baxter, Deerfield, IL) and 50 ppm India ink to mimic the absorption and scattering properties of human tissue[274]. IRDye 800CW carboxylic acid (LI-COR Biosciences; Lincoln, NE) was added at a concentration of 10 nM to the hand to represent background signal and 50 nM or 100 nM to the synovial space to represent specific uptake. The synovial space was placed ~2.5 mm from the surface of the hand. Once the gel solidified, it was imaged on an IVIS Spectrum (Perkin Elmer; Waltham, MA) and the TBR was calculated using the LivingImage software (Perkin Elmer; Waltham, MA).

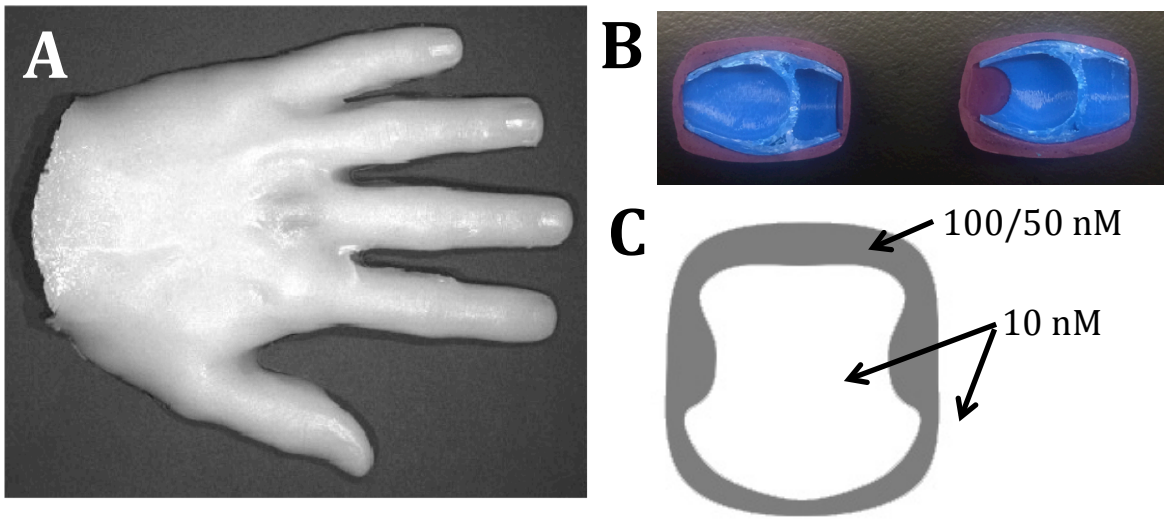

Figure 5.11 Optical Phantoms

(A) A silicone mold of a human hand was used to generate the optical phantom. (B) The CAD model of the synovium was used to 3D print a cast (blue) to generate a mold (purple) for the joint. (C) Cross-section of optical phantom, with the darker region being the joint. The grey region had either 100 or 50 nM of the dye and the healthy tissue in white had 10 nM of the dye.

Chapter 6: Conclusion

6.1 Summary

In this dissertation, we demonstrated that near infrared molecular imaging agents could be orally delivered to detect diseases like breast cancer and rheumatoid arthritis in mouse models. Chapter 2 dealt with the validation of a theoretical model that could predict delivery of drugs and imaging agents to tumors. The key challenges here were to make sure that the computational model was a accurate enough to be able to predict the distribution of drugs to tumors based on their physicochemical properties in spite of the heterogeneity in the tumor microenvironment. The previously published computational model showed that drugs could be categorized into four different classes based on their rate-limiting step of delivery[20]. The four classes are (I) blood flow limited, (II) extravasation limited, (III) diffusion limited and (IV) local binding/ metabolism limited agents. One drug or imaging agent was selected for each class based on computational predictions and non-overlapping fluorescence spectra. These agents were co-injected in the same mice to avoid tumor-to-tumor variability. The results showed that the computational model accurately described the delivery and distribution of these agents ranging from small molecules to antibodies in the tumor. This is of extreme importance as it exhibited that we could predict the delivery of these agents to tumors with knowledge of their physicochemical properties, which can be obtained from *in vitro* studies. Drug selection in the industry requires rigorous animal testing to prove that the agents work *in vivo*. This computational model can help reduce the amount of time, resources and animals required during

initial drug or imaging agent selection by eliminating these agents early on in their development if the model shows poor distribution. The model was used to guide our decision-making as we went about selecting the ideal imaging agent.

In order to find a molecular imaging agent that could be orally delivered we had to decide on the target and the ligand to be used. We selected integrin of the form $\alpha_v\beta_3$ because it is an extracellular target, has high expression on breast cancer cells and macrophages, internalizes at a relatively fast rate and has well-studied ligands against it. This dissertation was primarily a proof-of-concept study to show that detection of diseases was viable post oral administration, which led us to pick a target that had several studied ligands against it. This allowed us to circumvent the molecular screening step and select a ligand with optimal properties from the several published binders against $\alpha_v\beta_3$. Out of all the published ligands we selected a peptidomimetic (structure in Chapter 3.4) that has low molecular weight, high stability, low toxicity and high affinity to $\alpha_v\beta_3$. The ligand had been shown to retain its affinity to $\alpha_v\beta_3$ after conjugation to a NIR fluorophore[97]. Chapter 3 showed the synthesis of five different fluorophores to the ligand and their measured physicochemical properties. The five imaging agents were evaluated on three criteria: specific targeting, high oral absorption and good *in vivo* optical properties. Based on these criteria, the IRDye800CW agent, with an oral absorption of 2.3%, was selected for testing in *in vivo* for breast cancer detection. While the oral absorption is lower than typical small molecule therapeutics, it is relatively good compared to some other large hydrophilic molecules (Chapter 3.4) and fulfills the criteria needed for high contrast. The rule of thumb for oral absorption of therapeutics is about 30% since they need to saturate their target. Imaging agents, on the other hand, only need to be able to differentiate their target from background. As the percent oral absorbed increases, so does the signal from the target and

background thereby keeping the contrast the same. Therefore, imaging agents are less sensitive to the absolute amount absorbed. There is however a lower threshold below which the imaging agent is not efficient enough to target the diseased site, estimated to be about 1% in the mouse models, which the IRDye800CW agent is well above. It also needs to be highlighted that the oral absorption of these imaging agents was ascertained by measuring the amount of agent excreted in urine. Therefore, the oral absorption numbers are a conservative estimate of the total amount of agent orally absorbed.

The IRDye800CW agent was administered at a 5mg/kg dose to nude mice with tumor xenografts in their mammary fat pads. Live animal imaging at 6, 24 and 48 hours post administration showed that the amount of imaging agent in the tumors remained fairly constant over two days; however, the target to background ratio (TBR) increased with time to give a TBR of ~4 at 48 hours. The residualizing nature of the imaging agent causes it to remain trapped in the tumor while the imaging agent in the background, i.e. healthy tissue, is cleared from the body, giving higher TBR values. This was a validation of the initial hypothesis of this dissertation as it showed the detection of breast cancer after oral administration of an imaging agent that binds primarily to activated macrophages and to a lesser extent breast cancer cells and neovasculature. One of the biggest advantages of this technique over current techniques is that it has the ability to provide molecular information about the disease. In order to confirm that the imaging agent was being taken up specifically in the tumor to provide accurate molecular information, we used the stereoisomer of the ligand to synthesize a low affinity stereoisomer agent. It has an order of magnitude lower affinity to $\alpha_v\beta_3$. We dosed mice with 5 mg/kg of this control agent and saw significantly lower uptake in the tumors compared to the IRDye800CW

agent. This showed that the IRDye800CW agent was being taken up specifically in the tumor due to its interaction with the $\alpha_v\beta_3$ receptor.

With the positive identification of breast cancer in mice, we wanted to see if the same imaging agent would work in the detection of rheumatoid arthritis (RA) as well. Since the there is still a lot to be learned about transient kinetics of imaging agents in the RA microenvironment, we decided to subcutaneously (SC) deliver the imaging agent to make sure that we would be able to target the macrophages at the site of the disease. SC delivery has similar kinetics to oral delivery with a prolonged absorption phase followed by a clearance phase, but it does not have the animal-to-animal variability of oral delivery. We also tested another imaging agent in conjunction with the IRDy800CW agent, the AF680 agent. It has similar properties to the IRDye800CW agent, and since its excitation and emission maxima are very different from that of the IRDye800CW agent, we could co-administer both imaging agents in the same animal. We used a collagen antibody induced arthritis (CAIA) model in Balb/cJ mice and used a 0.1 mg/kg dose for SC delivery. The IRDye800CW agent was significantly better at identifying inflamed joints from healthy joints, with the AF680 agent not being able to differentiate between the two. The AF680 agent has lower plasma protein binding leading to faster clearance from the body and an area under the curve that is 4 fold lower than that of the IRDye800CW agent. The higher exposure of the IRDye800CW agent to the target is the reason for the IRDye800CW outperforming the AF680 agent. The IRDye800CW agent was then tested in the same CAIA mouse model via oral administration and the results showed statistically significant higher uptake in the inflamed joints compared to the healthy ones. We also used the low affinity stereoisomer control to demonstrate the specific uptake of the IRDye800CW agent in macrophages.

The biggest downside to using fluorescence as an imaging modality is its low depth of imaging. In order to test the feasibility of using epifluorescence to detect RA at clinically relevant depths in humans, we developed a 3D COMSOL model to run optical simulations and mimic the clinical setting. A CAD file of a human hand was built using measurements from published MRI scans and simulations were run testing different target to background concentration ratios. The target to background concentration ratios are the ratio of the amount of imaging agent delivered to the target, i.e. the inflamed joint, to the amount of imaging agent in background, i.e. rest of the hand. So, if the target to background concentration is 5, it means that the inflamed joint has a five times higher concentration of imaging agent than the rest of the hand. The model and its assumptions were validated using optical phantoms with the same target to background concentration ratios (Chapter 5.5). The simulations showed that with a target to background concentration ratio of 5.5 and 6.5, we have a 95% and 98% chance of detecting the inflamed joint. For reference, the *in vivo* data in mice showed a ~20 target to background concentration ratio giving us 3-4 fold buffer when translating this technique to humans.

In conclusion, we were able to show sufficient absorption and specific targeting of the IRDye800CW in the detection of breast cancer and RA. To implement this technique in the clinic, patients would self-administer these imaging agents approximately two days before imaging. When they are in the clinic, they can immediately be screened for these diseases. This method prevents the need for multiple visits: once to get intravenously injected with the imaging agent by a trained professional and then later to get imaged.

6.2 Future Work

This proof-of-concept study showed that molecular imaging agents can be orally administered and can identify the site of disease in mice. The development of this imaging agent

can be used as a model system to develop other agents that can bind to targets overexpressed in other diseases, thereby broadening the range of diseases that can be detected through annual screenings. Lowering the variability in the absorption of the imaging agent by using permeability enhancers can make the technique more robust.

Development of imaging agents

Since integrin $\alpha_v\beta_3$ is highly expressed on macrophages that are present at sites of inflammation, this imaging agent alone runs the risks of identifying sites of inflammation as breast cancer itself. The best way to reduce these false positives would be to co-administer another molecular imaging agent that binds a different biomarker and provides more molecular information about the disease. The integrin agent would then provide high sensitivity while the second agent would improve the specificity. Future work will involve identifying potential targets for co-administration of the imaging agents and ideal ligands to bind to these targets. The imaging agents will have excitation and emission spectra in the 600-700 nm range to avoid overlap with the IRDye800CW agent. Initial theoretical research suggests that calcium-chelating agents would be ideal as a second imaging agent. Literature shows the presence of calcium deposits in certain breast cancers[302], which would mean that high signal from both the imaging agents would indicate the presence of a tumor rather than being a false positive. Other potential targets for breast cancer are prostate specific membrane antigen (PSMA) and matrix metalloproteinases (MMPs), both of which are upregulated in breast cancers, have low or no expression in healthy tissue, and are extracellular targets[303,304]. In the case of RA, the calcium chelating agents would bind to bone and the integrin binding agents would bind to macrophages. The ratio between two agents would potentially help us differentiate between RA and ankylosing

spondylitis. Higher signal from the calcium-chelating agent would suggest ankylosing spondylitis, whereas higher signal from the integrin binder would suggest RA. This would help avoid misidentifying the disease in RA since both of diseases have inflammation around the joints as a symptom.

Reducing variability in oral absorption

One potential issue with this technique is the high variability in the administered oral dose. Below a certain threshold of absorption, the signal from the site of disease is not sufficient to provide high contrast to noise due to low uptake from the circulation. One method of reducing this variability and potentially increasing the absorbed fraction is the use of permeability enhancers like in the case of semaglutide[305], which is in phase 3 clinical trials. Permeability enhancers like fatty acids could help increase the amount of dose absorbed thereby providing more robust signal using this technique.

Our hypothesis for absorption of these large hydrophilic molecules is the amphiphilic structure of the imaging agents, with a lipophilic ligand conjugated to a hydrophilic fluorophore. We hypothesized that if we could make the ligand portion of the imaging agent more lipophilic we could potentially get higher absorption. Fig. 6.1 shows the structures of the imaging agent used in this dissertation and the more lipophilic version of it with the carboxylic acid replaced with an ester. Preliminary studies show that the absorption using the prodrug version of is more consistent and is higher than the carboxylic acid version (Fig. 6.1). Next steps will include studying the affinity of the prodrug imaging agent to $\alpha_v\beta_3$, its cleavage by carboxylesterases in blood and identifying what fraction of the dose is cleaved when collected in urine.

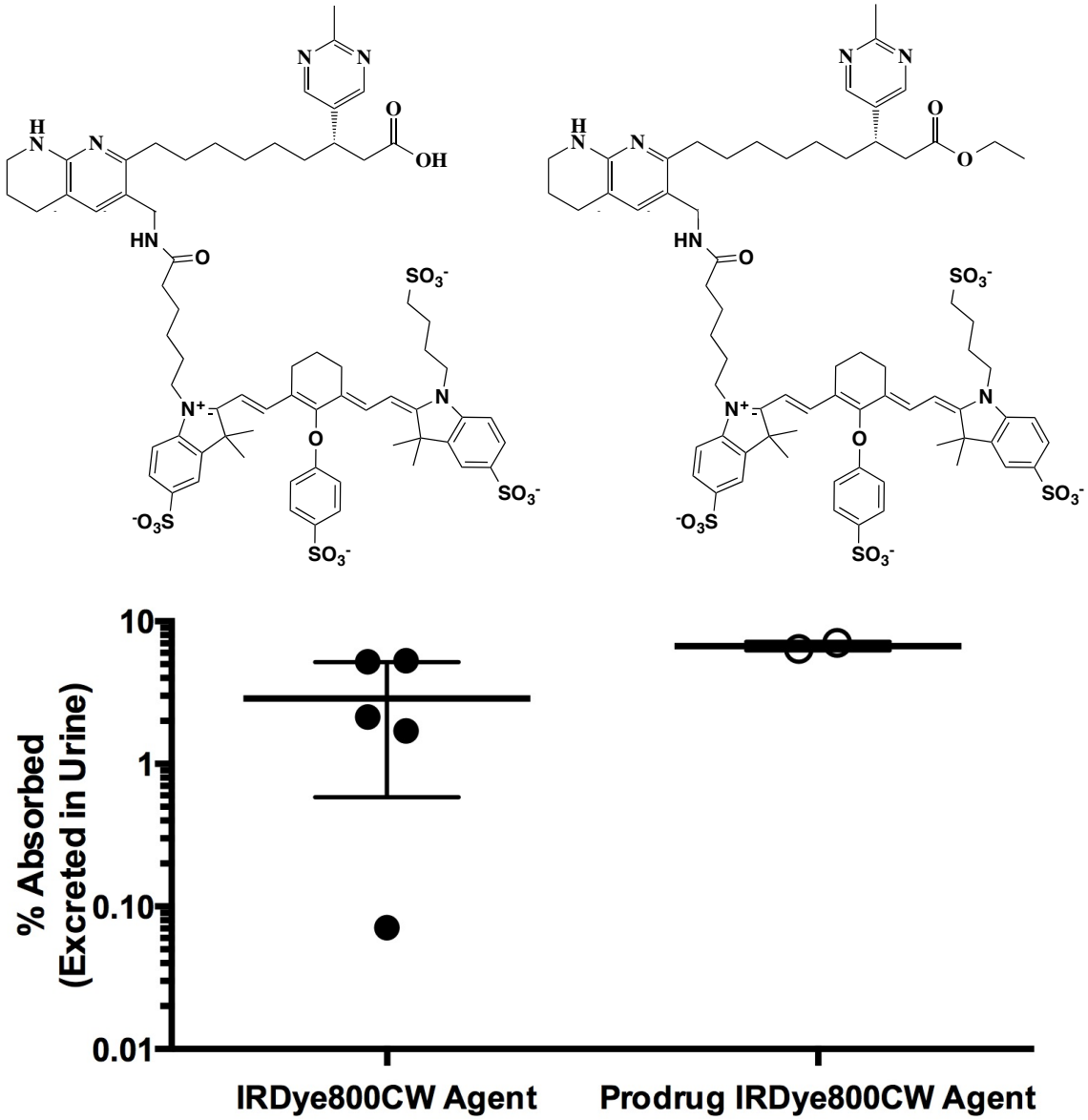

Figure 6.1 Structure and oral absorption of the IRDye800CW agent and its prodrug version

Early detection in RA

For the purposes of these proof-of-concept studies we had diseases in their peak states. The eventual goal is to be able to detect the disease early on. In order to identify how early on after the onset of the disease we can identify it, future work will involve inducing RA in rats and orally dosing the imaging agents at varying times post induction to identify the time at which we can confidently diagnose the disease.

Treatment monitoring

Another application of orally delivered imaging agents, other than early detection, is treatment monitoring. The current standard of treatment is weekly doses of methotrexate and treatment monitoring follow ups are subjective and conducted after several weeks to months. It would be ideal to have a quantitative method to measure the response at the diseased site days after treatment to offer the doctor with more information about whether the dose needs to be increased or if they need to switch to a biologic dose. The technique proposed in this dissertation would be ideal to monitor to the treatment of the disease. After starting treatment the patient could take a pill of the imaging agent every 2-3 weeks and could be imaged by their doctor to ascertain whether there needs to be any change in the course of action or if the disease is being treated adequately. Since this technique provides quantitative data, doctors can follow the data over time to make more informed decisions regarding the health of their patients. Future work to show the benefits of this method, rats will be induced with RA, treated with methotrexate and will be dosed with the imaging agent and imaged periodically to follow the progression of the disease.

In summary, we will work on developing orally available imaging agents for different targets to co-administer two imaging agents and provide extensive molecular information about the disease. Permeability enhancers or the prodrug approach will be studied to provide consistent and sufficient delivery of imaging agents post oral delivery. The imaging agents will be used in rat models to study how early RA is detectable and to provide quantitative data for treatment monitoring to indicate any required increases in dosage or frequency of doses.

6.3 Challenges and Future Directions

Fluorescent imaging agents have enormous potential in modern medicine. The last decade has seen several studies conducted on the use of specific and non-specific fluorescent agents for guided surgeries. Their ability to provide high spatial resolution in surgeries is highly beneficial to patient outcomes, as is the low risk (non-ionizing radiation) of the imaging modality. Another avenue being actively studied is the use of biologics as imaging agents, where highly specific antibodies can easily be tagged with NIR fluorophores. These can be used either in surgeries as their high specificity can clearly help delineate healthy and diseased tissue or can be self-administered for disease detection (e.g. research in oral cancer detection). The versatility of these imaging agents lies in the fact that these fluorophores can be easily conjugated with ligands (small molecules or biologics) and are stable over long periods of time compared to radiotracers with half-lives ranging from hours to days. They have fundamental advantages over related techniques, such as providing molecular information (compared to anatomical imaging), the spatial location of these biomarkers (compared to blood tests), and are less expensive with lower risks from non-ionizing radiation (compared to PET or SPECT modalities). However, there are limitations and challenges that lie ahead before routine implementation in the clinic.

Specifically for the proposed method presented in this thesis, future challenges include the sensitivity and specificity of the method in breast cancer and rheumatoid arthritis, the oral absorption in humans versus rodents and associated variability, and the logistics surrounding the implementation of a new imaging modalities. Each one of these aspects is presented below along with some potential avenues forward to overcome these challenges.

Sensitivity and Specificity for Screening

With respect to the sensitivity and specificity for breast cancer detection, the primary concern for sensitivity is the spatial resolution of lesions embedded deep in breast tissue. This is because the biomarker is found on tumor associated macrophages, neovasculature, and most breast cancer cells, therefore, the expression should occur in most/all tumors. Studies using diffuse optical tomography and non-specific agents have demonstrated the ability to detect tumors of ~1cm (and ~8mm in diameter for phantoms with similar contrast ratios). The expectation is that using molecular imaging agents for this purpose could help detect lesions smaller than 1cm in size due to the high specificity of the agents. Tumors smaller than this would require an alternative technique, but it is still unclear whether these smaller tumors are important for detection. Some evidence indicates that the tumors detected at a small size may typically be slower growing tumors that may not require treatment. Future studies from mammography results should help shed light on these issues. If these small lesions are important to reduce mortality, there is also ongoing research in techniques like high dynamic range fluorescence laminar optical tomography and optoacoustic imaging that can help increase the spatial resolution and depth of imaging of this technique, respectively.

For specificity, a major challenge is differentiating benign versus malignant tumors. Although $\alpha_v\beta_3$ expression is higher on more aggressive tumor types, it is also expressed in some benign lesions such as fibroadenomas. One benefit of fluorescence imaging agents is the ability to co-administer a pair of imaging agents that have little to no overlap in their excitation-emission spectra. This allows for multi-channel imaging to screen multiple biomarkers of the same disease to help differentiate malignant vs. benign disease. If the specificity from multiple biomarkers is not sufficient, then this method may be primarily suited for women with dense

breast tissue, since the NIR approach would allow better detection in these women. Because women with dense breast tissue have a higher risk of breast cancer and are more challenging to image using mammography, this is currently a major unmet clinical need in this patient population.

For rheumatoid arthritis, one issue when using these imaging agents in RA detection is determining the appropriate patient population for screening. There are several clinical trials designed to treat early, even subclinical, patients from high-risk groups. These clinical trials are based on genetic factors and autoantibodies that show up in routine blood tests. Although the risk of developing RA in these patients is significantly elevated over the normal population, the prevalence is still low, so only a fraction of these patients will actually develop the disease. Therefore, the biomarkers from blood tests and family history may serve as an excellent 'pre-screening' tool to select the population for an imaging screen. These patients, along with those with diffuse symptoms (e.g. undifferentiated arthritis) would be prime candidates for a quantitative screen.

A second issue is differentiation with other forms of arthritis. These include other diseases with a similar prevalence, such as ankylosing spondylitis. Although the clinical presentation of these diseases are different, differential diagnosis at early stages can be challenging. It may be possible that a more quantitative imaging screen, such as the one proposed here, will be able to better differentiate these conditions compared to a clinical exam. However, this would need to be determined through a controlled clinical trial. Alternatively, pairing the current agent, which quantifies inflammation and should have high sensitivity (due to the high expression level on activated macrophages) with a second NIR agent that differentiates the conditions (improving specificity) would be ideal. This work is continuing in the Thurber lab.

As a parallel application in RA, this method may have applicability for the early monitoring of treatment response. Typically, once a patients starts a new therapy, the physician will follow up within several weeks to months to see if the treatment is effective. For example, the follow up visits may determine whether the patient needs to move from a small molecule drug, like methotrexate, to a more expensive but powerful biologic. By using the technique described in this thesis, the patient could undergo a repeat scan within days to see if the inflammation was subsiding at the molecule level, thereby avoiding any additional damage prior to switching treatment if required.

Variability in animals and humans

The technique proposed in this dissertation was tested in rodent models of disease, specifically an orthotopic breast cancer model and CAIA model of RA. Continued work is needed to see how the pharmacokinetics (absorption and clearance) scale to other species. One of the main challenges is accommodating the high patient-to-patient variability. Although the contrast is not highly impacted by the amount of absorption, it can be affected if the absorption drops below a level necessary for detection above autofluorescence. The variability in absorption in other species and the clinic is currently unknown and needs to be tested in ongoing work. There is clinical evidence for similar sized hydrophilic molecules, as cited in our publications, that the levels will be similar to the amount absorbed in rodents. However, this must be directly measured for the molecules employed in this work. If challenges exist, proper formulation may be able to overcome and/or improve the amount absorbed in humans and remains a focus in ongoing work.

Logistics of implementation in the clinic

In addition to the scientific challenges described above, there are clinical and business factors to consider. One significant challenge faced by fluorescent imaging agents is the strong precedence for the deeply ingrained imaging modalities like PET, SPECT, CT, MRI etc. in the medical industry. The decades-long history of mammography is particularly entrenched in the cancer screening field, and the mixed clinical outcomes (successes in early detection weighed against the costs of over-diagnosis) have made this a highly controversial topic. There is also resistance to change in any large organized system.

There is no one solution to overcoming these non-scientific (but very real) challenges. However, if continued progress in the scientific challenges shows that this is ultimately a more successful approach, then several points must be clearly presented to the clinical community to help facilitate change.

First, the approach must clearly show superiority to current methods (e.g. mammography). Using an analogy from the pharmaceutical industry, this method would be promoted as 'best-in-class' versus 'first-in-class,' which would then allow it to gain in market share for breast cancer screening. To justify this continued development of molecular imaging with NIR tomography, for example, it needs to be emphasized that the fundamentals for this approach are superior to those used by mammography (and many newer techniques under development) and help address many of its limitations. Anatomical imaging will never be able to provide molecular information, and cancer is ultimately a molecular disease. This disconnect is a major driver of overdiagnosis. Second, it does not use ionizing radiation, so the associated cancer risks are much lower. Finally, a significant effort has already developed clinical-grade equipment for use with these molecular imaging agents.

A second issue is the experience and perception among physicians. Many may be more comfortable with a technique that has been used for many years. For practical implementation in breast cancer, the method would likely initially be used in women with dense breast tissue, since they have limited benefit from mammography (and contrast-enhanced MRI is expensive). The convenience of taking a pill versus receiving IV contrast and long scan times for MRI would likely cause patients to prefer a NIR tomographic scan. Once more experience was gained in this patient population, it would be easier to implement in a wider patient population. While experience with any technique is important, this cannot be the driving argument for screening; otherwise, physicians would always use the oldest technology available.

A third factor to consider is the use in other diseases. One of the most widely used NIR imaging agents in the clinic is the untargeted dye ICG, developed around WWII. It is generally used because it is clinically available rather than because of any particular strengths as an imaging agent. It is untargeted, has poor optical properties other than an ideal excitation/emission, and clears rapidly through the liver. If some of these agents were FDA approved for screening one disease, it would lower the bar to testing in clinical trials for different indications. Even if better agents were developed in the future, now the tables would be turned, and the orally available probe would be first-in-class.

The targeted NIR imaging agents provide molecular information about disease sites, but the high scattering of NIR light dramatically limits the spatial resolution for deep-tissue imaging. This makes it ideal for pairing with other modalities with better spatial resolution – multi-modal imaging. The most promising avenue might be pairing ultrasound with fluorescence molecular imaging agents to provide anatomical and molecular information at the same time. Ultrasound aligns well with many of the strengths of NIR imaging (both generally low cost, no ionizing

radiation, potential for combining with other techniques like optoacoustic imaging, etc.). Similar to the strengths of combining PET and SPECT with CT or MRI, the NIR imaging would provide molecular information while ultrasound provides anatomical information (and maybe physiological info for more complex methods such as Doppler US and photoacoustic imaging).

In conclusion, in spite of the limitations and drawbacks of this technique, it has tremendous promise in the medical industry. The modality itself is continuously evolving with great strides being made in increasing spatial resolution and depth of imaging. The ability to non-invasively detect diseases using a low-risk imaging modality that has the potential of high compliance rates can significantly help improve patient outcomes with the early detection of diseases.

References

1. Etzioni R, Urban N, Ramsey S, McIntosh M, Schwartz S, Reid B, Radich J, Anderson G, Hartwell L 2003. The case for early detection. Nature reviews Cancer 3(4):243-252.

2. Bradley WG 2008. History of medical imaging. Proceedings of the American Philosophical Society 152(3):349-361.

3. Scatliff JH, Morris PJ 2014. From Roentgen to magnetic resonance imaging: the history of medical imaging. North Carolina medical journal 75(2):111-113.

4. Hutton BF 2014. The origins of SPECT and SPECT/CT. European journal of nuclear medicine and molecular imaging 41(1):3-16.

5. Choyke PL, Kobayashi H 2012. Medical Uses of Fluorescence Imaging: Bringing Disease to Light. IEEE Journal of Selected Topics in Quantum Electronics 18(3):1140-1146.

6. Gillenwater A, Jacob R, Ganeshappa R, et al. 1998. Noninvasive diagnosis of oral neoplasia based on fluorescence spectroscopy and native tissue autofluorescence. Archives of Otolaryngology–Head & Neck Surgery 124(11):1251-1258.

7. Kinch MS, Woodard PK 2017. Analysis of FDA-approved imaging agents. Drug discovery today 22(7):1077-1083.

8. Agdeppa ED, Spilker ME 2009. A Review of Imaging Agent Development. The AAPS journal 11(2):286-299.

9. James ML, Gambhir SS 2012. A Molecular Imaging Primer: Modalities, Imaging Agents, and Applications. Physiological reviews 92(2):897-965.

10. James ML, Gambhir SS 2012. A molecular imaging primer: modalities, imaging agents, and applications. Physiological reviews 92(2):897-965.

11. Imai MDT, Takahashi MDK, Fukura MDH, Morishita MDY 1997. Measurement of Cardiac Output by Pulse Dye Densitometry Using Indocyanine Green A Comparison with the Thermodilution Method. Anesthesiology 87(4):816-822.

12. Cooke AR, Harrison DD, Skyring AP 1963. Use of indocyanine green as a test of liver function. The American Journal of Digestive Diseases 8(3):244-250.

13. Spaide RF, Klancnik JM, Jr, Cooney MJ 2015. Retinal vascular layers imaged by fluorescein angiography and optical coherence tomography angiography. JAMA Ophthalmology 133(1):45-50.

14. Hadjipanayis CG, Widhalm G, Stummer W 2015. What is the Surgical Benefit of Utilizing 5-Aminolevulinic Acid for Fluorescence-Guided Surgery of Malignant Gliomas? Neurosurgery 77(5):663-673.

15. Weissleder R 2001. A clearer vision for in vivo imaging. Nat Biotech 19(4):316-317.

16. Frangioni JV 2003. In vivo near-infrared fluorescence imaging. Current Opinion in Chemical Biology 7(5):626-634.

17. Pansare VJ, Hejazi S, Faenza WJ, Prud'homme RK 2012. Review of Long-Wavelength Optical and NIR Imaging Materials: Contrast Agents, Fluorophores, and Multifunctional Nano Carriers. Chemistry of Materials 24(5):812-827.

18. van Dam GM, Themelis G, Crane LMA, Harlaar NJ, Pleijhuis RG, Kelder W, Sarantopoulos A, de Jong JS, Arts HJG, van der Zee AGJ, Bart J, Low PS, Ntziachristos V 2011.

Intraoperative tumor-specific fluorescence imaging in ovarian cancer by folate receptor-α targeting: first in-human results. Nature medicine 17:1315.

19. Hilderbrand SA, Weissleder R 2010. Near-infrared fluorescence: application to in vivo molecular imaging. Current Opinion in Chemical Biology 14(1):71-79.

20. Lipinski CA 2004. Lead- and drug-like compounds: the rule-of-five revolution. Drug Discovery Today: Technologies 1(4):337-341.

21. Goel S, Duda DG, Xu L, Munn LL, Boucher Y, Fukumura D, Jain RK 2011. Normalization of the Vasculature for Treatment of Cancer and Other Diseases. Physiological Reviews 91(3):1071-1121.

22. Secomb TW, Hsu R, Park EYH, Dewhirst MW 2004. Green's function methods for analysis of oxygen delivery to tissue by microvascular networks. Annals of Biomedical Engineering 32(11):1519-1529.

23. Helmlinger G, Sckell A, Dellian M, Forbes N, Jain RK 2002. Acid Production in Glycolysis-impaired Tumors Provides New Insights into Tumor Metabolism. Clinical Cancer Research 8:1284-1291.

24. Jain RK 1999. Transport of molecules, particles, and cells in solid tumors. Annual review of biomedical engineering 1:241-263.

25. Minchinton AI, Tannock IF 2006. Drug penetration in solid tumours. Nature Reviews Cancer 6(8):583-592.

26. Ohtani H 1998. Stromal reaction in cancer tissue: pathophysiologic significance of the expression of matrix-degrading enzymes in relation to matrix turnover and immune/inflammatory reactions. Pathology international 48(1):1-9.

27. Grantab R, Sivananthan S, Tannock IF 2006. The penetration of anticancer drugs through tumor tissue as a function of cellular adhesion and packing density of tumor cells. Cancer Res 66(2):1033-1039.

28. Baxter LT, Jain RK 1989. Transport of fluid and macromolecules in tumors. I. Role of interstitial pressure and convection. Microvasc Res 37(1):77-104.

29. Karnoub AE, Dash AB, Vo AP, Sullivan A, Brooks MW, Bell GW, Richardson AL, Polyak K, Tubo R, Weinberg RA 2007. Mesenchymal stem cells within tumour stroma promote breast cancer metastasis. Nature 449(7162):557-563.

30. Jain RK, Ward-Hartley K 1984. Tumor Blood Flow-Characterization, Modifications, and Role in Hyperthermia. Sonics and Ultrasonics, IEEE Transactions on 31(5):504-525.

31. Dreher MR, Liu W, Michelich CR, Dewhirst MW, Yuan F, Chilkoti A 2006. Tumor Vascular Permeability, Accumulation, and Penetration of Macromolecular Drug Carriers. Journal of the National Cancer Institute 98(5):335-344.

32. Kovtun YV, Audette CA, Ye Y, Xie H, Ruberti MF, Phinney SJ, Leece BA, Chittenden T, Blättler WA, Goldmacher VS 2006. Antibody-Drug Conjugates Designed to Eradicate Tumors with Homogeneous and Heterogeneous Expression of the Target Antigen. Cancer Research 66(6):3214-3221.

33. Dreher MR, Liu WG, Michelich CR, Dewhirst MW, Yuan F, Chilkoti A 2006. Tumor vascular permeability, accumulation, and penetration of macromolecular drug carriers. Journal of the National Cancer Institute 98(5):335-344.

34. Gerlowski L, Jain RK 1986. Microvascular Permeability of Normal and Neoplastic Tissues. Microvascular Research 31:288-305.

35. Champion JA, Mitragotri S 2006. Role of target geometry in phagocytosis. Proceedings of the National Academy of Sciences of the United States of America 103(13):4930-4934.

36. Hamblett KJ, Senter PD, Chace DF, Sun MM, Lenox J, Cerveny CG, Kissler KM, Bernhardt SX, Kopcha AK, Zabinski RF, Meyer DL, Francisco JA 2004. Effects of drug loading on the antitumor activity of a monoclonal antibody drug conjugate. Clinical cancer research : an official journal of the American Association for Cancer Research 10(20):7063-7070.

37. Rhoden JJ, Wittrup KD 2012. Dose dependence of intratumoral perivascular distribution of monoclonal antibodies. Journal of Pharmaceutical Sciences 101(2):860-867.

38. Weissleder R, Tung CH, Mahmood U, Bogdanov A 1999. In vivo imaging of tumors with protease-activated near-infrared fluorescent probes. Nature biotechnology 17(4):375-378.

39. Su H, Seimbille Y, Ferl GZ, Bodenstein C, Fueger B, Kim KJ, Hsu YT, Dubinett SM, Phelps ME, Czernin J, Weber WA 2008. Evaluation of [F-18]gefitinib as a molecular imaging probe for the assessment of the epidermal growth factor receptor status in malignant tumors. European journal of nuclear medicine and molecular imaging 35(6):1089-1099.

40. Thurber GM, Weissleder R 2011. Quantitating antibody uptake in vivo: conditional dependence on antigen expression levels. Molecular imaging and biology : MIB : the official publication of the Academy of Molecular Imaging 13(4):623-632.

41. Cai WB, Chen K, He LN, Cao QH, Koong A, Chen XY 2007. Quantitative PET of EGFR expression in xenograft-bearing mice using Cu-64-labeled cetuximab, a chimeric anti-EGFR monoclonal antibody. European journal of nuclear medicine and molecular imaging 34(6):850-858.

42. McLarty K, Cornelissen B, Scollard DA, Done SJ, Chun K, Reilly RM 2009. Associations between the uptake of In-111-DTPA-trastuzumab, HER2 density and response to

trastuzumab (Herceptin) in athymic mice bearing subcutaneous human tumour xenografts. European journal of nuclear medicine and molecular imaging 36(1):81-93.

43. Aerts H, Dubois L, Perk L, Vermaelen P, van Dongen G, Wouters BG, Lambin P 2009. Disparity Between In Vivo EGFR Expression and Zr-89-Labeled Cetuximab Uptake Assessed with PET. J Nucl Med 50(1):123-131.

44. Milenic DE, Wong KJ, Baidoo KE, Ray GL, Garmestani K, Williams M, Brechbiel MW 2008. Cetuximab: Preclinical Evaluation of a Monoclonal Antibody Targeting EGFR for Radioimmunodiagnostic and Radioimmunotherapeutic Applications. Cancer Biother Radiopharm 23(5):619-631.

45. Mullani NA, Herbst RS, O'Neil RG, Gould KL, Barron BJ, Abbruzzese JL 2008. Tumor blood flow measured by PET dynamic imaging of first-pass F-18-FDG uptake: A comparison with O-15-Labeled water-measured blood flow. J Nucl Med 49(4):517-523.

46. Patlak CS, Blasberg RG, Fenstermacher JD 1983. Graphical Evaluation of Blood-to-Brain Transfer Constants from Multiple-Time Uptake Data. J Cereb Blood Flow Metab 3(1):1-7.

47. Thurber GM, K.S. Yang, T. Reiner, R.H. Kohler, P. Sorger, T. Mitchison, and R. Weissleder 2013. Single-cell and subcellular pharmacokinetic imaging allows insight into drug action in vivo. Nature communications 4:1504.

48. Poulin P, Theil FP 2002. Prediction of pharmacokinetics prior to in vivo studies. II. Generic physiologically based pharmacokinetic models of drug disposition. Journal of pharmaceutical sciences 91(5):1358-1370.

49. Peters SA 2008. Evaluation of a generic physiologically based pharmacokinetic model for lineshape analysis. Clinical pharmacokinetics 47(4):261-275.

50. Rowland M, Peck C, Tucker G. 2011. Physiologically-Based Pharmacokinetics in Drug Development and Regulatory Science. In Cho AK, editor Annual Review of Pharmacology and Toxicology, Vol 51, 2011, ed., Palo Alto: Annual Reviews. p 45-73.

51. Ferl GZ, Wu AM, DiStefano JJ 2005. A predictive model of therapeutic monoclonal antibody dynamics and regulation by the neonatal fc receptor (FcRn). Annals of Biomedical Engineering 33(11):1640-1652.

52. Garg A, Balthasar JP 2007. Physiologically-based pharmacokinetic (PBPK) model to predict IgG tissue kinetics in wild-type and FcRn-knockout mice. J Pharmacokinet Pharmacodyn 34(5):687-709.

53. Thurber GM, Weissleder R 2011. A Systems Approach for Tumor Pharmacokinetics. PLoS ONE 6(9).

54. Graham J, Muhsin M, Kirkpatrick P 2004. Cetuximab. Nature Reviews Drug Discovery 3(7):549-550.

55. Astsaturov I, Cohen RB, Harari PM 2006. EGFR-targeting monoclonal antibodies in head and neck cancer. Current Cancer Drug Targets 6(8):691-710.

56. Thurber GM, Schmidt MM, Wittrup KD 2008. Antibody tumor penetration: Transport opposed by systemic and antigen-mediated clearance. Advanced Drug Delivery Reviews 60(12):1421-1434.

57. Lammler G, Herzog H, Saupe E, Schutze HR 1971. Chemotherapeutic studies on Litomosoides carinii infection of Mastomys natalensis. 1. The filaricidal action of 2,6-bis-benzimidazoles. Bulletin of the World Health Organization 44(6):751-756.

58. Chaplin DJ, Olive PL, Durand RE 1987. Intermittent Blood-Flow in a Murine Tumor - Radiobiological Effects. Cancer Research 47(2):597-601.

59. Trotter MJ, Chaplin DJ, Olive PL 1989. Use of a Carbocyanine Dye as a Marker of Functional Vasculature in Murine Tumors. 59(5):706-709.

60. Coleman PJ, Brashear KM, Askew BC, Hutchinson JH, McVean CA, Duong LT, Feuston BP, Fernandez-Metzler C, Gentile MA, Hartman GD, Kimmel DB, Leu CT, Lipfert L, Merkle K, Pennypacker B, Prueksaritanont T, Rodan GA, Wesolowski GA, Rodan SB, Duggan ME 2004. Nonpeptide alpha(v)beta(3) antagonists. Part 11: Discovery and preclinical evaluation of potent alpha v beta(3) antagonists for the prevention and treatment of osteoporosis. J Med Chem 47(20):4829-4837.

61. Kossodo S, Pickarski M, Lin S-A, Gleason A, Gaspar R, Buono C, Ho G, Blusztajn A, Cuneo G, Zhang J, Jensen J, Hargreaves R, Coleman P, Hartman G, Rajopadhye M, Duong LT, Sur C, Yared W, Peterson J, Bednar B 2009. Dual In Vivo Quantification of Integrin-targeted and Protease-activated Agents in Cancer Using Fluorescence Molecular Tomography (FMT). Molecular Imaging and Biology.

62. Balaz 2009. Modeling Kinetics of Subcellular Disposition of Chemicals. Chemical Reviews 109:1793-1899.

63. Arndt-Jovin DJ, Jovin TM 1977. Analysis and sorting of living cells according to deoxyribonucleic acid content. The journal of histochemistry and cytochemistry : official journal of the Histochemistry Society 25(7):585-589.

64. Thurber GM, Figueiredo JL, Weissleder R 2009. Multicolor Fluorescent Intravital Live Microscopy (FILM) for Surgical Tumor Resection in a Mouse Xenograft Model. PLoS ONE 4(11):e8053.

65. Boucher Y, Baxter LT, Jain RK 1990. Interstitial Pressure-Gradients in Tissue-Isolated and Subcutaneous Tumors - Implications for Therapy. Cancer Research 50(15):4478-4484.

66. Jain RK, Baxter L 1988. Mechanisms of Heterogeneous Distribution of Monoclonal Antibodies and Other Macromolecules in Tumors: Significance of Elevated Interstitial Pressure. Cancer Research 48:7022-7032.

67. Swartz MA 2001. The physiology of the lymphatic system. Advanced Drug Delivery Reviews 50(1-2):3-20.

68. Thurber GM, Wittrup KD 2008. Quantitative spatiotemporal analysis of antibody fragment diffusion and endocytic consumption in tumor spheroids. Cancer Research 68:3334-3341.

69. Adams G, Schier R, McCall A, Simmons H, Horak E, Alpaugh K, Marks J, Weiner L 2001. High Affinity Restricts the Localization and Tumor Penetration of Single-Chain Fv Antibody Molecules. Cancer Research 61:4750-4755.

70. Rudnick SI, Lou JL, Shaller CC, Tang Y, Klein-Szanto AJP, Weiner LM, Marks JD, Adams GP 2011. Influence of Affinity and Antigen Internalization on the Uptake and Penetration of Anti-HER2 Antibodies in Solid Tumors. Cancer Research 71(6):2250-2259.

71. Heijn M, Roberge S, Jain RK 1999. Cellular membrane permeability of anthracyclines does not correlate with their delivery in a tissue-isolated tumor. 59(17):4458-4463.

72. Müller M, Keimling R, Lang S, Pauli J, Dahmen U, Dirsch O. 2009. Estimating Blood Flow Velocity in Liver Vessels. In Meinzer H-P, Deserno T, Handels H, Tolxdorff T, editors. Bildverarbeitung für die Medizin 2009, ed.: Springer Berlin Heidelberg. p 36-40.

73. Sturesson C, Milstein DMJ, Post I, Maas AM, van Gulik TM 2013. Laser speckle contrast imaging for assessment of liver microcirculation. Microvascular Research 87:34-40.

74. Jain RK 1999. Transport of Molecules, Particles, and Cells in Solid Tumors. Annual Reviews in Biomedical Engineering 01:241-263.

75. Baker J, Lindquist K, Huxham L, Kyle A, Sy J, Minchinton A 2008. Direct Visualization of Heterogeneous Extravascular Distribution of Trastuzumab in Human Epidermal Growth Factor Receptor Type 2 Overexpressing Xenografts. Clinical Cancer Research 14(7):2171-2179.

76. Steffen AC, Orlova A, Wikman M, Nilsson FY, Stahl S, Adams GP, Tolmachev V, Carlsson J 2006. Affibody-mediated tumour targeting of HER-2 expressing xenografts in mice. European journal of nuclear medicine and molecular imaging 33(6):631-638.

77. Baish JW, Netti PA, Jain RK 1997. Transmural coupling of fluid flow in microcirculatory network and interstitium in tumors. Microvascular Research 53(2):128-141.

78. Trotter MJ, Olive PL, Chaplin DJ 1990. Effect of Vascular Marker Hoechst-33342 on Tumor Perfusion and Cardiovascular Function in the Mouse. 62(6):903-908.

79. Grandjean TR, Chappell MJ, Yates JT, Jones K, Wood G, Coleman T 2011. Compartmental modelling of the pharmacokinetics of a breast cancer resistance protein. Computer methods and programs in biomedicine 104(2):81-92.

80. Lalande ME, Ling V, Miller RG 1981. Hoechst 33342 dye uptake as a probe of membrane permeability changes in mammalian cells. Proc Natl Acad Sci U S A 78(1):363-367.

81. Thurber GM, Zajic SC, Wittrup KD 2007. Theoretic criteria for antibody penetration into solid tumors and micrometastases. Journal of nuclear medicine : official publication, Society of Nuclear Medicine 48(6):995-999.

82. Huang S, Endo RI, Nemerow GR 1995. Upregulation of integrins alpha v beta 3 and alpha v beta 5 on human monocytes and T lymphocytes facilitates adenovirus-mediated gene delivery. Journal of virology 69(4):2257-2263.

83. Perrault SD, Walkey C, Jennings T, Fischer HC, Chan WCW 2009. Mediating Tumor Targeting Efficiency of Nanoparticles Through Design. Nano Letters 9(5):1909-1915.

84. Yang Z, Leon J, Martin M, Harder JW, Zhang R, Liang D, Lu W, Tian M, Gelovani JG, Qiao A, Li C 2009. Pharmacokinetics and biodistribution of near-infrared fluorescence polymeric nanoparticles. Nanotechnology 20(16):11.

85. Choi HS, Ipe BI, Misra P, Lee JH, Bawendi MG, Frangioni JV 2009. Tissue- and Organ-Selective Biodistribution of NIR Fluorescent Quantum Dots. Nano Letters.

86. Nahrendorf M, Waterman P, Thurber G, Groves K, Rajopadhye M, Panizzi P, Marinelli B, Aikawa E, Pittet MJ, Swirski FK, Weissleder R 2009. Hybrid In Vivo FMT-CT Imaging of Protease Activity in Atherosclerosis With Customized Nanosensors. Arterioscler Thromb Vasc Biol 29(10):1444-U1489.

87. Blumenthal RD, Fand I, Sharkey RM, Boerman OC, Kashi R, Goldenberg DM 1991. The Effect of Antibody Protein Dose on the Uniformity of Tumor Distribution of Radioantibodies - an Autoradiographic Study. Cancer Immunology Immunotherapy 33(6):351-358.

88. Thurber G, Wittrup KD Submitted. A mechanistic compartmental model for antibody uptake in tumors. Annals of Biomedical Engineering.

89. Jain RK 2005. Normalization of tumor vasculature: An emerging concept in antiangiogenic therapy. Science 307(5706):58-62.

90. Devaraj NK, Thurber GM, Keliher EJ, Marinelli B, Weissleder R 2012. Reactive polymer enables efficient in vivo bioorthogonal chemistry. Proceedings of the National Academy of Sciences of the United States of America 109(13):4762-4767.

91. Keliher EJ, Reiner T, Thurber GM, Upadhyay R, Weissleder R 2012. Efficient 18F-Labeling of Synthetic Exendin-4 Analogues for Imaging Beta Cells. ChemistryOpen:n/a-n/a.

92. Crank J. 1975. The Mathematics of Diffusion. 2 ed., Oxford: Clarendon Press. p 414.

93. Breusegem SY, Loontiens FG, Regenfuss P, Clegg RM 2001. Kinetics of binding of Hoechst dyes to DNA studied by stopped-flow fluorescence techniques. Methods in enzymology 340:212-233.

94. Ojha H, Murari BM, Anand S, Hassan MI, Ahmad F, Chaudhury NK 2009. Interaction of DNA minor groove binder Hoechst 33258 with bovine serum albumin. Chemical & pharmaceutical bulletin 57(5):481-486.

95. Loontiens FG, Regenfuss P, Zechel A, Dumortier L, Clegg RM 1990. Binding characteristics of Hoechst 33258 with calf thymus DNA, poly[d(A-T)] and d(CCGGAATTCCGG): multiple stoichiometries and determination of tight binding with a wide spectrum of site affinities. Biochemistry 29(38):9029-9039.

96. Ferl GZ, Dumont RA, Hildebrandt IJ, Armijo A, Haubner R, Reischl G, Su H, Weber WA, Huang SC 2009. Derivation of a compartmental model for quantifying 64Cu-DOTA-RGD kinetics in tumor-bearing mice. Journal of nuclear medicine : official publication, Society of Nuclear Medicine 50(2):250-258.

97. Kossodo S, Pickarski M, Lin SA, Gleason A, Gaspar R, Buono C, Ho G, Blusztajn A, Cuneo G, Zhang J, Jensen J, Hargreaves R, Coleman P, Hartman G, Rajopadhye M, Duong le T, Sur C, Yared W, Peterson J, Bednar B 2010. Dual in vivo quantification of integrin-targeted and protease-activated agents in cancer using fluorescence molecular tomography (FMT). Molecular imaging and biology : MIB : the official publication of the Academy of Molecular Imaging 12(5):488-499.

98. Smith KA, Hill SA, Begg AC, Denekamp J 1988. Validation of the fluorescent dye Hoechst 33342 as a vascular space marker in tumours. British journal of cancer 57(3):247-253.

99. Bolte S, Cordelieres FP 2006. A guided tour into subcellular colocalization analysis in light microscopy. Journal of Micrsocopy 224:213-232.

100. Weissleder R 2006. Molecular imaging in cancer. Science 312(5777):1168-1171.

101. Minamimoto R, Senda M, Jinnouchi S, Terauchi T, Yoshida T, Murano T, Fukuda H, Iinuma T, Uno K, Nishizawa S, Tsukamoto E, Iwata H, Inoue T, Oguchi K, Nakashima R, Inoue T 2013. The current status of an FDG-PET cancer screening program in Japan, based on a 4-year (2006-2009) nationwide survey. Annals of nuclear medicine 27(1):46-57.

102. Lee H, Shin TH, Cheon J, Weissleder R 2015. Recent Developments in Magnetic Diagnostic Systems. Chem Rev.

103. Kumar AA, Hennek JW, Smith BS, Kumar S, Beattie P, Jain S, Rolland JP, Stossel TP, Chunda-Liyoka C, Whitesides GM 2015. From the bench to the field in low-cost diagnostics: two case studies. Angewandte Chemie 54(20):5836-5853.

104. Hori SS, Gambhir SS 2011. Mathematical model identifies blood biomarker-based early cancer detection strategies and limitations. Science translational medicine 3(109):109ra116.

105. Smith RA, Brooks D, Cokkinides V, Saslow D, Brawley OW 2013. Cancer screening in the United States, 2013: a review of current American Cancer Society guidelines, current issues in cancer screening, and new guidance on cervical cancer screening and lung cancer screening. CA: a cancer journal for clinicians 63(2):88-105.

106. Lutz AM, Willmann JK, Cochran FV, Ray P, Gambhir SS 2008. Cancer screening: a mathematical model relating secreted blood biomarker levels to tumor sizes. PLoS medicine 5(8):e170.

107. Frangioni JV 2008. New technologies for human cancer imaging. Journal of Clinical Oncology 26(24):4012-4021.

108. Chari ST 2007. Detecting early pancreatic cancer: Problems and prospects. Seminars in oncology 34(4):284-294.

109. Minamimoto R, Senda M, Jinnouchi S, Terauchi T, Yoshida T, Inoue T 2015. Detection of breast cancer in an FDG-PET cancer screening program: results of a nationwide Japanese survey. Clinical breast cancer 15(2):e139-146.

110. Klibanov AL 2005. Ligand-Carrying Gas-Filled Microbubbles: Ultrasound Contrast Agents for Targeted Molecular Imaging. Bioconjugate Chemistry 16(1):9-17.

111. Ferrara K, Pollard R, Borden M 2007. Ultrasound microbubble contrast agents: fundamentals and application to gene and drug delivery. Annu Rev Biomed Eng 9:415-447.

112. Viola KL, Sbarboro J, Sureka R, De M, Bicca MA, Wang J, Vasavada S, Satpathy S, Wu S, Joshi H, Velasco PT, MacRenaris K, Waters EA, Lu C, Phan J, Lacor P, Prasad P, Dravid VP, Klein WL 2015. Towards non-invasive diagnostic imaging of early-stage Alzheimer's disease. Nat Nanotechnol 10(1):91-98.

113. Urano Y, Sakabe M, Kosaka N, Ogawa M, Mitsunaga M, Asanuma D, Kamiya M, Young MR, Nagano T, Choyke PL, Kobayashi H 2011. Rapid Cancer Detection by Topically Spraying a gamma-Glutamyltranspeptidase-Activated Fluorescent Probe. Science translational medicine 3(110).

114. Nitin N, Rosbach KJ, El-Naggar A, Williams M, Gillenwater A, Richards-Kortum RR 2009. Optical Molecular Imaging of Epidermal Growth Factor Receptor Expression to Improve Detection of Oral Neoplasia. Neoplasia 11(6):542-551.

115. Hsiung PL, Hardy J, Friedland S, Soetikno R, Du CB, Wu AP, Sahbaie P, Crawford JM, Lowe AW, Contag CH, Wang TD 2008. Detection of colonic dysplasia in vivo using a targeted heptapeptide and confocal microendoscopy. Nature medicine 14(4):454-458.

116. Morris EA 2014. Rethinking breast cancer screening: ultra FAST breast magnetic resonance imaging. Journal of clinical oncology : official journal of the American Society of Clinical Oncology 32(22):2281-2283.

117. Bahmani B, Bacon D, Anvari B 2013. Erythrocyte-derived photo-theranostic agents: hybrid nano-vesicles containing indocyanine green for near infrared imaging and therapeutic applications. Scientific reports 3:2180.

118. Klaassen CD, Plaa GL 1969. Plasma disappearance and biliary excretion of indocyanine green in rats, rabbits, and dogs. Toxicology and Applied Pharmacology 15(2):374-384.

119. Cherrick GR, Stein SW, Leevy CM, Davidson CS 1960. INDOCYANINE GREEN: OBSERVATIONS ON ITS PHYSICAL PROPERTIES, PLASMA DECAY, AND HEPATIC EXTRACTION. Journal of Clinical Investigation 39(4):592-600.

120. Schaafsma BE, Mieog JS, Hutteman M, van der Vorst JR, Kuppen PJ, Lowik CW, Frangioni JV, van de Velde CJ, Vahrmeijer AL 2011. The clinical use of indocyanine green as a near-infrared fluorescent contrast agent for image-guided oncologic surgery. J Surg Oncol 104(3):323-332.

121. Hardesty DA, Thind H, Zabramski JM, Spetzler RF, Nakaji P 2014. Safety, efficacy, and cost of intraoperative indocyanine green angiography compared to intraoperative catheter angiography in cerebral aneurysm surgery. Journal of clinical neuroscience : official journal of the Neurosurgical Society of Australasia 21(8):1377-1382.

122. Leblond F, Davis SC, Valdes PA, Pogue BW 2010. Pre-clinical whole-body fluorescence imaging: Review of instruments, methods and applications. J Photochem Photobiol B-Biol 98(1):77-94.

123. Ogawa M, Regino CAS, Choyke PL, Kobayashi H 2009. In vivo target-specific activatable near-infrared optical labeling of humanized monoclonal antibodies. Molecular cancer therapeutics 8(1):232-239.

124. Wang LV, Hu S 2012. Photoacoustic tomography: in vivo imaging from organelles to organs. Science 335(6075):1458-1462.

125. Blum G, von Degenfeld G, Merchant MJ, Blau HM, Bogyo M 2007. Noninvasive optical imaging of cysteine protease activity using fluorescently quenched activity-based probes. Nat Chem Biol 3(10):668-677.

126. Palmer GM, Fontanella AN, Shan S, Hanna G, Zhang G, Fraser CL, Dewhirst MW 2011. In vivo optical molecular imaging and analysis in mice using dorsal window chamber models applied to hypoxia, vasculature and fluorescent reporters. Nature protocols 6(9):1355-1366.

127. Urano Y, Asanuma D, Hama Y, Koyama Y, Barrett T, Kamiya M, Nagano T, Watanabe T, Hasegawa A, Choyke PL, Kobayashi H 2009. Selective molecular imaging of viable cancer cells with pH-activatable fluorescence probes. Nature medicine 15(1):104-109.

128. Tromberg BJ, Pogue BW, Paulsen KD, Yodh AG, Boas DA, Cerussi AE 2008. Assessing the future of diffuse optical imaging technologies for breast cancer management. Medical physics 35(6):2443-2451.

129. Jung WG, Zhang J, Chung JR, Wilder-Smith P, Brenner M, Nelson JS, Chen ZP 2005. Advances in oral cancer detection using optical coherence tomography. IEEE J Sel Top Quantum Electron 11(4):811-817.

130. Zeff BW, White BR, Dehghani H, Schlaggar BL, Culver JP 2007. Retinotopic mapping of adult human visual cortex with high-density diffuse optical tomography. Proc Natl Acad Sci U S A 104(29):12169-12174.

131. Luo S, Zhang E, Su Y, Cheng T, Shi C 2011. A review of NIR dyes in cancer targeting and imaging. Biomaterials 32(29):7127-7138.

132. Gerega A, Milej D, Weigl W, Botwicz M, Zolek N, Kacprzak M, Wierzejski W, Toczylowska B, Mayzner-Zawadzka E, Maniewski R, Liebert A 2012. Multiwavelength time-resolved detection of fluorescence during the inflow of indocyanine green into the adult's brain. Journal of biomedical optics 17(8):087001.

133. Weigl W, Milej D, Gerega A, Toczylowska B, Kacprzak M, Sawosz P, Botvvicz M, Maniewski R, Mayzner-Zawadzka E, Liebert A 2014. Assessment of cerebral perfusion in post-traumatic brain injury patients with the use of ICG-bolus tracking method. Neuroimage 85:555-565.

134. Mohajerani P, Meier R, Noel PB, Rummeny EJ, Ntziachristos V 2013. Spatiotemporal analysis for indocyanine green-aided imaging of rheumatoid arthritis in hand joints. J Biomed Opt 18(9):097004.

135. Werner SG, Langer HE, Schott P, Bahner M, Schwenke C, Lind-Albrecht G, Spiecker F, Kurtz B, Burmester GR, Backhaus M 2013. Indocyanine green-enhanced fluorescence optical imaging in patients with early and very early arthritis: a comparative study with magnetic resonance imaging. Arthritis and rheumatism 65(12):3036-3044.

136. Massoud TF, Gambhir SS 2007. Integrating noninvasive molecular imaging into molecular medicine: an evolving paradigm. Trends Mol Med 13(5):183-191.

137. Desmettre T, Devoisselle JM, Mordon S 2000. Fluorescence Properties and Metabolic Features of Indocyanine Green (ICG) as Related to Angiography. Survey of Ophthalmology 45(1):15-27.

138. Kaoru Sakatani, Masaki Kashiwasake-Jibu, Yoshinori Taka, Shijie Wang, Huancong Zuo, Katsuyuki Yamamoto, Koichi Shimizu 1997. Noninvasive optical imaging of the subarachnoid space and cerebrospinal fluid pathways based on near-infrared fluorescence. Journal of Neurosurgery 87(5):738-745.

139. van Dam GM, Themelis G, Crane LM, Harlaar NJ, Pleijhuis RG, Kelder W, Sarantopoulos A, de Jong JS, Arts HJ, van der Zee AG, Bart J, Low PS, Ntziachristos V 2011. Intraoperative tumor-specific fluorescence imaging in ovarian cancer by folate receptor-alpha targeting: first in-human results. Nature medicine 17(10):1315-1319.

140. Nguyen QT, Olson ES, Aguilera TA, Jiang T, Scadeng M, Ellies LG, Tsien RY 2010. Surgery with molecular fluorescence imaging using activatable cell-penetrating peptides decreases residual cancer and improves survival. Proceedings of the National Academy of Sciences of the United States of America 107(9):4317-4322.

141. Vahrmeijer AL, Hutteman M, van der Vorst JR, van de Velde CJ, Frangioni JV 2013. Image-guided cancer surgery using near-infrared fluorescence. Nature reviews Clinical oncology 10(9):507-518.

142. Gibbs-Strauss SL, O'Hara JA, Srinivasan S, Hoopes PJ, Hasan T, Pogue BW 2009. Diagnostic detection of diffuse glioma tumors in vivo with molecular fluorescent probe-based transmission spectroscopy. Medical physics 36(3):974-983.

143. Gioux S, Choi HS, Frangioni JV 2010. Image-guided surgery using invisible near-infrared light: fundamentals of clinical translation. Mol Imaging 9(5):237-255.

144. Hope-Ross M, Yannuzzi LA, Gragoudas ES, Guyer DR, Slakter JS, Sorenson JA, Krupsky S, Orlock DA, Puliafito CA 1994. Adverse reactions due to indocyanine green. Ophthalmology 101(3):529-533.

145. Bottinor W, Polkampally P, Jovin I 2013. Adverse reactions to iodinated contrast media. The International journal of angiology : official publication of the International College of Angiology, Inc 22(3):149-154.

146. FDA. 2017. MQSA National Statistics. ed.: FDA.

147. McCamish M, Woollett G 2011. Worldwide experience with biosimilar development. mAbs 3(2):209-217.

148. Jackisch C, Muller V, Maintz C, Hell S, Ataseven B 2014. Subcutaneous Administration of Monoclonal Antibodies in Oncology. Geburtshilfe und Frauenheilkunde 74(4):343-349.

149. Utz KS, Hoog J, Wentrup A, Berg S, Lammer A, Jainsch B, Waschbisch A, Lee DH, Linker RA, Schenk T 2014. Patient preferences for disease-modifying drugs in multiple sclerosis therapy: a choice-based conjoint analysis. Therapeutic advances in neurological disorders 7(6):263-275.

150. van de Ven S, Wiethoff A, Nielsen T, Brendel B, van der Voort M, Nachabe R, Van der Mark M, Van Beek M, Bakker L, Fels L, Elias S, Luijten P, Mali W 2010. A novel fluorescent imaging agent for diffuse optical tomography of the breast: first clinical experience in patients. Molecular imaging and biology : MIB : the official publication of the Academy of Molecular Imaging 12(3):343-348.

151. Poellinger A, Burock S, Grosenick D, Hagen A, Ludemann L, Diekmann F, Engelken F, Macdonald R, Rinneberg H, Schlag PM 2011. Breast cancer: early- and late-fluorescence near-infrared imaging with indocyanine green--a preliminary study. Radiology 258(2):409-416.

152. Bhattacharya S 2010. The facts about penicillin allergy: a review. Journal of advanced pharmaceutical technology & research 1(1):11-17.

153. Macdougall IC 1999. Strategies for iron supplementation: oral versus intravenous. Kidney international Supplement 69:S61-66.

154. Anderson JA, Adkinson NF, Jr. 1987. Allergic reactions to drugs and biologic agents. Jama 258(20):2891-2899.

155. Breen N, Gentleman JF, Schiller JS 2011. Update on mammography trends: comparisons of rates in 2000, 2005, and 2008. Cancer 117(10):2209-2218.

156. Kemp SF, Lockey RF, Simons FE, World Allergy Organization ad hoc Committee on Epinephrine in A 2008. Epinephrine: the drug of choice for anaphylaxis. A statement of the World Allergy Organization. Allergy 63(8):1061-1070.

157. Lipinski CA, Lombardo F, Dominy BW, Feeney PJ 2001. Experimental and computational approaches to estimate solubility and permeability in drug discovery and development settings. Adv Drug Deliv Rev 46(1-3):3-26.

158. Porras AG, Holland SD, Gertz BJ 1999. Pharmacokinetics of alendronate. Clinical pharmacokinetics 36(5):315-328.

159. Coleman PJ, Brashear KM, Hunt CA, Hoffman WF, Hutchinson JH, Breslin MJ, McVean CA, Askew BC, Hartman GD, Rodan SB, Rodan GA, Leu CT, Prueksaritanont T, Fernandez-Metzler C, Ma B, Libby LA, Merkle KM, Stump GL, Wallace AA, Lynch JJ, Lynch R, Duggan ME 2002. Non-peptide alpha(v)beta(3) antagonists. Part 3: identification of potent RGD mimetics incorporating novel beta-amino acids as aspartic acid replacements. Bioorganic & medicinal chemistry letters 12(1):31-34.

160. Han X, Nabors LB 2010. Integrins - a Relevant Target in Glioblastoma. European Journal of Clinical and Medical Oncology 2(1):59-64.

161. Millard M, Odde S, Neamati N 2011. Integrin targeted therapeutics. Theranostics 1:154-188.

162. Wilder RL 2002. Integrin alpha V beta 3 as a target for treatment of rheumatoid arthritis and related rheumatic diseases. Annals of the rheumatic diseases 61 Suppl 2:ii96-99.

163. Zhang L, Bhatnagar S, Deschenes E, Thurber GM 2016. Mechanistic and quantitative insight into cell surface targeted molecular imaging agent design. Sci Rep 6.

164. Bhatnagar S, Deschenes E, Liao J, Cilliers C, Thurber GM 2014. Multichannel Imaging to Quantify Four Classes of Pharmacokinetic Distribution in Tumors. Journal of pharmaceutical sciences 103(10):3276-3286.

165. Zhang L, Bhatnagar S, Deschenes E, Thurber GM 2016. Mechanistic and quantitative insight into cell surface targeted molecular imaging agent design. Sci Rep 6:25424.

166. Czogalla A 2009. Oral cyclosporine A - the current picture of its liposomal and other delivery systems. Cellular & Molecular Biology Letters 14(1):139-152.

167. Hebert MF, Roberts JP, Prueksaritanont T, Benet LZ 1992. Bioavailability of cyclosporine with concomitant rifampin administration is markedly less than predicted by hepatic enzyme induction. Clinical Pharmacology & Therapeutics 52(5):453-457.

168. Kimura RH, Cheng Z, Gambhir SS, Cochran JR 2009. Engineered Knottin Peptides: A New Class of Agents for Imaging Integrin Expression in Living Subjects. Cancer Research 69(6):2435-2442.

169. Zhou Y, Chakraborty S, Liu S 2011. Radiolabeled Cyclic RGD Peptides as Radiotracers for Imaging Tumors and Thrombosis by SPECT. Theranostics 1:58-82.

170. Moore SJ, Gephart MGH, Bergen JM, Su YRS, Rayburn H, Scott MP, Cochran JR 2013. Engineered knottin peptide enables noninvasive optical imaging of intracranial medulloblastoma.

Proceedings of the National Academy of Sciences of the United States of America 110(36):14598-14603.

171. Li ZB, Cai W, Cao Q, Chen K, Wu Z, He L, Chen X 2007. (64)Cu-labeled tetrameric and octameric RGD peptides for small-animal PET of tumor alpha(v)beta(3) integrin expression. Journal of nuclear medicine : official publication, Society of Nuclear Medicine 48(7):1162-1171.

172. Harris TD, Cheesman E, Harris AR, Sachleben R, Edwards DS, Liu S, Bartis J, Ellars C, Onthank D, Yalamanchili P, Heminway S, Silva P, Robinson S, Lazewatsky J, Rajopadhye M, Barrett J 2007. Radiolabeled divalent peptidomimetic vitronectin receptor antagonists as potential tumor radiotherapeutic and imaging agents. Bioconjug Chem 18(4):1266-1279.

173. Uchida M, Willits DA, Muller K, Willis AF, Jackiw L, Jutila M, Young MJ, Porter AE, Douglas T 2009. Intracellular Distribution of Macrophage Targeting Ferritin–Iron Oxide Nanocomposite. Advanced Materials 21(4):458-462.

174. Kageshita T, Hamby CV, Hirai S, Kimura T, Ono T, Ferrone S 2000. αvβ3 expression on blood vessels and melanoma cells in primary lesions; differential association with tumor progression and clinical prognosis. Cancer Immunol Immunother 49(6):314-318.

175. Antonov AS, Kolodgie FD, Munn DH, Gerrity RG 2004. Regulation of Macrophage Foam Cell Formation by αVβ3 Integrin: Potential Role in Human Atherosclerosis. The American Journal of Pathology 165(1):247-258.

176. Nabors LB, Mikkelsen T, Rosenfeld SS, Hochberg F, Akella NS, Fisher JD, Cloud GA, Zhang Y, Carson K, Wittemer SM, Colevas AD, Grossman SA 2007. Phase I and correlative biology study of cilengitide in patients with recurrent malignant glioma. Journal of clinical oncology : official journal of the American Society of Clinical Oncology 25(13):1651-1657.

177. Cox D, Brennan M, Moran N 2010. Integrins as therapeutic targets: lessons and opportunities. Nature reviews Drug discovery 9(10):804-820.

178. Coleman PJ, Brashear KM, Askew BC, Hutchinson JH, McVean CA, Duong LT, Feuston BP, Fernandez-Metzler C, Gentile MA, Hartman GD, Kimmel DB, Leu C-T, Lipfert L, Merkle K, Pennypacker B, Prueksaritanont T, Rodan GA, Wesolowski GA, Rodan SB, Duggan ME 2004. Nonpeptide αvβ3 Antagonists. Part 11: Discovery and Preclinical Evaluation of Potent αvβ3 Antagonists for the Prevention and Treatment of Osteoporosis. J Med Chem 47(20):4829-4837.

179. Xiong JP, Stehle T, Zhang R, Joachimiak A, Frech M, Goodman SL, Arnaout MA 2002. Crystal structure of the extracellular segment of integrin alpha Vbeta3 in complex with an Arg-Gly-Asp ligand. Science 296(5565):151-155.

180. Harlaar NJ, Kelder W, Sarantopoulos A, Bart J, Themelis G, van Dam GM, Ntziachristos V 2013. Real-time near infrared fluorescence (NIRF) intra-operative imaging in ovarian cancer using an αvβ3-integrin targeted agent. Gynecologic Oncology 128(3):590-595.

181. Hutteman M, Mieog JSD, van der Vorst JR, Dijkstra J, Kuppen PJK, van der Laan AMA, Tanke HJ, Kaijzel EL, Que I, van de Velde CJH, Löwik CWGM, Vahrmeijer AL 2011. Intraoperative near-infrared fluorescence imaging of colorectal metastases targeting integrin αvβ3 expression in a syngeneic rat model. European Journal of Surgical Oncology (EJSO) 37(3):252-257.

182. Xiao Y, Li P, Cheng Y, Zhang X, Sheng J, Wang D, Li J, Zhang Q, Zhong C, Cao R, Wang F 2014. Enhancing the intestinal absorption of low molecular weight chondroitin sulfate by conjugation with alpha-linolenic acid and the transport mechanism of the conjugates. International journal of pharmaceutics 465(1-2):143-158.

183. Hiebert LM, Wice SM, Ping T 2005. Increased plasma anti-Xa activity and recovery of heparin from urine suggest absorption of orally administered unfractionated heparin in human subjects. The Journal of laboratory and clinical medicine 145(3):151-155.

184. El-Sayed M, Ginski M, Rhodes C, Ghandehari H 2002. Transepithelial transport of poly(amidoamine) dendrimers across Caco-2 cell monolayers. Journal of controlled release : official journal of the Controlled Release Society 81(3):355-365.

185. Hubbard D, Enda M, Bond T, Moghaddam SP, Conarton J, Scaife C, Volckmann E, Ghandehari H 2015. Transepithelial Transport of PAMAM Dendrimers Across Isolated Human Intestinal Tissue. Molecular pharmaceutics 12(11):4099-4107.

186. Thiagarajan G, Sadekar S, Greish K, Ray A, Ghandehari H 2013. Evidence of oral translocation of anionic G6.5 dendrimers in mice. Molecular pharmaceutics 10(3):988-998.

187. Mousa SA, Zhang F, Aljada A, Chaturvedi S, Takieddin M, Zhang H, Chi L, Castelli MC, Friedman K, Goldberg MM, Linhardt RJ 2007. Pharmacokinetics and pharmacodynamics of oral heparin solid dosage form in healthy human subjects. Journal of clinical pharmacology 47(12):1508-1520.

188. Baughman RA, Kapoor SC, Agarwal RK, Kisicki J, Catella-Lawson F, FitzGerald GA 1998. Oral delivery of anticoagulant doses of heparin. A randomized, double-blind, controlled study in humans. Circulation 98(16):1610-1615.

189. Castelli MC, Wong DF, Friedman K, Riley MG 2011. Pharmacokinetics of oral cyanocobalamin formulated with sodium N-[8-(2-hydroxybenzoyl)amino]caprylate (SNAC): an open-label, randomized, single-dose, parallel-group study in healthy male subjects. Clinical therapeutics 33(7):934-945.

190. Aungst BJ 2012. Absorption enhancers: applications and advances. The AAPS journal 14(1):10-18.

191. Maher S, Leonard TW, Jacobsen J, Brayden DJ 2009. Safety and efficacy of sodium caprate in promoting oral drug absorption: from in vitro to the clinic. Adv Drug Deliv Rev 61(15):1427-1449.

192. Walsh EG, Adamczyk BE, Chalasani KB, Maher S, O'Toole EB, Fox JS, Leonard TW, Brayden DJ 2011. Oral delivery of macromolecules: rationale underpinning Gastrointestinal Permeation Enhancement Technology (GIPET). Therapeutic delivery 2(12):1595-1610.

193. Vetter A, Perera G, Leithner K, Klima G, Bernkop-Schnurch A 2010. Development and in vivo bioavailability study of an oral fondaparinux delivery system. European journal of pharmaceutical sciences : official journal of the European Federation for Pharmaceutical Sciences 41(3-4):489-497.

194. Ralay-Ranaivo B, Desmaele D, Bianchini EP, Lepeltier E, Bourgaux C, Borgel D, Pouget T, Tranchant JF, Couvreur P, Gref R 2014. Novel self assembling nanoparticles for the oral administration of fondaparinux: synthesis, characterization and in vivo evaluation. Journal of controlled release : official journal of the Controlled Release Society 194:323-331.

195. Brady CE, 3rd, DiPalma JA, Morawski SG, Santa Ana CA, Fordtran JS 1986. Urinary excretion of polyethylene glycol 3350 and sulfate after gut lavage with a polyethylene glycol electrolyte lavage solution. Gastroenterology 90(6):1914-1918.

196. Ryan CM, Yarmush ML, Tompkins RG 1992. Separation and quantitation of polyethylene glycols 400 and 3350 from human urine by high-performance liquid chromatography. Journal of pharmaceutical sciences 81(4):350-352.

197. Pelham RW, Nix LC, Chavira RE, Cleveland MV, Stetson P 2008. Clinical trial: single- and multiple-dose pharmacokinetics of polyethylene glycol (PEG-3350) in healthy young and elderly subjects. Alimentary pharmacology & therapeutics 28(2):256-265.

198. Donovan MD, Flynn GL, Amidon GL 1990. ABSORPTION OF POLYETHYLENE GLYCOL-600 THROUGH POLYETHYLENE GLYCOL-2000 - THE MOLECULAR-WEIGHT DEPENDENCE OF GASTROINTESTINAL AND NASAL ABSORPTION. Pharmaceutical research 7(8):863-868.

199. Shaffer CB, Critchfield FH 1947. The absorption and excretion of the solid polyethylene glycols; (carbowax compounds). Journal of the American Pharmaceutical Association American Pharmaceutical Association 36(5):152-157.

200. Shaffer CB, Critchfield FH, Nair JH, 3rd 1950. The absorption and excretion of a liquid polyethylene glycol. Journal of the American Pharmaceutical Association American Pharmaceutical Association 39(6):340-344.

201. Volpi N 2002. Oral bioavailability of chondroitin sulfate (Condrosulf) and its constituents in healthy male volunteers. Osteoarthritis and cartilage 10(10):768-777.

202. Volpi N 2010. About oral absorption and human pharmacokinetics of chondroitin sulfate. Osteoarthritis and cartilage 18(8):1104-1105; author reply 1106-1107.

203. Volpi N 2007. Analytical aspects of pharmaceutical grade chondroitin sulfates. Journal of pharmaceutical sciences 96(12):3168-3180.

204. Qi Y, Zhao G, Liu D, Shriver Z, Sundaram M, Sengupta S, Venkataraman G, Langer R, Sasisekharan R 2004. Delivery of therapeutic levels of heparin and low-molecular-weight heparin through a pulmonary route. Proc Natl Acad Sci U S A 101(26):9867-9872.

205. Ott P 1998. Hepatic Elimination of Indocyanine Green with Special Reference to Distribution Kinetics and the Influence of Plasma Protein Binding. Pharmacology & Toxicology 83:1-48.

206. Hamann FM, Brehm R, Pauli J, Grabolle M, Frank W, Kaiser WA, Fischer D, Resch-Genger U, Hilger I 2011. Controlled modulation of serum protein binding and biodistribution of asymmetric cyanine dyes by variation of the number of sulfonate groups. Mol Imaging 10(4):258-269.

207. van de Waterbeemd H, Testa B. 2009. Drug Bioavailability. 2nd ed., Morlenbach, Germany: Wiley-VCH.

208. Li E, Brown SL, Stupack DG, Puente XS, Cheresh DA, Nemerow GR 2001. Integrin αvβ1 Is an Adenovirus Coreceptor. Journal of virology 75(11):5405-5409.

209. Miller JM, Dahan A, Gupta D, Varghese S, Amidon GL 2010. Enabling the intestinal absorption of highly polar antiviral agents: ion-pair facilitated membrane permeation of zanamivir heptyl ester and guanidino oseltamivir. Molecular pharmaceutics 7(4):1223-1234.

210. Corlu A, Choe R, Durduran T, Rosen MA, Schweiger M, Arridge SR, Schnall MD, Yodh AG 2007. Three-dimensional in vivo fluorescence diffuse optical tomography of breast cancer in humans. Opt Express 15(11):6696-6716.

211. Lannin DR, Wang S 2017. Are Small Breast Cancers Good because They Are Small or Small because They Are Good? The New England journal of medicine 376(23):2286-2291.

212. Welch HG, Prorok PC, O'Malley AJ, Kramer BS 2016. Breast-Cancer Tumor Size, Overdiagnosis, and Mammography Screening Effectiveness. New England Journal of Medicine 375(15):1438-1447.

213. Gill JK, Maskarinec G, Pagano I, Kolonel LN 2006. The association of mammographic density with ductal carcinoma in situ of the breast: the Multiethnic Cohort. Breast cancer research : BCR 8(3):R30.

214. White E, Velentgas P, Mandelson MT, Lehman CD, Elmore JG, Porter P, Yasui Y, Taplin SH 1998. Variation in Mammographic Breast Density by Time in Menstrual Cycle Among Women Aged 40–49 Years. JNCI: Journal of the National Cancer Institute 90(12):906-910.

215. Ong MS, Mandl KD 2015. National expenditure for false-positive mammograms and breast cancer overdiagnoses estimated at $4 billion a year. Health affairs 34(4):576-583.

216. Danino T, Prindle A, Kwong GA, Skalak M, Li H, Allen K, Hasty J, Bhatia SN 2015. Programmable probiotics for detection of cancer in urine. Science translational medicine 7(289):289ra284.

217. Hawrysz DJ, Sevick-Muraca EM 2000. Developments toward diagnostic breast cancer imaging using near-infrared optical measurements and fluorescent contrast agents. Neoplasia 2(5):388-417.

218. Ntziachristos V, Yodh AG, Schnall M, Chance B 2000. Concurrent MRI and diffuse optical tomography of breast after indocyanine green enhancement. Proc Natl Acad Sci U S A 97(6):2767-2772.

219. Li X, Chance B, Yodh AG 1998. Fluorescent heterogeneities in turbid media: limits for detection, characterization, and comparison with absorption. Appl Opt 37(28):6833-6844.

220. Davis SC, Pogue BW, Dehghani H, Paulsen KD 2009. Tissue drug concentration determines whether fluorescence or absorption measurements are more sensitive in diffuse optical tomography of exogenous contrast agents. Appl Opt 48(10):D262-272.

221. Ku G, Wang LV 2005. Deeply penetrating photoacoustic tomography in biological tissues enhanced with an optical contrast agent. Opt Lett 30(5):507-509.

222. Chen H, Niu G, Wu H, Chen X 2016. Clinical Application of Radiolabeled RGD Peptides for PET Imaging of Integrin alphavbeta3. Theranostics 6(1):78-92.

223. Knopfelmacher A, Fox J, Lo Y, Shapiro N, Fineberg S 2015. Correlation of histopathologic features of ductal carcinoma in situ of the breast with the oncotype DX DCIS score. Modern pathology : an official journal of the United States and Canadian Academy of Pathology, Inc 28(9):1167-1173.

224. Dayton PA, Pearson D, Clark J, Simon S, Schumann PA, Zutshi R, Matsunaga TO, Ferrara KW 2004. Ultrasonic analysis of peptide- and antibody-targeted microbubble contrast agents for molecular imaging of alphavbeta3-expressing cells. Mol Imaging 3(2):125-134.

225. Waldeck J, Hager F, Holtke C, Lanckohr C, von Wallbrunn A, Torsello G, Heindel W, Theilmeier G, Schafers M, Bremer C 2008. Fluorescence reflectance imaging of macrophage-rich atherosclerotic plaques using an alphavbeta3 integrin-targeted fluorochrome. Journal of nuclear medicine : official publication, Society of Nuclear Medicine 49(11):1845-1851.

226. Taherian A, Li X, Liu Y, Haas TA 2011. Differences in integrin expression and signaling within human breast cancer cells. BMC Cancer 11:293.

227. Takayama S, Ishii S, Ikeda T, Masamura S, Doi M, Kitajima M 2005. The relationship between bone metastasis from human breast cancer and integrin alpha(v)beta3 expression. Anticancer research 25(1A):79-83.

228. Guidi AJ, Fischer L, Harris JR, Schnitt SJ 1994. Microvessel density and distribution in ductal carcinoma in situ of the breast. J Natl Cancer Inst 86(8):614-619.

229. Narod SA, Iqbal J, Giannakeas V, Sopik V, Sun P 2015. Breast Cancer Mortality After a Diagnosis of Ductal Carcinoma In Situ. JAMA oncology 1(7):888-896.

230. Esserman L, Yau C 2015. Rethinking the Standard for Ductal Carcinoma In Situ Treatment. JAMA oncology 1(7):881-883.

231. van Luijt PA, Heijnsdijk EA, Fracheboud J, Overbeek LI, Broeders MJ, Wesseling J, den Heeten GJ, de Koning HJ 2016. The distribution of ductal carcinoma in situ (DCIS) grade in 4232 women and its impact on overdiagnosis in breast cancer screening. Breast cancer research : BCR 18(1):47.

232. Marquez JP, Stanton SE, Disis ML 2015. The antigenic repertoire of premalignant and high-risk lesions. Cancer Prev Res (Phila) 8(4):266-270.

233. Boyd NF, Martin LJ, Yaffe MJ, Minkin S 2011. Mammographic density and breast cancer risk: current understanding and future prospects. Breast cancer research : BCR 13(6):223.

234. Habel LA, Dignam JJ, Land SR, Salane M, Capra AM, Julian TB 2004. Mammographic density and breast cancer after ductal carcinoma in situ. J Natl Cancer Inst 96(19):1467-1472.

235. Jacques SL 2013. Optical properties of biological tissues: a review. Physics in medicine and biology 58(11):R37-61.

236. Chen G, Ouyang Z, Wang F, Wu H, Jia B, Chordia MD 2017. Evaluation of Tc-99m-3PRGD2 Integrin Receptor Imaging in the Differential Diagnosis of Breast Lesions and Comparison With Mammography. Cancer investigation 35(2):108-115.

237. Breen N, A. Cronin K, Meissner HI, Taplin SH, Tangka FK, Tiro JA, McNeel TS 2007. Reported drop in mammography. Cancer 109(12):2405-2409.

238. Cilliers C, Liao J, Atangcho L, Thurber G 2015. Residualization Rates of Near-Infrared Dyes for the Rational Design of Molecular Imaging Agents. Molecular Imaging and Biology:1-6.

239. Calonge N, Petitti DB, DeWitt TG, Dietrich AJ, Gregory KD, Grossman D, Isham G, LeFevre ML, Leipzig RM, Marion LN, Melnyk B, Moyer VA, Ockene JK, Sawaya GF, Schwartz JS, Wilt T, Force USPST 2009. Screening for Breast Cancer: US Preventive Services Task Force Recommendation Statement. Annals of internal medicine 151(10):716-W236.

240. Heywang-Köbrunner SH, Hacker A, Sedlacek S 2011. Advantages and Disadvantages of Mammography Screening. Breast Care 6(3):199-207.

241. Bleyer A, Welch HG 2012. Effect of three decades of screening mammography on breast-cancer incidence. N Engl J Med 367(21):1998-2005.

242. Boyd N, Martin L, Chavez S, Gunasekara A, Salleh A, Melnichouk O, Yaffe M, Friedenreich C, Minkin S, Bronskill M 2009. Breast-tissue composition and other risk factors for breast cancer in young women: a cross-sectional study. The Lancet Oncology 10(6):569-580.

243. Ntziachristos V 2010. Going deeper than microscopy: the optical imaging frontier in biology. Nature methods 7(8):603-614.

244. Brooks PC, Strömblad S, Klemke R, Visscher D, Sarkar FH, Cheresh DA 1995. Antiintegrin alpha v beta 3 blocks human breast cancer growth and angiogenesis in human skin. Journal of Clinical Investigation 96(4):1815-1822.

245. Sloan EK, Pouliot N, Stanley KL, Chia J, Moseley JM, Hards DK, Anderson RL 2006. Tumor-specific expression of alphavbeta3 integrin promotes spontaneous metastasis of breast cancer to bone. Breast cancer research : BCR 8(2):R20.

246. Desgrosellier JS, Cheresh DA 2010. Integrins in cancer: biological implications and therapeutic opportunities. Nature reviews Cancer 10(1):9-22.

247. Zhu Q, Tannenbaum S, Hegde P, Kane M, Xu C, Kurtzman SH 2008. Noninvasive monitoring of breast cancer during neoadjuvant chemotherapy using optical tomography with ultrasound localization. Neoplasia 10(10):1028-1040.

248. Reiner T, Thurber G, Gaglia J, Vinegoni C, Liew CW, Upadhyay R, Kohler RH, Li L, Kulkarni RN, Benoist C, Mathis D, Weissleder R 2011. Accurate measurement of pancreatic islet beta-cell mass using a second-generation fluorescent exendin-4 analog. Proceedings of the National Academy of Sciences of the United States of America 108(31):12815-12820.

249. Mohs AM, Mancini MC, Singhal S, Provenzale JM, Leyland-Jones B, Wang MD, Nie SM 2010. Hand-held Spectroscopic Device for In Vivo and Intraoperative Tumor Detection: Contrast Enhancement, Detection Sensitivity, and Tissue Penetration. Anal Chem 82(21):9058-9065.

250. Hagen A, Grosenick D, Macdonald R, Rinneberg H, Burock S, Warnick P, Poellinger A, Schlag PM 2009. Late-fluorescence mammography assesses tumor capillary permeability and differentiates malignant from benign lesions. Opt Express 17(19):17016-17033.

251. Ntziachristos V, Chance B 2001. Probing physiology and molecular function using optical imaging: applications to breast cancer. Breast cancer research : BCR 3(1):41-46.

252. Collettini F, Martin JC, Diekmann F, Fallenberg E, Engelken F, Ponder S, Kroencke TJ, Hamm B, Poellinger A 2012. Diagnostic performance of a Near-Infrared Breast Imaging system as adjunct to mammography versus X-ray mammography alone. Eur Radiol 22(2):350-357.

253. Adams A, Mourik JE, van der Voort M, Pearlman PC, Nielsen T, Mali WP, Elias SG 2012. Estimation of detection limits of a clinical fluorescence optical mammography system for the near-infrared fluorophore IRDye800CW: phantom experiments. Journal of biomedical optics 17(7):076022.

254. Ubrich N, Maincent P. 2005. Recent Advances in Heparin Delivery. In Benita S, editor Microencapsulation, ed.: Informa Healthcare. p 481-520.

255. Arbit E, Goldberg M, Gomez-Orellana I, Majuru S 2006. Oral heparin: status review. Thrombosis journal 4:6.

256. Motlekar NA, Srivenugopal KS, Wachtel MS, Youan BB 2006. Modulation of gastrointestinal permeability of low-molecular-weight heparin by L-arginine: in-vivo and in-vitro evaluation. The Journal of pharmacy and pharmacology 58(5):591-598.

257. Oliveira S, Cohen R, Stigter-van Walsum M, van Dongen G, Elias SG, van Diest PJ, Mali W, en Henegouwen PMvB 2012. A novel method to quantify IRDye800CW fluorescent antibody probes ex vivo in tissue distribution studies. EJNMMI research 2(1):50.

258. Scott DL, Smith C, Kingsley G 2003. Joint damage and disability in rheumatoid arthritis: an updated systematic review. Clinical and experimental rheumatology 21(5 Suppl 31):S20-27.

259. Gibofsky A 2012. Overview of epidemiology, pathophysiology, and diagnosis of rheumatoid arthritis. The American journal of managed care 18(13 Suppl):S295-302.

260. Lipsky PE 2009. Are new agents needed to treat RA? Nat Rev Rheumatol 5(10):521-522.

261. van Steenbergen HW, da Silva JAP, Huizinga TWJ, van der Helm-van Mil AHM 2018. Preventing progression from arthralgia to arthritis: targeting the right patients. Nature reviews Rheumatology 14(1):32-41.

262. Singh JA, Furst DE, Bharat A, Curtis JR, Kavanaugh AF, Kremer JM, Moreland LW, O'Dell J, Winthrop KL, Beukelman T, Bridges SL, Jr., Chatham WW, Paulus HE, Suarez-Almazor M, Bombardier C, Dougados M, Khanna D, King CM, Leong AL, Matteson EL, Schousboe JT, Moynihan E, Kolba KS, Jain A, Volkmann ER, Agrawal H, Bae S, Mudano AS,

Patkar NM, Saag KG 2012. 2012 update of the 2008 American College of Rheumatology recommendations for the use of disease-modifying antirheumatic drugs and biologic agents in the treatment of rheumatoid arthritis. Arthritis care & research 64(5):625-639.

263. Resnick D 1988. Common disorders of synovium-lined joints: pathogenesis, imaging abnormalities, and complications. AJR American journal of roentgenology 151(6):1079-1093.

264. Szkudlarek M, Court-Payen M, Strandberg C, Klarlund M, Klausen T, Ostergaard M 2001. Power Doppler ultrasonography for assessment of synovitis in the metacarpophalangeal joints of patients with rheumatoid arthritis: a comparison with dynamic magnetic resonance imaging. Arthritis and rheumatism 44(9):2018-2023.

265. Szkudlarek M, Klarlund M, Narvestad E, Court-Payen M, Strandberg C, Jensen KE, Thomsen HS, Østergaard M 2006. Ultrasonography of the metacarpophalangeal and proximal interphalangeal joints in rheumatoid arthritis: a comparison with magnetic resonance imaging, conventional radiography and clinical examination. Arthritis Research & Therapy 8(2):R52.

266. Backhaus M, Kamradt T, Sandrock D, Loreck D, Fritz J, Wolf KJ, Raber H, Hamm B, Burmester GR, Bollow M 1999. Arthritis of the finger joints: a comprehensive approach comparing conventional radiography, scintigraphy, ultrasound, and contrast-enhanced magnetic resonance imaging. Arthritis and rheumatism 42(6):1232-1245.

267. Scheel AK, Hermann KG, Ohrndorf S, Werner C, Schirmer C, Detert J, Bollow M, Hamm B, Muller GA, Burmester GR, Backhaus M 2006. Prospective 7 year follow up imaging study comparing radiography, ultrasonography, and magnetic resonance imaging in rheumatoid arthritis finger joints. Annals of the rheumatic diseases 65(5):595-600.

268. Wunder A, Tung CH, Muller-Ladner U, Weissleder R, Mahmood U 2004. In vivo imaging of protease activity in arthritis: a novel approach for monitoring treatment response. Arthritis and rheumatism 50(8):2459-2465.

269. Schafer VS, Hartung W, Hoffstetter P, Berger J, Stroszczynski C, Muller M, Fleck M, Ehrenstein B 2013. Quantitative assessment of synovitis in patients with rheumatoid arthritis using fluorescence optical imaging. Arthritis Research & Therapy 15(5):R124.

270. Benson RC, Kues HA 1978. Fluorescence properties of indocyanine green as related to angiography. Physics in medicine and biology 23(1):159-163.

271. Dziekan T, Weissbach C, Voigt J, Ebert B, Macdonald R, Bahner ML, Mahler M, Schirner M, Berliner M, Berliner B, Osel J, Osel I 2011. Detection of rheumatoid arthritis by evaluation of normalized variances of fluorescence time correlation functions. Journal of biomedical optics 16(7):076015.

272. Kisten Y, Gyori N, Af Klint E, Rezaei H, Levitsky A, Karlsson A, van Vollenhoven R 2015. Detection of clinically manifest and silent synovitis in the hands and wrists by fluorescence optical imaging. RMD open 1(1):e000106.

273. Wang L. WH. 2007. Biomedical Optics: Principles and Imaging. ed., Hoboken, NJ: Wiley.

274. Thurber GM, Figueiredo J-L, Weissleder R 2010. Detection limits of intraoperative near infrared imaging for tumor resection. J Surg Oncol 102(7):758-764.

275. Bhatnagar S, Verma KD, Hu Y, Khera E, Priluck A, Smith D, Thurber GM 2018. Oral Administration and Detection of a Near-Infrared Molecular Imaging Agent in an Orthotopic Mouse Model for Breast Cancer Screening. Molecular pharmaceutics.

276. Theumann NH, Pfirrmann CW, Drape JL, Trudell DJ, Resnick D 2002. MR imaging of the metacarpophalangeal joints of the fingers: part I. Conventional MR imaging and MR arthrographic findings in cadavers. Radiology 222(2):437-445.

277. Nieuwenhuis WP, Krabben A, Stomp W, Huizinga TW, van der Heijde D, Bloem JL, van der Helm-van Mil AH, Reijnierse M 2015. Evaluation of magnetic resonance imaging-detected tenosynovitis in the hand and wrist in early arthritis. Arthritis & rheumatology (Hoboken, NJ) 67(4):869-876.

278. Burgers LE, Allaart CF, Huizinga TWJ, van der Helm-van Mil AHM 2017. Brief Report: Clinical Trials Aiming to Prevent Rheumatoid Arthritis Cannot Detect Prevention Without Adequate Risk Stratification: A Trial of Methotrexate Versus Placebo in Undifferentiated Arthritis as an Example. Arthritis & rheumatology 69(5):926-931.

279. Alander JT, Kaartinen I, Laakso A, Patila T, Spillmann T, Tuchin VV, Venermo M, Valisuo P 2012. A review of indocyanine green fluorescent imaging in surgery. International journal of biomedical imaging 2012:940585.

280. Bender AT, Spyvee M, Satoh T, Gershman B, Teceno T, Burgess L, Kumar V, Wu Y, Yang H, Ding Y, Akare S, Chen Q 2013. Evaluation of a candidate anti-arthritic drug using the mouse collagen antibody induced arthritis model and clinically relevant biomarkers. American journal of translational research 5(1):92-102.

281. Chan MM, Gray BD, Pak KY, Fong D 2015. Non-invasive in vivo imaging of arthritis in a collagen-induced murine model with phosphatidylserine-binding near-infrared (NIR) dye. Arthritis Research & Therapy 17:50.

282. Cho H, Bhatti FU, Yoon TW, Hasty KA, Stuart JM, Yi AK 2016. Non-invasive dual fluorescence in vivo imaging for detection of macrophage infiltration and matrix

metalloproteinase (MMP) activity in inflammatory arthritic joints. Biomedical optics express 7(5):1842-1852.

283. Chen WT, Mahmood U, Weissleder R, Tung CH 2005. Arthritis imaging using a near-infrared fluorescence folate-targeted probe. Arthritis Research & Therapy 7(2):R310-317.

284. Ryu JH, Lee A, Chu JU, Koo H, Ko CY, Kim HS, Yoon SY, Kim BS, Choi K, Kwon IC 2011. Early diagnosis of arthritis in mice with collagen–induced arthritis, using a fluorogenic matrix metalloproteinase 3–specific polymeric probe. Arthritis & Rheumatism 63(12):3824-3832.

285. Garrood T, Morrison M, Shivapatham D, Chaabo K, Ul-Hassan F, Ballinger J, Cook G, Cope A 2015. Whole-Body Synovial Uptake of a 99m-Tc-Labelled RGD Peptide is Highly Correlated with Power Doppler Ultrasound [abstract]. Arthritis Rheumatol 67((suppl 10)):http://acrabstracts.org/abstract/whole-body-synovial-uptake-of-a-99mtc-labelled-rgd-peptide-is-highly-correlated-with-power-doppler-ultrasound/.

286. Zhu Z, Yin Y, Zheng K, Li F, Chen X, Zhang F, Zhang X 2014. Evaluation of synovial angiogenesis in patients with rheumatoid arthritis using (6)(8)Ga-PRGD2 PET/CT: a prospective proof-of-concept cohort study. Annals of the rheumatic diseases 73(6):1269-1272.

287. Vollmer S, Vater A, Licha K, Gemeinhardt I, Gemeinhardt O, Voigt J, Ebert B, Schnorr J, Taupitz M, Macdonald R, Schirner M 2009. Extra domain B fibronectin as a target for near-infrared fluorescence imaging of rheumatoid arthritis affected joints in vivo. Mol Imaging 8(6):330-340.

288. Bennett JS 2005. Structure and function of the platelet integrin α(IIb)β(3). Journal of Clinical Investigation 115(12):3363-3369.

289. Cherry SR. SJ, Phelps ME. 2003. Physics in Nuclear Medicine. Fourth ed.: Elsevier Saunders.

290. Keating J, Judy R, Newton A, Singhal S 2016. Near-infrared operating lamp for intraoperative molecular imaging of a mediastinal tumor. BMC medical imaging 16:15.

291. Rose A. 1974. Vision: Human and Electronic. ed.: Springer.

292. Haacke ME, Brown, Robert L., Thompson, Kichael R., Venkatesan, Ramesan. 2014. Magnetic Resonance Imaging: Physical Principles and Sequence Design. ed.: Wiley.

293. Dickerscheid D, Lavalaye J, Romijn L, Habraken J 2013. Contrast-noise-ratio (CNR) analysis and optimisation of breast-specific gamma imaging (BSGI) acquisition protocols. EJNMMI research 3(1):21.

294. Thurber GM, Figueiredo JL, Weissleder R 2010. Detection Limits of Intraoperative Near Infrared Imaging for Tumor Resection. J Surg Oncol 102(7):758-764.

295. Thompson RD, Wakelin MW, Larbi KY, Dewar A, Asimakopoulos G, Horton MA, Nakada MT, Nourshargh S 2000. Divergent effects of platelet-endothelial cell adhesion molecule-1 and beta 3 integrin blockade on leukocyte transmigration in vivo. Journal of immunology 165(1):426-434.

296. Lu YJ, Leamon CP. 2011. Targeting Activated Macrophages Via a Functional Folate Receptor for Potential Treatment of Autoimmune/Inflammatory Disorders. ed., New York: Springer. p 195-216.

297. Paulos CM, Turk MJ, Breur GJ, Low PS 2004. Folate receptor-mediated targeting of therapeutic and imaging agents to activated macrophages in rheumatoid arthritis. Adv Drug Deliv Rev 56(8):1205-1217.

298. Varghese B, Vlashi E, Xia W, Ayala Lopez W, Paulos CM, Reddy J, Xu LC, Low PS 2014. Folate receptor-beta in activated macrophages: ligand binding and receptor recycling kinetics. Molecular pharmaceutics 11(10):3609-3616.

299. Bhatnagar S, Verma KD, Hu Y, Khera E, Priluck A, Smith DE, Thurber GM 2018. Oral Administration and Detection of a Near-Infrared Molecular Imaging Agent in an Orthotopic Mouse Model for Breast Cancer Screening. Molecular pharmaceutics 15(5):1746-1754.

300. Haskell RC, Svaasand LO, Tsay TT, Feng TC, McAdams MS 1994. Boundary-Conditions for the Diffusion Equation in Radiative-Transfer. J Opt Soc Am A-Opt Image Sci Vis 11(10):2727-2741.

301. Ripoll J, Schulz RB, Ntziachristos V 2003. Free-space propagation of diffuse light: Theory and experiments. Phys Rev Lett 91(10):4.

302. Morgan MP, Cooke MM, McCarthy GM 2005. Microcalcifications Associated with Breast Cancer: An Epiphenomenon or Biologically Significant Feature of Selected Tumors? Journal of Mammary Gland Biology and Neoplasia 10(2):181-187.

303. Gabriella WA, Sonal V, A. GE, J. CP, Clifford CKS, He L, H. BN, J. SS 2014. Prostate-specific membrane antigen expression in tumor-associated vasculature of breast cancers. APMIS 122(6):482-489.

304. MERDAD A, KARIM S, SCHULTEN H-J, DALLOL A, BUHMEIDA A, AL-THUBAITY F, GARI MA, CHAUDHARY AG, ABUZENADAH AM, AL-QAHTANI MH 2014. Expression of Matrix Metalloproteinases (MMPs) in Primary Human Breast Cancer: MMP-9 as a Potential Biomarker for Cancer Invasion and Metastasis. Anticancer research 34(3):1355-1366.

305. Davies M, Pieber TR, Hartoft-Nielsen M, Hansen OH, Jabbour S, Rosenstock J 2017. Effect of oral semaglutide compared with placebo and subcutaneous semaglutide on glycemic control in patients with type 2 diabetes: A randomized clinical trial. Jama 318(15):1460-1470.